Dissertation

submitted to the
Combined Faculties for the Natural Sciences and for Mathematics
of the Ruperto-Carola University of Heidelberg, Germany
for the degree of
Doctor of Natural Sciences

presented by

Paola Caprile
Born in Santiago, Chile

Oral examination: 08 July, 2009

Development of a Dose Calculation Model as a Supplemental Quality Assurance Tool for TomoTherapy

Referees: Prof. Dr. Günther H. Hartmann
Prof. Dr. Wolfgang Schlegel

to Timo...

Zusammenfassung

Entwicklung eines Modells zur Dosisberechnung als zusätzliches Werkzeug für die Qualitätssicherung in der TomoTherapie

Die helikale TomoTherapie® ist eine moderne Technik in der Strahlentherapie mit Photonen. Das System beruht auf der Überlagerung einer Vielzahl kleiner Felder um die verordnete Dosisverteilung mit hoher Genauigkeit am Patienten zu applizieren. In der vorliegenden Arbeit wurde ein neues Modell entwickelt, mit dem die bei der TomoTherapie applizierte Dosisverteilung vorhergesagt wird. Das Modell kann im Rahmen der Qualitätssicherung für die Verifikation von Dosisverteilungen verwendet werden. Das Modell basiert auf einem sogenannten "Energiedepositions-Kernel" und kann die Dosisverteilung in einem homogenen Medium für Felder bis zu einer Größe von nur ∼2 mm Durchmesser mit hoher Genauigkeit vorhersagen. Das Modell berücksichtigt zwei wesentliche Einflüsse auf die Dosisverteilung kleiner Felder: (i) die räumliche Ausdehnung der Strahlenquelle und (ii) den Verlust des Sekundärelektronengleichgewichts (SEG) innerhalb des Feldes. Die Form der Strahlenquelle wurde mittels der "Schlitz-Methode" unter zusätzlicher Anpassung eines Kollimator-Faktors rekonstruiert. Das fehlende SEG wird durch einen poly-energetischen Pencil-Beam Kernel berücksichtigt. Das Modell wurde für einen 6 MV Photonenstrahl an einem konventionellen Linearbeschleuniger erfolgreich validiert. Das Werkzeug für die Dosisverifikation wurde für einfache Strahlanordnungen untersucht. Zusätzlich wurde es verwendet um den Einfluss der zeitabhängigen Bestrahlungsparameter auf die Integraldosis zu bestimmen. Das entwickelte Modell ermöglicht die Analyse der Leistungsfähigkeit von Bestrahlungsgeräten beim applizieren kleiner Bestrahlungsfelder in der Strahlentherapie. Darüber stellen die Modellberechnungen eine Alternative zur konventionellen Dosimetrie in kleinen Feldern dar.

Abstract

Development of a dose calculation model as a supplemental quality assurance tool for TomoTherapy

Helical TomoTherapy® is a state-of-the-art delivery technique used in photon radiotherapy. This system relies on the superposition of many small fields to precisely administer the prescribed dose to the patient. This thesis presents a new model that predicts dose distributions delivered by TomoTherapy. The model may be used within a dose verification tool for quality assurance purposes. It is based on so-called "energy deposition kernels" and can accurately predict dose distributions in a homogeneous medium for a broad range of field sizes, down to ∼2 mm in diameter. The model takes into account the two main effects that influence the dose distribution in small fields: (i) the spatial extension of the radiation source and (ii) the loss of charged particle equilibrium (CPE) within the field. The shape of the source is determined by a combination of a "slit-method" reconstruction and a collimator factor fitting procedure, whereas the loss of CPE is taken into account by the use of a poly-energetic pencil beam kernel. The model was successfully validated for a 6 MV photon beam produced by a conventional linear accelerator. The dose verification tool was evaluated for simple beam configurations and used to study the influence of temporal beam parameter variations on the integral dose. The developed model allows to evaluate the performance of devices applying narrow photon beams in the treatment delivery. Furthermore, it can be used as an alternative to the conventional dosimetry of small fields.

Contents

List of Acronyms

3DCRT Three-Dimensional Conformal Radiotherapy

AAPM American Association of Physicists in Medicine

CF Collimator Factor

CAX Central AXis

CPE Charged Particle Equilibrium

CT Computed Tomography

DDK Dose Deposition Kernel

DQA Delivery Quality Assurance

DTA Distance To Agreement

ESTRO European Society for Therapeutic Radiology and Oncology

FFT Fast Fourier Transform

FWHM Full Width at Half Maximum

HU Hounsfield Units

IAEA International Atomic Energy Agency

IC Ionization Chamber

IMRT Intensity-Modulated Radiation Therapy

IGRT Image-Guided Radiation Therapy

KERMA Kinetic Energy Released to MAtter

LAC Large Area Chamber

MLC Multi-Leaf Collimator

MVCT Mega-Voltage Computed Tomography

OAR Off-Axis Ratio

OF Output Factor

PDD Percentage Depth Dose

PBK Pencil Beam Kernel

QA Quality Assurance

SAD Source-Axis Distance

SCD Source-Collimator Distance

SD Standard Deviation

SSD Source-Surface Distance

TAR Tissue Air Ratio

TERMA Total Energy Released to MAtter

TG Task Group

TPR Tissue Phantom Ratio

TPS Treatment Planning System

TRS Technical Report Series

"The important thing in science is not so much to obtain new facts as to discover new ways of thinking about them."

Sir William Bragg (1862-1942)

1 Introduction

In the year 2008, 12.4 million new cancer cases were diagnosed worldwide (Boyle and Levin, 2008). About 50% of these patients will require radiation therapy at a certain point of their illness, either alone or in combination with other cancer treatments (Delaney et al., 2003). The use of therapeutic radiation dates back to more than 100 years ago, shortly after the German physicist Wilhelm Conrad Röntgen discovered the "x-rays", in 1895. In the early 1920s, the treatment of patients with x-ray radiation was already incorporated into the clinical routine. During the first half of the twentieth century, radiotherapy treatments were almost exclusively targeted at (mostly superficial) inoperable tumors. Even though the science behind radiation was sound, the technological barrier at that time did not allow deep and accurate radiation treatments. Later on, the use of high energy photons from radioactive isotopes (^{60}Co, ^{137}Cs) and linear accelerators in medicine, together with the introduction of the Computed Tomography (CT) by Godfrey Hounsfield in 1971, opened a new era in radiation therapy. CT allowed the replacement of the two dimensional treatments by accurate Three-Dimensional Conformal Radiotherapy (3DCRT), which permits a better targeting of the tumor while minimizing the dose to the adjacent healthy tissues. Perhaps one of the most important developments in the field was the advent of Intensity-Modulated Radiation Therapy (IMRT). This concept, developed in the early 1980s (Brahme et al., 1982), conforms the prescribed dose to any shape of the target in a three dimensional way, taking the concept of 3DCRT to the next level. This new technique opened the possibility to safely escalate the prescribed dose to the tumor and to re-treat patients that were previously irradiated (a comprehensive review on IMRT can be found in Webb 2001). Nowadays, the latest revolution in radiotherapy is the so-called Image-Guided Radiation Therapy (IGRT), which uses CT (dynamic) imaging to compensate for the inter- (or intra-) fractional tumor motion.

It has been recommended that the uncertainty in the dose delivered to a patient should remain below 3-5% (1 standard deviation, Wambersie 2001). Considering that the uncertainties associated with target delineation are still large (Giraud et al., 2002), these recommendations set high demands on the modeling of the beam.

Modern radiation therapy techniques make use of different beam modifiers (e.g., Multi-

Leaf Collimators (MLCs), micro-MLCs and stereotactic collimators) in order to achieve the desired geometrical accuracy in the delivered dose to the target. One of the drawbacks in the use of such techniques, is that the treatment is typically based on the superposition of many small fields that define very sharp dose gradients, which carries a number of issues that need to be considered from the dosimetric and modeling points of view. The most important effects to consider under these conditions are: the partial occlusion of the radiation source and the loss of Charged Particle Equilibrium (CPE) within the field.

Under small field conditions the dosimetric methods used to acquire the input data for a particular Treatment Planning System (TPS) must be carefully selected in order to reduce the uncertainties in the dose calculation. The dosimeter used for this purpose should have an adequate lateral resolution and tissue equivalence (Calcina et al., 2007). Moreover, it is recommended this data should be measured with more than one dosimetric system (Pappas et al., 2008). The use of small fields is also demanding in the modeling aspect. The factor-based calculation methods that do not model secondary particle transport are not well suited for accurate beam characterization in these conditions. This type of models are also limited in terms of flexibility, due to the impossibility of handling the almost unlimited number of possible field shapes used in IMRT. The small field conditions require that the dose calculation is able to include the source extension and the secondary particle transport.

Another component to be considered is the planning technique. Nowadays, the optimal patient treatment is obtained using the inverse-planning technique (instead of the traditional forward planning) that uses user defined constraints ("cost functions") for the dose to the target and to the structures at risk, in an iterative process, to obtain the "best" plan. Inverse planning makes the planning process much more efficient, but the optimized parameters obtained for the treatment are no longer intuitive. This entails the requirement of a better understanding of the beam delivery and Quality Assurance (QA) processes associated, underlining the importance of independent dose calculation methods to verify the output of a planned treatment. International organizations, such as the European Society for Therapeutic Radiology and Oncology (ESTRO) (Belletti et al., 1996) and the American Association of Physicists in Medicine (AAPM) (Kutcher et al., 1994; Fraass et al., 1998), have recommended the inclusion of this practice as part of a comprehensive clinical QA program. An independent dose calculation should be performed prior to the treatment in order to detect and prevent possible flaws in it. Ideally, these calculations should rely on input data that is independent from the planning system.

The aforementioned issues motivated the development a beam model applicable to a broad range of field sizes (including narrow beams), that could be used to provide a supplemental dose verification procedure for the QA program of a TomoTherapy unit.

Hi·ART TomoTherapy® is an innovative IMRT dedicated system that integrates inverse treatment panning, image-guided patient positioning and dose delivery. It has a short linac, mounted in a ring gantry that allows to deliver the dose to the patient in a helical pattern (analogous to a spiral CT). The first clinical use of TomoTherapy was registered in 2002 (Mackie, 2006). Four years later, the University Hospital of Heidelberg acquired the first TomoTherapy unit in Germany, treating the first patient in July 2006. Therefore, it is of particular interest to study this delivery system and the challenges related to the use of small fields and to the implementation of a QA program for it.

This work is mainly focused on the implementation of a dose verification tool applicable to the Hi·ART TomoTherapy System, based on a dose model (algorithm) developed to

yield highly accurate dose distributions in water for narrow beams. Within this frame, the dosimetric challenges and the demands in dose modeling and QA, posed by the advent of non-standard beams in radiotherapy, are discussed; with particular interest in TomoTherapy. A summary of the dosimetric QA program for the TomoTherapy unit, applied at the University Hospital of Heidelberg, is also included in this document.

The independent dose calculation tool presented in this thesis does not only help to ensure the patient safety and the success of the treatment, as being part of the comprehensive QA of the system, but can also be used to study the uncertainties related to the single processes involved in the helical delivery technique. The importance of such independent calculations in complex delivery techniques used in modern radiotherapy should be underlined, as the success of the treatment in these cases depends on the performance and synchrony of many individual components.

Following this introductory chapter, Chapter 2 presents the basic physical concepts used in this thesis together with a description of the development and validation of an independent dose verification tool for TomoTherapy. The presented dose calculation algorithm especially focuses in the main effects to be considered for narrow beams (the spatial extension of the source and the loss of secondary charged particle equilibrium). Therefore, a detailed description on how these effects are taken into account is also given. The main results of this work are presented in Chapter 3: starting from the basic parameters required by the model, followed by the validation results in a conventional linac, to finish with the application to TomoTherapy delivered dose distributions. A study of the overall uncertainty associated to random and systematic variations of specific parameters within the treatment is also included. In Chapter 4, a critical assessment of the dose verification tool, regarding its usability and limitations, is given. The individual results of the validation and implementation processes are also discussed throughout this chapter. At last, a summary and outlook for this work are presented in Chapter 5.

"Theory guides. Experiment decides."

An old saying in science

2 Materials and Methods

This dissertation, deals with modern dose delivery techniques used in photon radiotherapy and the challenges associated with the clinical implementation of these state-of-the-art techniques. In particular, the case of TomoTherapy was studied. To prepare a framework for this work, this chapter begins with an overview of the basic physical concepts, methods and considerations related to the determination of dose delivered by clinical photon beams. Then, the development of a beam model that can handle small field conditions commonly used in modern radiotherapy, is described. The methods used to validate such a model are also included. Later in this chapter, a description of the TomoTherapy system and of its current clinical QA program, carried out at the University Hospital of Heidelberg, is given. Finally, the implementation of the model into a dose verification tool for TomoTherapy delivered distributions is presented.

2.1 Clinical photon beams: basics of energy deposition

The energy deposited (by ionizing radiation) in a medium per unit mass is called absorbed dose and has the unit J/kg or Gray (Gy). In general, the calculation of absorbed dose is performed in water (considering that the human body is composed by ∼60% of water). The absorbed dose in different tissues is determined as a correction to the dose in water (Schneider et al., 2000), depending on their electron densities.

Photons are indirectly ionizing particles, therefore, they do not deposit their energy in the patient directly, but through interactions with the atoms in the medium encountered in their paths. Most of the energy of the primary photons is transferred to secondary electrons. These secondary electrons are the ones that release the energy to the medium, mainly by scattering interactions.

In the ideal case, the photons would first interact with the patient. However, the presence of many components of the linear accelerator in the vicinity of the x-ray source (e.g., collimators) or directly between the source and the patient (e.g., flattening filter), leads to charged particle contamination of the photon beam and dose scattering, which can represent 5-15% of the total dose, as shown by Ahnesjö (1994). As these head-scattered

photons differ in energy and direction from the primary beam photons, it is useful to introduce the concepts of primary and scatter dose, associated with the dose deposited by primary and head-scattered photons, respectively.

2.1.1 Energy deposition mechanism

The energy imparted to matter from a clinical photon beam can be characterized as a two-step process: (1) the transfer of energy from photons to charged particles in the medium and (2) the charged particles transfer their energy to the medium along their tracks.

(1) The TERMA/KERMA step: A key concept in the photon dose deposition process is the energy fluence (Ψ) or the Total Energy Released to MAtter (TERMA). At each point in the medium (r), the TERMA (T) corresponds to (Ahnesjö et al., 1987)

$$T(r) = -\frac{1}{\rho(r)} \nabla \cdot \mathbf{\Psi}(\mathbf{r}), \tag{2.1}$$

where $\rho(r)$ is the density distribution in the medium, and $\mathbf{\Psi}(\mathbf{r})$ is the vectorial energy fluence. Considering that the change in energy fluence is most rapidly in the direction of movement, in the mono-energetic case, the TERMA differential in energy, $T_E(r)$, is given by

$$T_E(r) = -\frac{1}{\rho(r)} \frac{d\Psi_E}{dl} = \frac{\mu}{\rho}(E, r)\, E\, \Phi_E(r), \tag{2.2}$$

where Ψ_E is the fluence differential in energy, l is the path length of the primary photons in the direction of motion, $\mu/\rho(E, r)$ is the mass attenuation of the photons with energy E at a point r, and $\Phi_E(r)$ is the primary photon fluence differential in energy at the position r. The latter can be obtained as

$$\Phi_E(r) = \Phi_E(r_0) \left(\frac{r_0}{r}\right)^2 e^{-\int_{r_0}^{r} \frac{\mu}{\rho}(E,l)\, \rho(l)\, dl}, \tag{2.3}$$

where $\Phi_E(r_0)$ is the primary photon fluence at a reference point r_0 (on the surface of the medium), the exponential term expresses the attenuation of the beam in the motion path $l = r - r_0$.

The TERMA accounts for the total energy transferred from the photons to the medium. This energy transfer can occur through different interaction mechanisms, depending on the energy of the beam and the characteristics of the medium (density and atomic number). Considering homogeneous water as the irradiated medium, the dominant regime in the range of energies used in therapeutic photon beams is the Compton effect. Pair production and photoelectric absorption effects also take place, but with a much lower probability of occurrence. Nevertheless, these low probabilities increase with the increase of energy in the case of pair production, and with the increase of atomic number of the medium in the case of photoelectric effect. If CPE is established, the deposited dose and TERMA are linearly related (Boyer et al., 2004).

The Kinetic Energy Released to MAtter (KERMA) (<TERMA) accounts for the kinetic energy that the launched charged particles (recoil electrons) acquire after the primary photon interactions (only the energy released to charged particles is

accounted). Most of this energy is deposited quasi-locally due to multiple Coulomb collisions with neighboring orbital electrons or atomic nuclei (collision KERMA). However, a small fraction of the energy will be carried away from the primary interaction site through radiative events such as bremsstrahlung and electron-positron annihilation (radiative KERMA). The collision KERMA accounts for the first part of the energy deposition mechanism: the energy transfer from non-charged particles to charged particles.

(2) The DOSE step: The inelastic collisions, in which a secondary electron transfers some of its energy to an orbital electron, represent the final mechanism of dose deposition in matter. The amount of energy transferred to the orbital electron will produce the excitation or ionization of the atom. If ionization occurs, the liberated electron will continue the process of excitation/ionization of atoms in its track until it stops, when all its kinetic energy is lost.

2.1.2 Charge particle equilibrium

By definition, CPE exists for a volume v if every charged particle of a given type and energy leaving v is replaced by an identical particle of the same energy entering it (Berger and Seltzer, 1982). Under these conditions, the primary dose becomes exactly equal to the collision KERMA.

To achieve a perfect CPE state using clinical photon beams is virtually impossible. The condition of CPE is lost in regions very close to the radiation source, the fluence will not be uniform due to the $1/r^2$ factor accounting for the divergence of the beam, or close to the interface between two materials of very different densities (e.g., tissue/air or soft-tissue/bone). The CPE is also lost when there is a magnetic or electric field induced that deviates the charged particles from their original path (valid for some radiation detectors) or for high energy radiation, as used in therapeutic photon beams (Hobbie and Roth, 2007). Easier to achieve is a state of transient-CPE that occurs when the energy deposited in the medium is proportional to the kinetic energy transferred to it. This condition is fulfilled in regions deeper than z_{max}, which corresponds to the forward range of the secondary electrons liberated from the primary photon interactions. From here on, the state of transient-CPE will be referred to just as CPE.

Dose calculation algorithms often assume a state of CPE simplify the calculations. The simplification is achieved by performing a so-called KERMA-approximation. In conventional 3DCRT, this assumption is valid in most of the cases as the field sizes used are big enough to provide this condition within the treated volumes. However, for narrow photon beams this approximation can be too coarse and may produce calculated distributions that do not reflect the delivered dose. As discussed by Das et al. (2008), the critical parameter to CPE condition is, rather than the forward range of the secondary electrons, their lateral range (corresponding to approximately 1/3 to 1/2 of the forward range for energies lower than 10 MV, Boyer et al. 2004).

2.2 Dose calculation methods: general aspects

In this section, a summary of the dose calculation concepts relevant to this thesis is presented. For a comprehensive review on dose calculation methods see Ahnesjö and Aspradakis (1999) or Boyer et al. (2004).

In order to anticipate the outcome of a radiation treatment, it is necessary to perform dose calculations. This should allow to determine the geometrical distribution and homogeneity of the dose to be delivered to the patient, ensuring a good coverage of the target and sparing of the organs at risk. The main requirements of the dose calculation algorithms are: high reliability, precision and accuracy in the determination of the dose, and high calculation speed (Schlegel and Mahr, 2007), if the purpose is treatment planning.

In earlier times, physicists manually calculated the dose to be delivered to the patient. These calculations were based on a set of beam parameters measured at different depths in a water phantom for quadratic fields and in the use of empirical formulas (Day, 1950) to correct for the differences between the water tank and the patient. These methods were called factor-based methods (also called correction-based methods).

The use of computerized methods to calculate dose distributions, started with the advent of CT. CT allows to obtain quantitative data on the anatomy of the patient, particularly on the different electron densities of the tissues (associated with the Hounsfield Units (HU)), which yielded an improvement on the geometrical accuracy of the calculations. With the increase of computing power, more sophisticated calculation methods were developed based on physical models. They are therefore called model-based algorithms. These methods, handle the primary and scatter components of the beam separately, using physical models of the beam and the deposition of energy in matter. Hence, they provide a good description of the changes in scattering due to variations in the beam shape and patient anatomy (Jeleń, 2007).

2.2.1 Factor-based calculations

In the factor-based algorithms (Cunningham, 1972; Thames, 1973; Sontag and Cunningham, 1977; Sontag et al., 1977; Sontag and Cunningham, 1978; El-Khatib and Battista, 1984) the dose is calculated by the multiplication of different factors that account for variations from the reference conditions (beam modifications and patient-related modifications) without explicit modeling of the transport of secondary electrons. The factors used for the determination of the dose include: Off-Axis Ratios (OARs), Output Factors (OFs), Percentage Depth Doses (PDDs), Tissue Air Ratios (TARs) and Tissue Phantom Ratios (TPRs), among others.

Factor based methods offer a conceptually simple approach to calculate dose distributions that has been widely used over the years for independent dose verification. However, there are some practical issues concerning this approach. The most important of them is that it is time consuming to measure all the parameters required to obtain a complete tabulated data set, which covers the entire range of possible configurations to be evaluated. Nevertheless, if the intended use of the method is to evaluate the dose in regions close to the central axis for simple field shapes, this approach can certainly be used. On the other hand, if one wants to evaluate the dose at arbitrary positions using complex field configurations (as commonly used in IMRT), the amount of data to be measured in order to cover the complete range of possible configurations becomes prohibitively large (Olofsson, 2006).

Facing the huge flexibility in the dose delivery of TomoTherapy, it was decided not to use the correction-based method for the dose calculations. Instead, a more sophisticated model-based method was used.

2.2.2 Model-based calculations

Within the model-based algorithms to calculate dose, two categories can be distinguished: the Monte Carlo calculations (highest accuracy, but long computation time) and the so-called kernel-based or convolution/superposition algorithms (Mackie et al., 1985). Kernel-based methods can model dose distributions very accurately and have the advantage of being faster than the Monte Carlo methods. In kernel-based methods, the delivered dose is assumed to be equal to the sum (or superposition) of elementary photon beam components. The distribution of energy imparted to a medium after the interaction with an elementary beam is called "kernel", hence, the name of the method. In this kind of calculations, two components are defined: (i) a primary (or ray tracing) component, which considers the energy transferred to the medium by photons and (ii) a secondary component, which brings into effect the transport and deposition of energy by the secondary particles. The primary component contains all the information regarding the beam shape and modulation, for which the geometry of the radiation system needs to be known. The other component is assumed to be independent from the geometric configuration of the system; it only depends on the spectrum of the photons and on the composition of the irradiated medium.

Depending on the "geometry" of the elementary beam, the kernel can receive different names. The most frequently used kernels are: the point-kernel (Figure 2.1(a)), which describes the deposition of energy after a single (mono-energetic) photon interaction in the center of an infinite medium, and the pencil-beam-kernel (Figure 2.1(b)), which describes the deposition of energy after the interaction of an infinitely narrow beam (or a finite size elementary beam) with a semi-infinite homogeneous medium.

The first step in the point-kernel calculations is to obtain the energy released in the medium due to the primary photon interactions considering the attenuation of the beam (this step is applicable to every model-based calculation). The second step is to calculate the dose by superposing the contributions of energy deposited around each interaction site described by the kernel. The kernels are usually calculated for mono-energetic beams, so knowledge on the beam spectrum is required. Although this concept is simple, there are many issues related to the implementation of this algorithm, including: long computation times, spectral variations, kernel variations due to heterogeneities and interpolation problems. Some of these problems (particularly the computation time) are solved by parameterizing point-kernels into conical sectors; this is the so-called "collapsed cone convolution approximation" (Ahnesjö, 1989).

A simpler and faster approach is used in the pencil-kernel calculations. The problem is reduced by one dimension, as the point kernels are already pre-summed in the direction of the incident beam. Using this method, the dose is computed by obtaining the fluence/TERMA (Figure 2.1(c)) over the field opening and then integrating the kernel contributions (Figure 2.1(d)). If the spectrum of the beam is not available, broad beam data can be used for the determination of the correct weighting of the mono-energetic components of the kernel.

The major limitation of the pencil beam kernel approach is the poor modeling of delivered dose distributions in the presence of lateral inhomogeneities. The pencil beam method can correct for the presence of inhomogeneities only in the forward direction by re-scaling the kernel. For the purpose of this work (implementation of a verification tool for dose distributions delivered in a homogeneous phantom), this limitation does not present a problem. Therefore, due to the theoretical simplicity, the pencil beam kernel approximation has been used as the dose calculation engine. All the distributions were

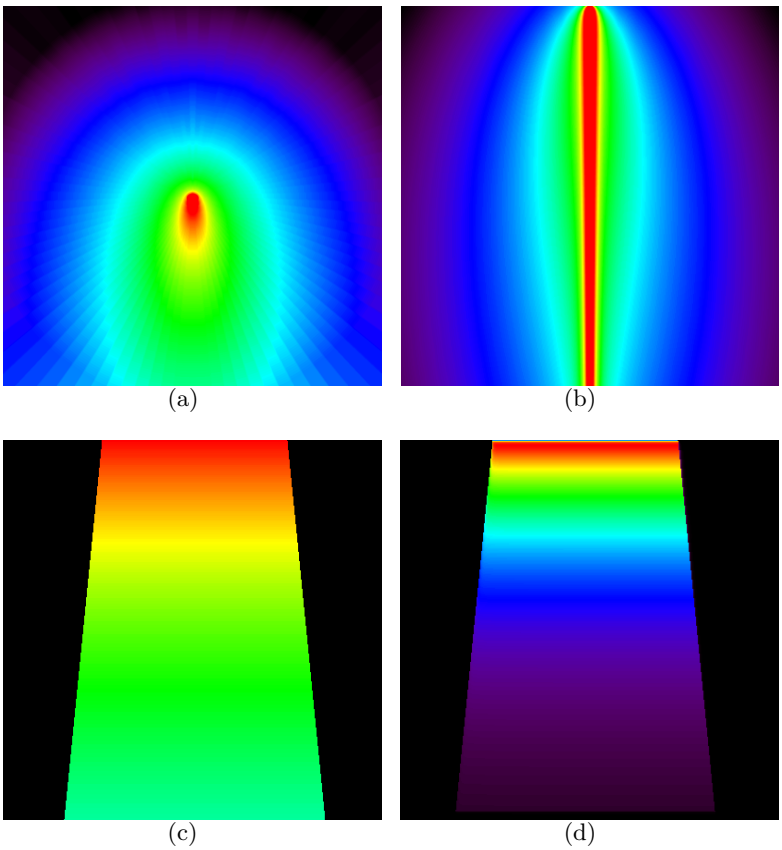

Figure 2.1: *Pencil beam kernel based dose calculation. (a) Mono-energetic point-kernel. (b) Poly-energetic pencil beam kernel, obtained after cumulating the point-kernels in depth, considering beam attenuation and spectrum weighting. (c) Fluence distribution for an open field, considering beam divergence. (d) Dose distribution, considering the transport of the secondary particles (convolution between the fluence and the pencil beam).*

calculated using water as the absorbing medium.

The Pencil Beam Kernel (PBK) can be obtained using different methods. These include experimental approaches (Ceberg et al., 1996; Storchi and Woudstra, 1996), a parameterized form (Nyholm et al., 2006) and Monte Carlo methods (Mohan and Chui, 1987; Ahnesjö and Trepp, 1991; Ahnesjö et al., 1992; Bourland and Chaney, 1992). In this work, a Monte Carlo based method was used. As the direct integration of the kernel over the field can be computationally exhaustive, it is assumed that the kernel distribution is space-invariant. Under this assumption, the calculation can be carried out using convolution techniques such as the Fast Fourier Transform (FFT) (Boyer and Mok, 1985), reducing significantly the number of operations to be performed. The details of the implementation of the PBK into the dose calculations are given in Sections 2.3.2 and 2.3.3.

PBK-based dose calculations (as any other model-based method) require an accurate determination of the lateral fluence distributions for the different field configurations. To obtain these distributions, there is an important effect to consider: the presence (or absence) of a flattening filter, used in most of the conventional linacs. This filter, as suggested by its name, is designed to produce a "flat" dose distribution at a certain depth in a water

phantom for a reference field size. This is accomplished by reducing the photon fluence in the central part of the beam, as a function of the off-axis distance, producing the so-called "horn-effect" (due to the resulting shape of the lateral fluence profiles for large fields, see Figure 3.8(b)). The absence of flattening filter (applicable to the TomoTherapy system, see Section 2.4.2), on the other hand, will leave the fluence for an open field unmodified, producing a cone-shaped lateral fluence distribution, as shown in Figure 2.11(a). A simple way to account for these filtering effects is to obtain a fluence profile for the biggest field size available and assume radial symmetry on the fluence distribution. The lateral photon fluence can be determined by taking into account, besides the filtering effect, the geometrical shape of the beam (for a given MLC/Jaws configuration), the effect of the spatial extension of the source and the head scatter contributions.

The scatter fraction coming from the treatment head can significantly contribute to the treatment beam. In this work, the head scatter contribution has been considered in the implementation of the "extended source" (that takes into account the focal spot size and the head scatter contributions, see Section 2.3.1). Nilsson and Brahme (1981) were the first to identify the sources of such contributions. These are: the scatter from primary collimators, the flattening filter, back-scatter to the monitor and forward-scatter from the secondary collimators.

Second order effects in the dose calculation engine are the spectral changes of the beam (e.g., off-axis softening) and kernel tilting to account for the beam divergence. The main reason for the spectral variations at off-axis positions is the flattening filter. Even though a conventional linac (which has a flattening filter) was used to validate the dose calculations, no corrections to account for this effect have been done. The justification of this decision is based on the consideration that this work aims to verify dose distributions delivered by the TomoTherapy system which lacks a flattening filter. It has been shown by Sharpe and Battista (1993) that the assumption of a parallel kernel can lead to significant errors in the determination of the dose for extreme configurations (large field size, high energy and short Source-Surface Distance (SSD)). However, they also found that this approximation was accurate enough in most of the clinically relevant configurations. Hence, no corrections are applied to account for this effect either.

2.2.3 Uncertainty considerations

The formal definition of the "uncertainty" of a measurement is: parameter associated with the result of a measurement that characterizes the dispersion of a value that could reasonably be attributed to the measurand (BIPM et al., 1995). Uncertainties are classified either as type A, if they can be assessed by statistical methods, or type B, if the assessment can not be done in a statistical way. Regardless of the method used for the determination of the uncertainties, if there is more than one parameter involved in the determination of a process, the individual uncertainties are usually combined in quadrature to estimate the overall value.

The accuracy requirements of the delivered dose in radiotherapy are related to the tumor and normal tissue reactions. It has been recommended that the overall uncertainty in the delivered dose to the patient should be less than 3-5% (1 Standard Deviation (SD)) (ICRU, 1976; Dutreix, 1984; Mijnheer et al., 1987). Many analyzes have shown that this is not an easy goal to achieve. From this fact arises the importance of the QA program, responsible for maintaining every step of the process within an acceptable tolerance.

Recent developments in external radiation therapy such as IMRT and IGRT allow

a very high conformity of the delivered dose to the target. However, large geometrical uncertainties are still associated to the delineation of the target volume and organs at risk (Leunens et al., 1993; Giraud et al., 2002). Therefore, very high demands on the precise dosimetric and geometrical determination of the dose delivered to the patient are set. Uncertainties in the dose determination can originate either from the (measured) input data required by the dose calculation algorithm, or from the algorithm itself, i.e., poor modeling, inadequate approximations, coarse calculation grid size and other limitations associated with either the basic algorithm or its use (Fraass et al., 1998).

In order to estimate the uncertainty requirements specifically for the dose calculation process, two approaches can be used. In the ideal case, the requirement should be derived from radiobiological data, according to the effect of dose variations in tumoral and normal cells. However, it is difficult to obtain quantitative data that can be used for this purpose, due to insufficient experiments and the variability in the tumor/tissue response to radiation (Boyer et al., 2004) among others. A more practical way to estimate the accuracy requirements of the dose calculation by itself is to identify and quantify the uncertainties associated with the dose delivery chain (Mijnheer et al., 1987; Ahnesjö and Aspradakis, 1999; Boyer et al., 2004), which results in a variety of criteria. Given the complexity of the plans and the dosimetric issues, there are no specific dose accuracy recommendations for IMRT. The AAPM guidelines (Ezzell et al., 2003) suggest that for single beams in low gradient regions, the agreement with measurements should be as good as it is required for conventional treatments (i.e., 2-4%). For typical complete treatment plans, the agreement with the measurement should be within 3-4% in high dose low gradient regions.

The acceptance criteria used in radiotherapy are often expressed (in terms of 1 SD) as a combination of dose deviation, in low dose gradient regions, and Distance To Agreement (DTA), in high dose gradient regions. These criteria are adopted simply because in regions with high dose gradients a small displacement results in a large dose deviation. The converse is valid for the geometrical DTA criterion. One way to asses these criteria is to calculate both of them individually and then select the smaller value for each evaluation point. A more practical approach, widely used in the evaluation of calculated dose distributions, is the gamma index concept developed by Low, Harms, Mutic and Purdy (1998). This concept combines the dose difference (global or local, as desired) and the spatial distance between the measured and evaluated points in a dose-distance space. The measure of acceptance is the multidimensional distance between measured and calculated values in the dose-distance space, scaled by the individual acceptance criteria. In the case of a 2-dimensional distribution, the acceptance criterion corresponds to the surface of an ellipsoid in the dose-distance space centered in the measured value to be evaluated. The resolution of the evaluated distribution should be 1/3 of the DTA criterion according to Low and Dempsey (2003), implying that the evaluation data may need to be interpolated. For clinical dose verification a combination of 3-5% dose difference and 3 mm DTA is commonly used (Low, Harms, Mutic and Purdy, 1998; Low and Dempsey, 2003; Winkler et al., 2005; Childress et al., 2005; Thomas et al., 2005; van Zijtveld et al., 2006).

The dosimetric uncertainties can be associated with the detector/readout system's sensitivity and response issues, output stability of the radiation system and geometrical inaccuracies in the alignment of the beam with the detector and/or the phantom.

2.3 Dose calculation method: establishment of a model applicable to small beams

Small fields, i.e., fields with a size comparable or smaller than the lateral range of associated secondary electrons, are increasingly used in radiotherapy. The most prominent example is their application in stereotactic radiosurgery. However, this statement also applies to larger fields that are composed of small beams, as used in IMRT. This has been particularly promoted by the clinical availability of recent developments, such as mini- or micro- MLCs on conventional accelerators and treatment units specifically designed for stereotaxy (GammaKnife, CyberKnife) or intensity modulated treatments (TomoTherapy).

A versatile model of small beams needs to overcome two problems:

(1) As long as the number of possible shapes of different small fields remains small (as it is the case for radiosurgery using a set of cylindrical collimators), the beam model required for dose calculation can simply be based on experimental input data such as PDDs, profiles or output factors for a small set of small fields. However, for IMRT, with an almost unlimited number of different small field shapes (patterns), it is difficult to apply the same approach.

(2) A beam model for small fields must be validated by experimental results, however, dosimetry of small fields is still a challenge. High dose gradients set constraints on the detector size, furthermore, composition effects and small positioning errors become relevant (Pappas et al., 2008; Das et al., 2008; Alfonso et al., 2008). Therefore, the use of new techniques has increased the uncertainty in clinical dosimetry. One example of this is the introduction of systematic errors in the treatment planning implementation, due to inaccuracies in the small field measurements (Crop et al., 2007). Additionally, for certain techniques, it has become very difficult, or even not possible (e.g., TomoTherapy), to perform reference dosimetry based on the available dosimetry protocols. These issues have concerned international organizations such as the International Atomic Energy Agency (IAEA). Indeed, efforts are currently being made by the IAEA to set the basis of new international recommendations in order to standardize the dosimetry for the new delivery techniques (Alfonso et al., 2008).

The model presented in this section explicitly takes into account the two main effects affecting the dose distributions for small field sizes. These are: (i) the fact that the source of radiation is not point-like but extended in space and that the partial blocking of it will have an impact on the penumbra of the field and beam output (Scott et al., 2008) and (ii) the lack of CPE conditions within the field when its size is comparable to the lateral range of the secondary electrons in the medium (Das et al., 2008). Considering the known geometry of the system and these two effects, lateral dose distributions and output factors in water can be well modeled by convolution techniques (Mackie et al., 1985).

The validation of the beam model was performed using a 6 MV photon beam of a Siemens Primus linac. Comparisons of measured versus calculated output factors and dose profiles are presented as tests of the algorithm.

This section is based on an article that has been published in a peer-reviewed journal (Caprile and Hartmann, 2009).

2.3.1 Determination of the spatial extension of the source

Several techniques for the determination of the intensity distribution of the radiation source have been used in the past (Munro et al., 1988; Treuer et al., 1993; Yang et al., 2002; Treuer et al., 2003; Yan et al., 2008), but perhaps the only one out of these that allows a quantitative and direct reconstruction of the source distribution is the "slit-method" presented by Munro et al. in 1988. This technique, coupled with an analysis of Collimator Factors (CFs) (output factors measured free in air), was used to reconstruct the "extended source" of the linac.

The extended source is defined as the projection of all primary photons and head scatter contributions into a common plane, perpendicular to the axis of the beam and located at the source position. This two-dimensional distribution is composed of an "inner" and an "outer" part. The inner part (focal spot) can be reconstructed by the slit-method. The outer part cannot be directly obtained from such measurements due to its very low contribution compared with the inner part. Therefore, it was indirectly determined from CFs measurements, assuming that the observed increase of the CFs with the field size can be attributed to photons originating from the extended source.

Inner part

The reconstruction of the focal spot is based on the measurement of strip-integrals of the source and the use of image reconstruction techniques (Munro et al., 1988). The principle is that using a slit-collimator and a radiation detector, it is possible to measure the radiation coming from a very small slit of the source (emitted in the forward direction). If this measurement is repeated at different positions, by linearly moving the collimator and detector in the direction perpendicular to the slit, a strip-integral of the source is obtained (an example strip-integral can be seen in the scatter plot shown in Figure 2.2(c)). Now, by measuring strip-integrals of the source at different angles (with the center of rotation aligned with the central axis of the beam) and making use of the central slice theorem (Gaskill, 1978) or other CT image reconstruction technique, it is possible to obtain the shape and size of the source.

The device used for the measurement of the strip-integrals (shown in Figure 2.2(a)) is composed of two slabs of lead/antimony of 200x70x48 mm^3 separated by a distance of 130 μm, forming a slit-collimator. A block of tungsten, with a drilled hole and an opening only in the direction towards the slit, is attached under the slit-collimator. It contains a solid state detector (diode type p, Model 6008, PTW Freiburg, Germany). The assembly is mounted on a dynamic base that can be moved linearly in steps of 0.05 mm with a total range of 4 cm. The base is fixed to a platform that can rotate 180° on its own axis in 3° steps. The field of view of the detector, as seen in Figure 2.2(b), is limited to the projection of the slit into the source plane.

The device was remotely controlled by a portable computer using a tool programmed with LabVIEW 8.2 (National Instruments Corporation, Austin, TX, USA) in the "G" programming language. This tool can synchronize the movement of the stage with the measurement of the diode for the selected integration time (Figure 2.2(c)). The detector position, the integration time and the measured charge at each scanning point are stored in an ASCII file for later processing and analysis. A scanning range of 40 mm, a step size of 0.1 mm and an integration time of 1 s were used for the measurement of the strip-integrals. The collimator was positioned with the top side at a distance of approximately

Figure 2.2: *Measurement of strip-integrals. (a) Custom made slit-collimator device for the measurement of strip-integrals of the source. (b) Schematic representation of the slit-collimator assembly and the radiation source, indicating the rotational and translational axis as used for the measurements. (c) Interface created to control the device and the data acquisition. It shows, on the bottom left panel a measured strip-integral of the source.*

50 cm from the source. The radiation field was set to a nominal value of 10x10 cm^2 (at the isocenter) for the linac and of 10x5 cm^2 for TomoTherapy.

There are many algorithms used in CT image reconstruction (Kopka and Daly, 1977). All of them yield a representation of the object, from which the strip-integrals were taken, that is not exempt of artifacts. For the reconstruction of the two-dimensional distribution of the focal spot, an iterative algorithm was selected. With this algorithm, it was easier to constrain the results to be physically valid, i.e., no negative values were allowed. The algorithm minimizes the function:

$$\chi^2(X) = \sum_{km} \frac{\left(\sum_{ij} F_{ij}^{km} X_{ij} - p_{km}\right)^2}{\sigma_{km}^2}, \tag{2.4}$$

where p_{km} is the measured projection value at the m^{th} angle and k^{th} position with an uncertainty of σ_{km}, X_{ij} is the intensity of the focal spot in the pixel (i, j) at the source plane and F_{ij}^{km} is the fraction of X_{ij} projected into p_{km}.

Even though the detector is embedded in a tungsten block, scattered radiation coming from parts other than the slit (e.g., room scatter) is detected by the diode, increasing the measured signal from the source by an unknown amount. This effect is not negligible at the "wings" of the strip-integral. Therefore, the reconstructed distribution was considered to be part of the focal spot only down to ∼0.1% of the maximum intensity. The section of the reconstructed distribution where the intensity was less than ∼0.1% of the maximum was considered to belong to the outer part of the source.

Outer part.

The outer part of the source was obtained by fitting the calculated CFs, or collimator scatter factors (S_c) in Khan's notation (Khan et al., 1980), to the measured values. The unnormalized CFs were calculated simply as the integral of the "visible" part of the extended source from the point of view of the detector, as follows

$$CF(F_x, F_y, l_m) = \int_{-lim_x}^{+lim_x} \int_{-lim_y}^{+lim_y} S(x', y')\, \mathrm{d}x'\, \mathrm{d}y', \tag{2.5}$$

where F_x and F_y indicate the field size at the measurement plane in x and y direction respectively, l_m is the distance from the source to the detector (located on the central axis of the beam) and S is the two-dimensional intensity distribution of the extended source. lim_x and lim_y are the integration limits, defined by the projection of the collimator edges to the source plane. This projection requires that the positions of the collimators used to produce the field are known. They are obtained simply as

$$\begin{aligned} lim_x &= \frac{F_x}{2} \cdot \frac{l_{cx}}{l_m - l_{cx}} \\ lim_y &= \frac{F_y}{2} \cdot \frac{l_{cy}}{l_m - l_{cy}}, \end{aligned}$$

where l_{cx} and l_{cy} are the distances from the source to the closer edges of the MLC and the Y-Jaws respectively.

Figure 2.3 provides a graphical representation of the previously described CF calculation process. Measured CFs for quadratic fields (ranging from 2 to 40 cm in side length) were obtained using a photon diode located at 100 cm from the source with an appropriate brass build-up cup.

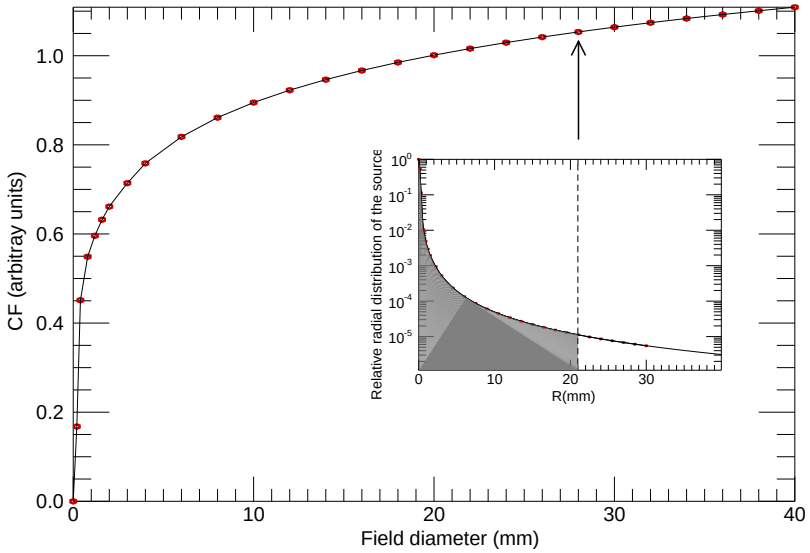

Figure 2.3: *Graphical representation of the CF calculation.*

2.3.2 Determination of the pencil beam kernel using Monte Carlo techniques

Proper modeling of dose distributions for small fields requires not only the source extension to be taken into account, but also the non-CPE conditions. To cope with these conditions, the lateral spread of the energy in the medium must be accounted for. For this purpose, a poly-energetic PBK, calculated using Monte Carlo simulations, has been used.

The poly-energetic PBK describes the dose deposition in a semi-infinite medium due to the interaction with an infinitely narrow beam (see Figure 2.1(b)). Therefore, it can be used to describe the non-equilibrium situation.

The PBK was calculated from mono-energetic point kernels or Dose Deposition Kernels (DDKs) and the weights of the energy spectrum of the beam as

$$PBK(x,y,z) = \frac{\int_0^{E_{max}} \Phi_E \int_0^{\infty} e^{-\mu_E z'} DDK(E,x,y,z-z')\,\mathrm{d}z'\,\mathrm{d}E}{\int_0^{E_{max}} \Phi_E\,\mathrm{d}E}, \tag{2.6}$$

where E_{max} is the maximum photon energy, μ_E is the linear attenuation coefficient in water for the energy E and Φ_E is the component from the energy spectrum for the energy E.

The DDK describes the dose deposition in an "infinite" medium after a single primary photon interaction event. The photon-medium interaction is forced to occur in the center of the medium (see example distribution in Figure 2.1(a)). DDKs can be obtained directly from Monte Carlo simulations using the EDKnrc calculation tool (Mackie et al., 1988; Mainegra-Hing et al., 2005) from the EGSnrc code system (National Research Council,

Ontario, Canada). The geometry used by the EDKnrc code to store the energy deposited is shown in Figure 2.4. Using the simulation parameters given in Table 2.1, mono-energetic DDKs for the PBK calculation were obtained.

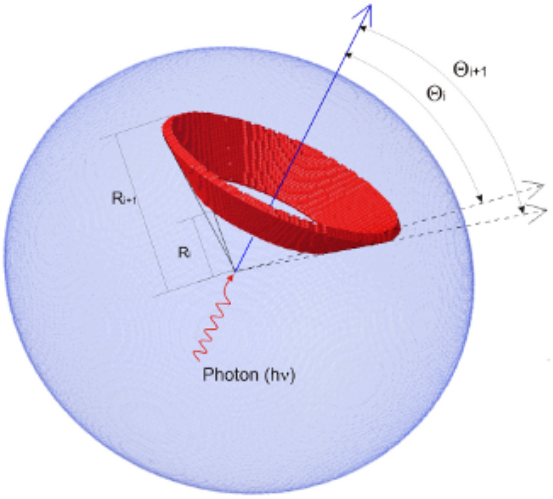

Figure 2.4: *Geometry used by the EDKnrc code. It represents a sphere of homogeneous water (light blue volume). Mono-energetic photons are forced to interact in the center of it. The energy deposited is stored in voxels (red volume) that are defined by the intersection between a series of cones (48) and spherical shells (24). It is assumed that the deposition of energy has rotational symmetry with respect to the axis defined by the photon trajectory.*

The weights of the spectrum were taken from Mohan's spectrum for a 6 MV beam (Mohan et al., 1985) as a first approximation. Then, a fine tuning was performed by fitting a calculated depth profile to the measured depth profile, since the dose from the individual energy bins contributes linearly to the final dose (Schlegel and Mahr, 2007). The function to be minimized was the following:

$$\chi^2(\Phi_E) = \sum_z \left(D(z) - \sum_{E=0}^{E_{max}} \Phi_E \cdot D_E(z) \right)^2 , \tag{2.7}$$

where D(z) is the measured PDD, and $D_E(z)$ is the calculated dose deposited at the central axis by a mono-energetic beam using the mono-energetic dose kernel. The Φ_E that minimize the χ^2 function were used as the new spectrum weights for the dose calculations.

The PDD for the 6 MV beam of the linac was measured for a reference field (10x10 cm^2) with a 0.125 cm^3 ionization chamber (Model 31010, PTW Freiburg, Germany).

2.3.3 Planar dose calculations

As previously mentioned, the dose calculations were performed using a PBK-based algorithm. Two-dimensional dose distributions in the plane perpendicular to the central axis were obtained as follows (Treuer et al., 1993):

First, a measured fluence distribution for the biggest field size available at a reference distance from the source (100 cm) is obtained. This distribution is used to correct for the

Table 2.1: *Parameters used in the Monte Carlo simulation of DDKs (based on Rogers et al. 2001)*

Parameter	Description	Value
	Monte Carlo inputs	
NUMBER OF HISTORIES	Number of initial photon interactions	$1 \cdot 10^6$
IFULL	Type of calculation. Options are: #(0) Calculate dose in cavity (if defined) #(1) Calculate and output EDK's #(2) Calculate and output dose #(3) Calculate and output EDK's and dose	#(2) Calculate and output dose
	Geometrical inputs	
NUMBER OF CONES		48
ANGLES	Angles defining the different cone openings (°)	θ=$i \cdot 3.75$ with $i = 1, 2, ..., 48$
NUMBER OF SPHERES		24
RADII	Radii defining the different spherical shells (cm)	r=0.05,0.1,0.15,0.2,0.25,0.3,0.4,0.5,0.6,0.8,1.0,1.5, 2.0,4.0,6.0,8.0,10.0,15.0,20.0,25.0,30.0,40.0,50.0,60.0
	Source inputs	
INCIDENT PARTICLE	Photons, electrons or positrons	Photons
INCIDENT ENERGY	Mono-energetic or spectrum	Mono-energetic
INCIDENT KINETIC ENERGY	Only for mono-energetic (KeV)	E=$i \cdot 250$ with $i = 1, 2, ..., 24$
	Transport parameters	
ECUT	Electron kinetic energy cut-off (MeV)	0.521
PCUT	Photon energy cut-off (MeV)	0.001
ESTEPE	Maximum fraction of kinetic energy loss per step	0.02

lateral variation of the photon fluence due to the presence of the flattening filter (the horn-effect). This distribution, Φ_0, is corrected considering the divergence of the beam when the calculation is performed at distances from the source different than the one where it was measured. To take into consideration the shape of the beam, Φ_0 is modulated by an aperture function A: defined by a value of one inside the field (i.e., the projected collimator edges at the measurement plane) and zero elsewhere. Then, the modulated fluence is convolved with the extended source S, yielding the "corrected" primary fluence (schematically shown for different depths in Figure 2.1(c))

$$\Phi(x,y,z) = c_x c_y \int\int_{-\infty}^{+\infty} [A\Phi_0](x',y',z) S(c_x[x-x'], c_y[y-y']) \, \mathrm{d}x' \, \mathrm{d}y', \tag{2.8}$$

where c_x and c_y are scaling factors ($c = (l_m - l_c)/l_c$) that account for the distances between the source and the measurement plane (l_m) and the source and the collimator (effective edge) plane (l_c).

Finally, the dose distribution (D) is obtained by convolving the corrected primary fluence (Φ) with the PBK (schematically shown for different depths in Figure 2.1(d)), at a measurement depth (d) as

$$D(x,y,z;d) = \int\int_{-\infty}^{+\infty} \Phi(x',y',z) PBK(x-x', y-y', d) \, \mathrm{d}x' \, \mathrm{d}y'. \tag{2.9}$$

Dose calculations were performed in a virtual homogeneous water phantom using cartesian coordinates with a grid of 0.1x0.1 mm^2 for circular fields, and of 1x1 mm^2 for quadratic fields. A schematic representation of the different steps involved in the planar dose calculation process is shown in Figure 2.5.

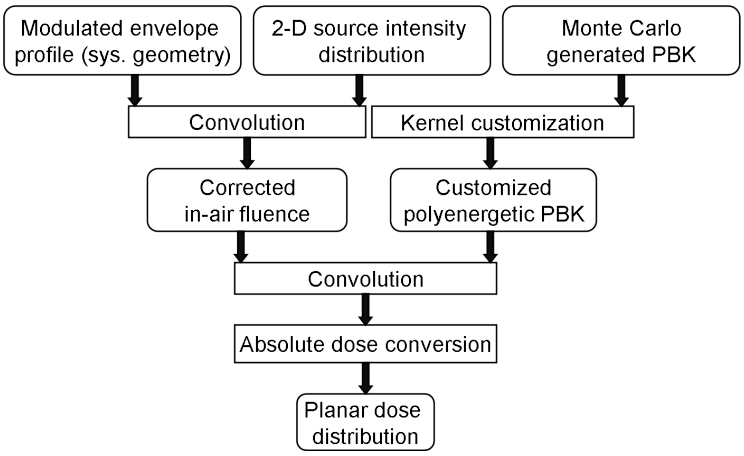

Figure 2.5: *Planar dose calculation flowchart (based on Yan et al. 2008).*

2.3.4 Test of the model

The model was tested by comparing measured and calculated planar dose profiles and output factors OFs for two collimator geometries: circular and quadratic, in a broad range of field sizes. Circular fields were generated by "add-on" cylindrical collimators used for radiosurgery (shown in Figure 2.6), with diameters ranging from 1 to 20 mm, positioned at a Source-Collimator Distance (SCD) of 59 cm. Quadratic fields, generated by the

inherent system (i.e., the MLC collimation in X direction and Y-jaws in the perpendicular direction), ranged from 0.5 to 40 cm in side length. Measurements were performed in a water tank (Model MP3, PTW Freiburg, Germany) using a photon diode. Dose profiles and OFs were measured at a SSD of 100 cm, at 1.5 cm depth in water.

(a)

(b)

(c) PTW ©

(d) PTW ©

Figure 2.6: *Components used to create the circular fields and detectors used in the validation. The collimators were inserted in the holding device and this, mounted on the linac. (a) Circular collimators. (b) Collimator holder.(c) Diode detector. (d) Parallel plate chamber, called Large Area Chamber (LAC).*

OF measurements for circular fields were done using two different methods. Directly by diode measurements, and indirectly by a combination of diode and parallel plate chamber (10.5 cm^3 Bragg Peak chamber, model 34070, PTW Freiburg, Germany) measurements. This method was developed by Sánchez-Doblado et al. (2007) and has the advantage of being less sensitive to positioning displacements. Using this method the OFs are obtained as

$$OF_i = \frac{D_i^{LAC}}{D_{10x10}} \cdot \frac{A}{I}, \tag{2.10}$$

where OF_i is the output factor for the field i, D_i^{LAC} is the measured dose for the field i using the parallel plate chamber (LAC: Large Area Chamber), D_{10x10} is the dose measured at the central axis for the reference field, A is the effective area of the LAC and I is the integral of the relative two-dimensional dose distribution over the effective area of the chamber. Sánchez-Doblado et al. obtained I using a combination of three films irradiated with a different amount of MUs (low, medium and high) in order to accurately determine the relative distribution. In this work, the film combination method was replaced by a one-dimensional profile measured across the field, assuming radial symmetry (see Figure 2.7).

The gamma index (Low, Harms, Mutic and Purdy, 1998) was used as an evaluation tool for the planar dose profiles. Individual criteria of 2% dose difference and 2 mm DTA were selected for the quadratic fields. For the circular fields the DTA criterion was tightened to 0.5 mm. The dose criterion was defined globally throughout this study, i.e., the percent dose difference is considered in reference to the maximum dose, not to the

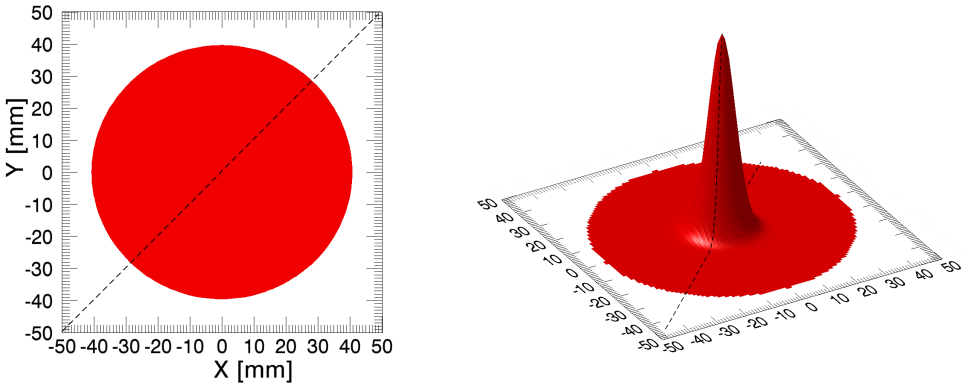

(a) (b)

Figure 2.7: *OF measurement procedure using a combination of parallel plate chamber and diode. (a) Representation of the chamber positioning within the field (circle) and a cross-field profile (dashed line). (b) Representation of a cross-field profile measured over the chamber area, used for the determination of the 2-D distribution (radial symmetry).*

local value.

2.4 Application to TomoTherapy: dose delivery verification tool

A dose calculation tool to be used in the verification of TomoTherapy delivered dose distributions was developed. The aim of this tool is for it to be implemented into the QA program of the system. It can also be used to study in depth the delivery technique and the influence of the different parameters in the final distribution. For this, it is necessary to understand the main characteristics of the delivery system that distinguish it from conventional teletherapy units. Furthermore, the dosimetric issues and QA challenges presented by the novel components of helical TomoTherapy need to be described in order to provide the context of this dose verification tool's usefulness.

2.4.1 Independent dose verification

The main reason to implement a dose verification tool is to have a method, in addition to the commercial TPS, to predict the outcome of a treatment. It is recommended (Kutcher et al., 1994) to verify the treatment parameters with an independent method, especially when the modality of treatment is complex (e.g., TomoTherapy). In such cases, small errors in the treatment parameters could lead to more serious consequences in the performance of the overall treatment than in the case of simpler techniques. Moreover, it is suggested that the patient verification should include both dose calculations and delivery verification measurements(Ezzell et al., 2003).

There are commercially available solutions for this purpose that can be used for conventional IMRT. However, the differences between the TomoTherapy delivery system and conventional IMRT (see Section 2.4.2) make them inadequate to be used for dose verification in TomoTherapy(Gibbons et al., 2009).

The dose verification tool developed allows to calculate distributions delivered by the TomoTherapy system to a homogeneous phantom, using input data that is independent of the TPS. This tool provides a supplemental QA procedure to verify the overall performance of the Hi·ART TomoTherapy system. Additionally, it allows to vary individual treatment parameters. This feature is particularly useful to study the influence on the overall treatment that the variation of parameters, such as output, gantry speed or couch velocity, would have. The calculated results were compared to measurements in static and dynamic modes. The performance of this method in inhomogeneous media has not been investigated yet and escapes from the scope of the presented work.

2.4.2 The Hi·ART TomoTherapy System®

The Helical TomoTherapy (TomoTherapy, inc., Madison, WI USA) is an IMRT dedicated system that delivers the treatment using a dynamic approach analogous to the one used in a spiral CT scanner. The system itself is also capable of acquiring Mega-Voltage Computed Tomography (MVCT) scans to be used as image guidance. The concept of tomotherapy, which literally translates to slice therapy, was developed at the University of Wisconsin in the late 1980s (Mackie, 2006). In 1993, the first helical TomoTherapy paper was published by Mackie et al. (1993). In this publication, the main concepts and components used in the modern unit were introduced for the first time (see Figure 2.8(a)).

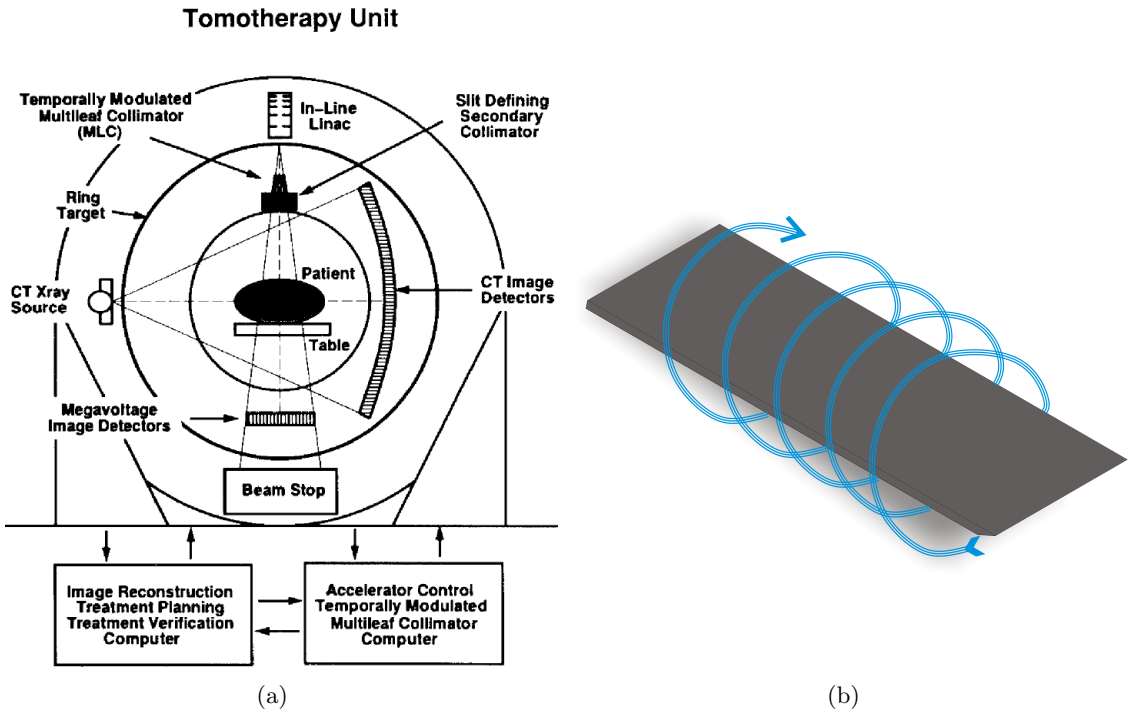

Figure 2.8: *Conceptual sketch of a TomoTherapy unit. (a) Schematic diagram of a helical TomoTherapy unit from Mackie et al. (1993). (b) Schematic representation of the helical delivery.*

The main characteristics of the modern unit (shown in Figure 2.9) that differ from the conventional teletherapy units, are described hereafter.

One of the most innovative features of TomoTherapy is the helical dose delivery (see

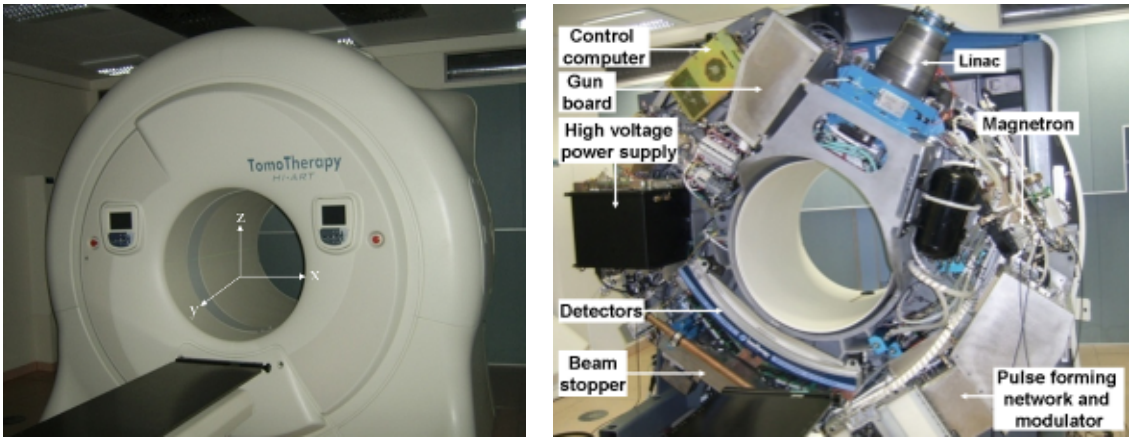

(a) (b)

Figure 2.9: *Helical TomoTherapy unit. (a) The TomoTherapy device with a reference coordinate system. (b) Main components.*

Figure 2.8(b)). Using this treatment technique, the patient moves linearly through the gantry bore at a constant velocity, while the gantry rotates around him/her at constant angular speed. During this process, the photon beam is switched on and is continuously modulated by the MLC. Prior to the treatment, the patient is positioned at a "virtual" isocenter, located 70 cm away from the machine isocenter in the longitudinal direction ("y" in Figure 2.9(a)). Then, an MVCT scan is performed and the displacements (and/or rotations) between planned and actual position of the patient are corrected for. After the repositioning of the patient (if necessary) the treatment can start.

The system has a short in-line linac mounted on a ring gantry that can rotate with a maximum speed of 10 seconds per rotation. The linac produces x-rays with a nominal energy of 6 MV at a dose rate of 8 Gy per minute in treatment mode. In scan mode, the same linac is used to produce the x-rays for the spiral MVCT. The nominal energy for this imaging mode is approximately 3.5 MV (Jeraj et al., 2004). The beam is collimated in the direction along the translational axis (Y axis in Figure 2.9(a)) into a fan beam, defined by a pair of jaws of up to 23 cm of tungsten (making the average leakage to be extremely low, below 0.01%). The fan beam's width ("thickness") can vary between 0 and 5 cm at the isocenter plane, which is located at a nominal distance of 85 cm from the source. In treatment mode, the field width in the longitudinal direction can only be set to 1, 2.5 or 5 cm at the isocenter. The modulation of the beam during the treatment is performed in the perpendicular direction (X axis in Figure 2.9(a))by a binary MLC (i.e., the leaves can be set to be either completely opened or completely closed).

The MLC has 64 dynamic leaves of 10 cm height and $\sim$2 mm in thickness (3 mm towards the patient direction and 2 mm towards the source, with tongue&groove of 0.15 and 0.3 mm respectively, Mackie 2006) made of 95% tungsten. The leaves are pulled open or pushed close by independent pneumatic pistons, organized in two blocks with 32 leaves each, facing each other. Each leaf is positioned at the same distance from the source with its face pointing towards it. This configuration allows opposite leaves to slide past each other without contact. The field width projected to the isocenter resulting from the opening of a single leaf is of only 6.25 mm, adding up to a maximum field width at the

isocenter of 40 cm (64 leaves opened) in the transverse (X) direction. The transit time of the MLC leaves is of only 20 ms.

The modulation of the beam is defined on rotational intervals. A single modulation pattern is determined over the course of a "projection" that comprises a gantry rotation arc of 7°. In this way, a complete rotation of the gantry corresponds to a total of 51 projections. The complete set of modulation patterns for a specific treatment is called "sinogram". For each projection of the treatment, it indicates the fraction of time that each individual leaf must be opened (see Figure 2.10). The total time that a single projection lasts can be determined by the "pitch": a key parameter set by the user prior to the treatment that is defined as in helical CT simply as,

$$p = \frac{L}{Y}, \tag{2.11}$$

where L is the longitudinal distance traveled by the couch in the course of one gantry rotation and Y is the fan beam width at the central axis (also set by the user to 1, 2.5 or 5 cm).

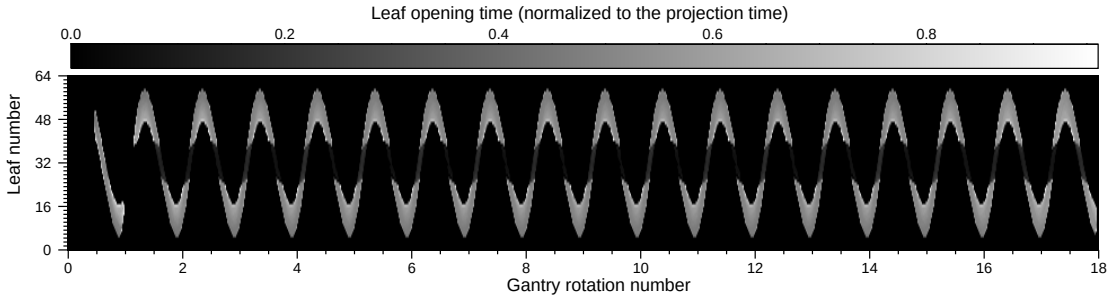

Figure 2.10: *Example sinogram. It indicates the fraction of time that each one of the MLC leaves remains open in one projection (51 projections = 360° gantry rotation).*

The variation of the pitch will influence the uniformity of the dose distribution in the longitudinal direction due to the beam junction. TomoTherapy delivered dose distributions can exhibit a thread-like pattern if the pitch is not optimally defined. This "thread effect" was thoroughly studied by Kissick et al. (2005).

A particular feature of the TomoTherapy device is that, in contrast to conventional linacs, it does not have a flattening filter. The lack of this component produces a dose profile across the field with a particular cone-like shape (see Figure 2.11(a)). This shape is unnoticeable in the longitudinal direction due to the restricted possible fan widths (5 cm maximum). The absence of flattening filter has two additional consequences: (i) there is a reduction of the extra focal radiation and (ii) the off-axis softening of the spectrum becomes a second order effect (as can be seen in Figure 2.11(b)), therefore no lateral spectral correction is needed for the beam modeling.

2.4.3 TomoTherapy dosimetry and QA

Conventional dosimetry codes of practice for high-energy clinical photon beams, such as the IAEA Technical Report Series (TRS)-398 (Andreo et al., 2000) and the AAPM Task Group (TG)-51 (Almond et al., 1999), set the reference measurement conditions to a nominal field size of 10x10 cm^2 at a distance of 100 cm from the source. The unique characteristics of TomoTherapy, in particular the short Source-Axis Distance (SAD) (of 85 cm

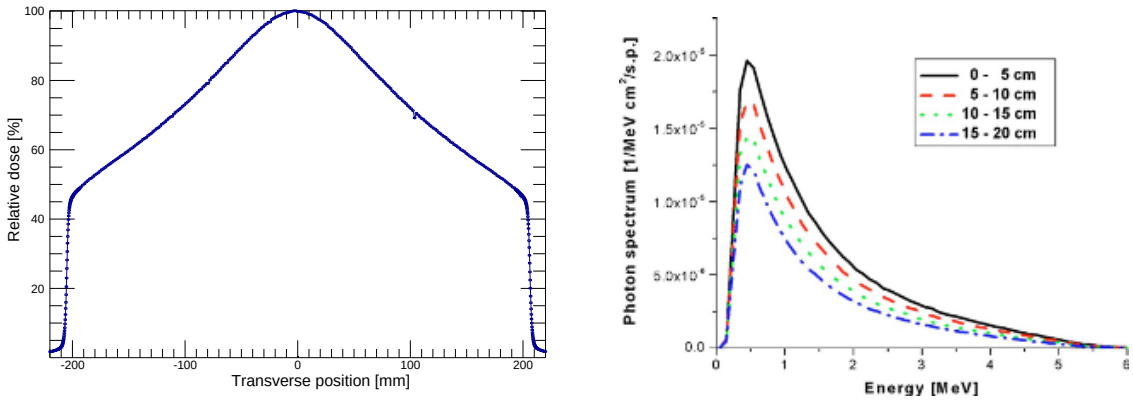

(a) (b)

Figure 2.11: *Helical TomoTherapy beam characteristics. (a) Normalized transverse profile of an open static field delivered by the TomoTherapy system. (b) Off-axis spectral dependence of the Helical TomoTherapy treatment beam. Note the very little off-axis spectral change: less than 5% with the average energy ranging from 1.43 MeV at the edge of the field to 1.49 MeV in the center (from Jeraj et al., 2004).*

in contrast to the typical 100 cm) and the field size limitation in the longitudinal direction (to a maximum of only 5 cm), do not allow the establishment of such reference conditions. Additionally, the use of multiple field patterns composed of many small fields inherently presents dosimetric (the measurement of absorbed dose to water in such conditions has not been standardized) and modeling (source occlusion and non-CPE conditions) challenges. This last issue is not only valid for TomoTherapy, but also for many of the emerging technologies in radiotherapy. The IAEA, in cooperation with the AAPM, has started working towards the development of guidelines and recommendations for reference dosimetry of small and non-standard fields, as an extension of the already established protocols based on absorbed dose to water (Alfonso et al., 2008). The development of the model presented in Section 2.3 is the approach used to deal with the non-standard fields.

There are several documents issued by international organizations that set the basis and give recommendations on the structure and management of a QA program in radiotherapy. These documents define the roles and responsibilities of every member of the radiotherapy team, in order to deliver to each patient the best and safest radiation treatment to achieve cure, long-term tumor control, or palliation (Kutcher et al., 1994; Belletti et al., 1996; Andreo and Ortiz-Lopez, 1997). These recommendations (although more than ten years old) are still valid in most of their aspects. However, if the specific QA recommendations for radiotherapy equipment (Kutcher et al., 1994; Nath et al., 1994; Boyer et al., 2001; Fraass et al., 1998) are considered, it becomes evident that they are inadequate for the new technologies used in radiation therapy and, thus, need to be quickly adapted to the rapidly changing needs of modern radiotherapy techniques (Palta et al., 2008*a*). It has been pointed out that the development of new QA programs should have a more rational, cost-effective and risk-based orientation (Williamson et al., 2008).

Currently, there is no absolute agreement on what is clinically acceptable in IMRT planning or delivery accuracy (Palta et al., 2008*b*). With the use of inverse optimization in IMRT, the results can no longer be interpreted intuitively, thus, a new dimension to the QA process (Van Dyk, 2008) had to be introduced. Therefore, each institution offering IMRT

must develop its own QA protocols and acceptance criteria for the treatment planning delivery.

The use of a helical delivery technique by the TomoTherapy system suggests that the QA procedures should also include dynamic tests performed in treatment conditions in order to verify the correct synchrony and performance of its components. The first guidelines for a QA program dedicated to helical TomoTherapy were written by Fenwick et al. (2004). These guidelines were based on the conventional linac QA schedule from the AAPM TG-40 and on procedures for sequential TomoTherapy QA previously described (Low, Chao, Mutic, Gerber, Perez and Purdy, 1998; Woo et al., 2003). They suggested daily, monthly, three-monthly and yearly schedules, gave detailed descriptions of the procedures testing the distinctive characteristics of the delivery system and discussed possible modification in the schedules once the technology would reach a more mature state. Two years later Balog et al. (2006) presented multifaceted daily and monthly QA procedures that were able to test most of the novel TomoTherapy features (MVCT image quality and dynamic delivery accuracy), besides the traditional beam output. These tests required the use of equipment (phantom and electrometer) with specific characteristics (offered by the vendor). To evaluate the performance (alignment, leakage, timing and leaf positioning error) of the binary MLC, Sarkar et al. (2007) developed a QA toolkit. This toolkit included the evaluation of seven MLC patterns that allow the users to test many of the mechanical and dosimetric properties of the TomoTherapy MLC. Broggi et al. (2008) studied the stability and constancy of the mechanical, dosimetric and geometrical performance of the system. The analysis of the temporal variation of the controlled parameters allowed them to propose modifications to the schedules of specific tests (mostly reducing the frequency of alignment tests and energy checks that showed good reproducibility) of their implemented clinical QA program. In most cases, the reference values of tolerance and action levels proposed by Fenwick et al. (2004) were found to be consistent with their experience. In the framework of "Quality Assurance of Radiation Therapy: The Challenges of Advanced Technologies" Symposium, Balog and Soisson (2008) proposed a detailed QA program for daily, monthly, and annual testing of the system.

In 2006, the University Hospital of Heidelberg in Germany acquired the first Hi-ART Helical TomoTherapy unit in the country. Since July 2006, more than 500 patients have been treated with this system. The use of TomoTherapy was justified by the following reasons: (i) complex tumor geometry, (ii) proximity of organs at risk or (iii) the need for image guidance for cases when the immobilization of the patient was problematic or when inter-fractional variations should be minimized (Sterzing et al., 2007). The QA program developed at this center is a dynamic process that continues evolving. In fact, in the frame of a cooperation agreement with the TomoTherapy company, new and more effective QA procedures are being developed. Currently, they are focused in making use of the detector data to evaluate the performance of the system. A summary of the current QA schedule is presented in Table 2.2. The program was divided into a daily, weekly, monthly, semestral, yearly and patient specific schedule. Here, a short description of the program, highlighting the "non-conventional" procedures, is presented.

Patient specific checks

The patient specific Delivery Quality Assurance (DQA) is performed by using a special feature included in the TPS platform. With this feature the user can replace the patient geometry, in which the planned dose was calculated, by a previously scanned verification

phantom (See Figure 2.12(a)). The program recalculates the dose to be deposited in the phantom geometry from the planned fluence for a specific fraction of the treatment. The DQA treatment is delivered to the phantom after registration of the correct positioning (an MVCT scan is performed and compared with the planned position) and repositioning (if necessary). The dose is simultaneously measured with Ionization Chambers (ICs) (0.056 cm^3 Extradin thimble type model A1SL Standard Imaging inc., Middleton, WI USA) provided by the TomoTherapy vendor (shown in Figure 2.12(c)) at 3 different positions in the sagittal plane of the "cheese-phantom". The simultaneous measurement is possible by the use of an 8-Channel electrometer (Tomoelectrometer™, Standard Imaging inc., Middleton, WI USA). A film (10"x12" EDR2 Ready Pack, Kodak, Rochester, NY USA) is positioned in the coronal plane and processed after the irradiation to convert the optical density to dose with a calibration curve. Finally, measured dose values are input into the planning station in order to be compared with the calculated ones. Point dose differences, profile comparisons and 2-D gamma distributions are used for the evaluation of the plan.

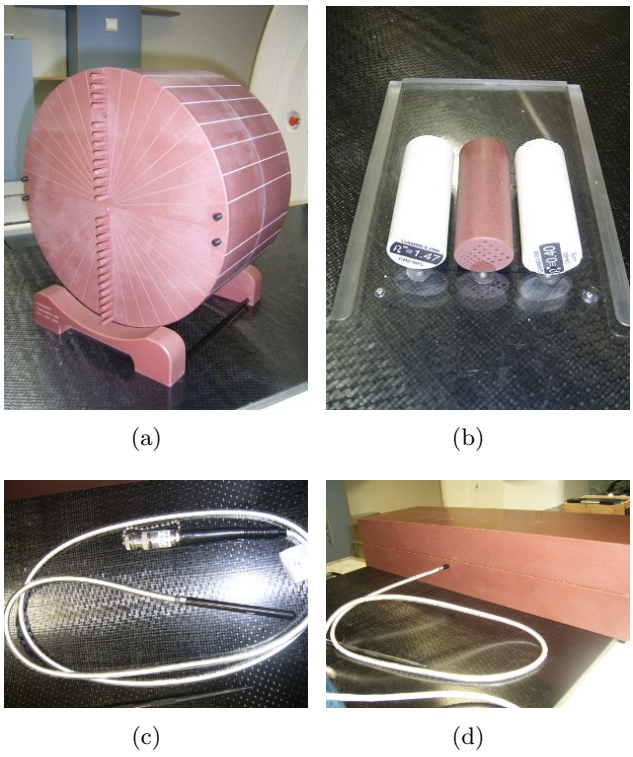

(a) (b)

(c) (d)

Figure 2.12: *Part of the equipment (offered by TomoTherapy inc.) used at the University Hospital of Heidelberg for the QA of the Helical TomoTherapy system. (a) "Cheese-phantom". (b) Different density "plugs" including a resolution testing plug. (c) Ionization chamber A1SL. (d) "Slab-phantom".*

Daily checks

Daily checks are consistent with the recommendations from Balog and Soisson (2008), verifying the MVCT image quality, red and green laser positions, visible and audible indicators, couch translation accuracy and integral dose output. However, energy variations were not verified on a daily basis, as suggested by Broggi et al. (2008). The reference

plan alluded in test D3, was performed for QA purposes using the CT scan images of the cheese-phantom as "patient". In this geometry, a simulated cylindrical target volume in the upper part of the phantom and an organ at risk in the central part of it (also cylindrical) were delineated and then, a treatment plan was calculated.

Weekly checks

Test W2 is performed using the slab-phantom (Figure 2.12(d)) and two ICs measuring simultaneously at depths of 10 and 20 cm. W4 is performed using the set-up shown in Figure 2.12(b). The resolution is tested visually by identifying the last "resolvable" row of the resolution plug. The fiducial marks in the acrylic base are used to check the spatial accuracy of the imaging system and the position of the virtual isocenter. The test W5, developed by Balog et al. (2006), lasts only 100 s and allows the testing of many of the unique features of the system. Analyzing the charge collected (every 100 ms) by two ICs positioned inside the cheese-phantom (at 5 mm from the center and 14 cm radially outwards in the most distal hole from the couch), parameters like the gantry period, couch offset, integral dose, energy and table velocity, can be tested. This test requires the use of the vendor supplied QA equipment.

Monthly checks

Many of the monthly tests recommended by Balog and Soisson (2008) such as image quality check, the D20/D10 test and the measurement of the couch speed among others are performed on a more regular basis (weekly) at the University Hospital of Heidelberg. Tests M1, M2 and M3 are performed using EDR2 films and the slab phantom for different MLC, gantry and couch configurations. These procedures and the evaluation software (TomoTherapy Film Analyzer) are provided with the system. Test M4 also uses the slab phantom and an EDR2 film. M5, M6 and M7 are performed using the same patient plan and the cheese-phantom. Test M8 is performed using an IC, which is positioned directly at the isocenter in a phantom that only provides the necessary build-up material. The IC remains static, measuring the collected charge every 100 ms, while the gantry constantly rotates around it with a period of 60 s for a time lapse of 30 min. The MLC leaves are open during the complete process.

Semestral checks

Semestral checks are basically the ones described by Balog and Soisson (2008) to be tested on an annual basis. These checks include most of the commissioning tests and should reproduce the respective values. The water tank measurements were not strictly performed in 6-month intervals, but every time the target was replaced.

Yearly checks

The correct functioning of all security systems and the vertical accuracy of the table were tested on a yearly basis.

As many of the dosimetric tests included in the QA program are proposed and evaluated by the system itself and/or require specific equipment supplied by the same company, the implementation of a supplemental QA procedure, is proposed. This procedure, based

on the dose calculation method presented in Section 2.3, would serve to test the overall performance of the system and the effect of individual parameter variations (e.g., output, gantry speed, and table velocity) within the treatment. Once the patient treatment sinograms are available, it can also be used as a patient specific delivery verification test.

Table 2.2: *Schedule of the QA program for the TomoTherapy unit at the University Hospital of Heidelberg (Kai Schubert, private communication).*

	Patient specific checks
P1	Patient DQA:
	Film, coronal 2-D dose distribution (Gamma index<1, 3%/3mm)
	IC measurements (3 simultaneous points)
	target volume(s) and organ(s) at risk (±3%)
	Daily checks
D1	Visible and audible indicators (working)
D2	MVCT air scan (no artifacts)
D3	Reference plan:
	MU constancy (±1%)
	Table position before and after the plan (±1mm)
	Laser position (±1mm)
	Weekly checks
W1	Lasers:
	Red (movable) relative laser position (±1mm)
	Green (static) absolute laser position (±1mm)
W2	Absolute dosimetry:
	Dose at 10 cm depth in a virtual-water phantom (±1%)
	Dose at 20 cm depth in a virtual-water phantom (±1%)
	D20/D10 (±1%)
W3	Reference plan:
	IC measurement, high dose (±2%)
	IC measurement, low dose (±2%)
	Film, coronal 2-D dose distribution (Gamma index<1, 2%/2mm)
	Film, longitudinal profile (optic agreement)
W4	MVCT image quality:
	Transverse distance between markers (±1mm)
	Longitudinal distance between markers (±1mm)
	Virtual isocenter (±1mm)
	Hounsfield Units, low, medium and high density
	Resolution (1 mm)
W5	Dynamic test:
	Energy (±1%)

Continued on next page...

Table 2.2 – **Continued from previous page**

	Gantry period (±0.2s)
	Table velocity, FWHM of lateral profile (±1mm)
	Table offset (±1mm)
	Integral dose (±2%)
	Monthly checks
M1	Virtual isocenter offset in x,y and z (±1mm)
M2	MLC center/gantry isocenter
M3	Central axis-Y axis misalignment
M4	Longitudinal field, uniformity and size (Gamma index<1, 1%/1mm)
M5	MVCT dose (<2 cGy)
M6	Patient plan:
	IC measurement, high dose (±3%)
	IC measurement, medium dose (±3%)
	IC measurement, low dose (±3%)
	Film, coronal 2-D dose distribution (Gamma index<1, 3%/3mm)
M7	Patient plan with interruption, compared with the non-interrupted:
	IC measurement, high dose (±2%)
	IC measurement, medium dose (±2%)
	IC measurement, low dose (±2%)
	Film, coronal 2-D dose distribution (Gamma index<1, 1%/1mm)
M8	Rotational test:
	Output constancy (±2%)
	Output angular dependence (±2%)
	Semestral checks
S1	Transverse profile at different gantry angles (Gamma index<1, 2%/2mm)
S2	Hounsfield Units
S3	Water tank static IC measurements (after target replacement):
	PDDs
	Longitudinal and transverse profiles at different depths
	Yearly checks
Y1	Security systems (working)
Y2	Table vertical position accuracy (±1mm)

2.4.4 Dose verification using the small-field model as a supplemental quality assurance test

The beam model presented in Section 2.3 has been validated to ensure that it can accurately reproduce dose distributions in water using small fields. Therefore, it has been implemented as the central engine of the calculation algorithm used for the TomoTherapy dose verification tool.

Using this verification tool, three-dimensional dose distributions were obtained in a homogeneous (water equivalent) virtual cylindrical phantom, coaxially aligned with the gantry rotation axis. A schematic representation of this phantom, indicating the main evaluation planes (where the results were obtained and visualized), is shown in Figure 2.13. The axis of the cylindrical phantom has a length of 20 cm and a radius is of 10 cm. The calculation voxels were defined to be of 1x1x1 mm^3.

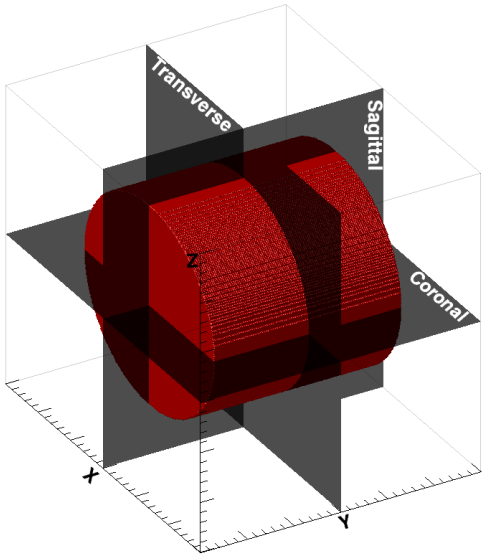

Figure 2.13: *Virtual cylindrical phantom and main evaluation planes.*

Static Mode

The input data required to implement the model into the dose calculation tool was collected using, in principle, the same methods as described in Section 2.3. Only a few modifications regarding the reference conditions were introduced. The reference field, in the TomoTherapy case, corresponded to a 40x5 cm^2 field defined at 85 cm from the source. The weights of the spectrum used for the determination of the poly-energetic PBK were obtained by fitting the calculated PDD to the one measured for this new reference condition. As mentioned before, the absence of a flattening filter makes the mean energy change at off-axis positions to be less than 5% (Jeraj et al., 2004). Therefore, no correction for lateral spectral changes was applied.

As the table sunk (∼1-2 mm) while it was moved from the virtual isocenter (where the slit-collimator device was positioned) to real isocenter (70 cm apart in the longitudinal direction), it was not possible to determine the exact position of the source with respect to the Central AXis (CAX) (i.e., the slit was not perfectly aligned with it). Therefore, it

could only be assumed that the source was centered. The validity of this assumption can be evaluated by the comparison between measured and calculated penumbras.

Planar dose distributions were obtained according to 2.3.3, although some small differences from the method described previously had to be considered. The first one is the fact that, in the case of TomoTherapy, the "envelope profile" obtained does not correct for the horn-effect produced by the flattening filter. On the contrary, it accounts for the characteristic cone shaped distribution of the fluence (see Figure 2.11(a)), due to the absence of a flattening filter. The second one is that, in this case, the leakage contribution to the final dose calculation has been included as an additive component to the 2-D dose distributions obtained. The leakage was taken into account by a cross-profile measured in the X direction with all the leaves of the MLC closed and the Y-jaws set to their maximum opening (relative to the maximum dose when all leaves are open and the jaws project a 5 cm field at the isocenter plane). To obtain the 2-D distribution needed for the planar dose calculations, the profile was replicated and weighted by the envelope distribution in the perpendicular direction. The specific shape of the collimators and other (second order) effects related with the MLC hardware have not been explicitly modeled. These include: the tongue&groove effects and the fact that the leaves are not perfectly back-focused to the source, thus, the fluence at a certain position under a leaf is influenced by the state (open/closed) of neighboring leaves.

Dynamic Mode

Three dynamic modes of the system can be identified. These are:

- *Topographic:* the couch moves longitudinally while the gantry angle is fixed during the complete beam-on time.
- *Rotational:* the couch is fixed while the gantry continuously rotates around it until the procedure is finished.
- *Helical:* both couch and gantry move simultaneously throughout the treatment.

All patients are treated in helical mode. The first two modes are used only for QA purposes. The verification tool presented here can calculate dose distributions for any of these modes including, of course, the static mode.

The final dose distributions were obtained as follows:

1. *Beamlet calculation:* The dose delivered to the virtual cylindrical phantom (centered in the longitudinal direction) was calculated using the static mode of the system (with the CAX perpendicular to the couch plane), for each one of the leaves opened individually and for each one of the three possible openings of the Y-jaws (the field width in the Y direction is fixed during the treatment to either 1, 2.5 or 5 cm projected to the isocenter plane). Each "beamlet" distribution was stored for later use. After this step, the model is no longer needed.
2. *Input of basic treatment parameters:* The algorithm requires, as a first step for the determination of the integral dose (after the beamlet distributions have been determined), the input of the main treatment parameters. These include: (i) the opening of the Y-jaws (1, 2.5 or 5 cm), (ii) the number of projections used in a complete rotation of the gantry (the default is 51, as this is the value used by the

TPS to plan patient treatments), (iii) the gantry period (between 10 and 60 s) and (iv) the displacement of the couch after a 360° gantry rotation. If the number of projections per gantry rotation is fixed to 51 and the jaw setting is given, the only extra treatment parameter needed is the pitch (see Equation 2.11). Typical pitch values used in patient treatments range from 0.25 to 0.5 (Kissick et al., 2005).

3. *Initial conditions:* Before starting the calculation process, the initial longitudinal position of the center of the phantom and the gantry angle need to be set.

4. *Sinogram "filtering":* The sinogram, described in Section 2.4.2, contains all the information related to the modulation of the beam (performed in the transverse direction, perpendicular to the patient movement). The optimized modulation patterns for each patient treatment obtained by the TPS, are subject to some modifications before the data is transferred to the delivery system. Even though currently the patient specific sinograms cannot be directly extracted from the TPS and implemented into the calculation tool. Here, the dynamic effects that introduce modifications into the calculated sinograms (and the corrections that account for them) to be implemented as part of a patient specific QA procedure, are pointed out. The first sinogram filtering, done projection by projection, is related to the latency of the MLC leaves. It takes approximately 10 ms to open/close each leaf. The opening time of each leaf in a projection is obtained by multiplying the opening fraction by the gantry period, and dividing it by the number of projections per rotation. If any of the leaves is programmed to be open in a specific projection for a period of time equal or less than 20 ms, the leaf is set to be closed during the complete projection time. Also depending on the projection time and latency, the opening fractions of the leaves are recalculated by a linear transform that accounts for the effective opening with respect to the programmed time. A transform function for a specific projection time is obtained by fitting straight lines to measured values of the effective opening time with respect to the programmed one (this behavior is similar within leaves). This process is done for different projection times, between 200 ms (although the minimum projection time allowed for patient treatments is of 294 ms, corresponding to 51 projections per gantry rotation with a rotation period of 15 s) and 1000 ms (where the linear relation between programmed and effective opening time has a slope of $\sim$1). If the projection time does not coincide with the ones used to obtain the transforms, the transform is obtained by simple linear interpolation (if the projection time is larger than 1000 ms, then the transform obtained for 1000 ms is used). This process has been described by Balog et al. (2003).

5. *Projection dose:* The dose deposited in the phantom by the delivery of a single projection (D_p) is calculated in the following way: The pre-calculated beamlets ($b_{Y,ln}$) corresponding to each leaf (ln) and to the nominal opening of the Y-jaws (Y) are weighted by their opening time ($O_{t,p,ln}$) and summed. Then, the distribution is rotated (interpolation is needed) and shifted; according to the gantry angle (θ_p) and the longitudinal position of the phantom (y_p), both corresponding to the projection (p). i.e.,

$$D_p(x,y,z) = \sum_{ln=0}^{64} O_{t,p,ln} \cdot b_{Y,ln}(x\ cos(\theta_p) + z\ sin(\theta_p), y - y_p, -x\ sin(\theta_p) + z\ cos(\theta_p)), \tag{2.12}$$

where the coordinates (x, y, z) refer to the coordinate system shown in Figure 2.9(a). The opening time $O_{t,p,ln}$, angle θ_p and phantom position y_p are determined as

$$O_{t,p,ln} = O_{f,p,ln} \cdot \frac{T}{p_r}, \tag{2.13}$$

$$\theta_p = \theta_i + \left(\frac{p}{p_r} \cdot 360^\circ \right) \; mod \; 360^\circ \tag{2.14}$$

and

$$y_p = y_i + \frac{p}{p_r} \cdot y_r, \tag{2.15}$$

respectively, where $x \; mod \; y$ returns the least common residue of the division x/y[1], $O_{f,p,ln}$ is the fraction of the projection time that the leaf ln remains open for the projection p, T is the gantry period, p_r is the number of projections per gantry rotation, θ_i is the initial gantry angle, y_i is the initial longitudinal position of the center of the phantom and y_r is the couch displacement per gantry rotation. The rotation angle is defined clockwise starting from the Z direction.

6. *Integral dose:* The final dose distribution (D_f) is obtained by superposing the distributions calculated for each projection of the treatment as

$$D_f(x, y, z) = \sum_{p=0}^{p_f} D_p(x, y, z), \tag{2.16}$$

where p_f is the total number of projections of the (filtered) sinogram.

2.4.5 Test of the tool

The dose verification tool was evaluated in the static and dynamic modes by comparing measured and calculated values.

Static tests

Using the static mode of the system, measurements were carried out by a diode detector in a water tank at 15 mm depth with a SSD of 85 cm. The tests consisted in the comparison of measured and calculated OFs and dose profiles for different collimator configurations.

Output factors were determined for a fixed Y-jaws opening (5 cm at the isocenter) varying the field size in the perpendicular direction (MLC) from 1.25 to 40 cm defined at the surface. Only symmetric openings were considered. The performance of the tool regarding the modeling of dose distributions in the plane perpendicular to the CAX (parallel to the couch plane) was tested in the X and Y directions for different rectangular fields and also for a more complex MLC pattern (where every other pair of leaves was set to be open).

Figure 2.14 shows the sinogram used for the measurement of OFs and planar dose profiles for different field openings in the X direction. It has, initially, 30 projections where all the leaves remain close (to provide sufficient time for the stabilization of the

[1]Weisstein, Eric W. "Modulus". From MathWorld–A Wolfram Web Resource. http://mathworld.wolfram.com/Modulus.html.

beam output before starting the measurements). Then, every 10 projections, an additional amount of leaves were open (symmetrically) until all of them were open (during the time corresponding to 10 projections, starting from the projection number 160). A different projection time was used for each set of measurements, as the scanning of the profiles required a longer time than the measurement of OFs.

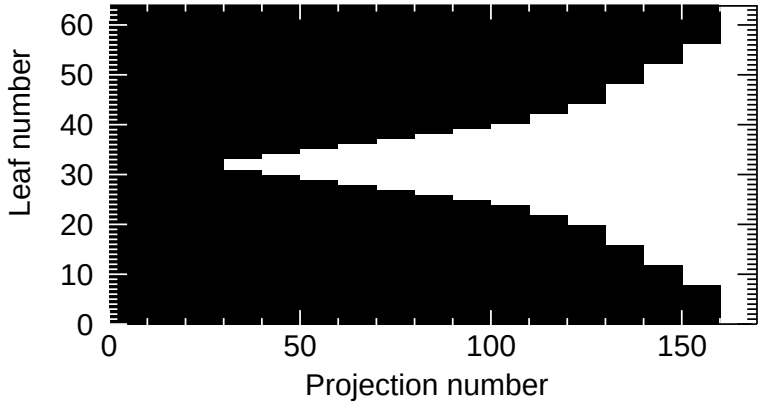

Figure 2.14: *Sinogram used to measure the OFs and the rectangular dose profiles.*

Dynamic tests

The three dynamic modes (topographic, rotational and helical) of the system were tested for a simple MLC configuration, in which the four central leaves (projecting a field width of 2.5 cm at the isocenter) were set to be open during the complete irradiation time. The Y-jaws opening was fixed to 2.5 cm (projected to the isocenter). The measurements were performed using the cheese-phantom (see Figure 2.12(a)) and a film positioned in the coronal plane that divided the cheese-phantom in two equal halves. Transverse and longitudinal profiles were compared. The treatment parameters (described in Section 2.4.4) used for each treatment mode are displayed in Table 2.3.

Table 2.3: *Parameters used for the evaluation of the dose verification tool in the different dynamic modes.* $^{(*)}$ *Even though the gantry remains fixed in the topographic procedure, it is necessary to input the values for every parameter in order to assign the absolute projection time and couch velocity.*

Parameter	Unit	Topographic$^{(*)}$	Rotational	Helical
θ_i	°	0	0	0
y_i	cm	-5	0	-5
T	s	10	10	10
p_r	-	10	10	10
y_r	cm	1	1	1
p_f	-	100	20	100

2.4.6 Parameter variations

It has been suggested, as part of a QA program of the TomoTherapy system, to check whether the output variation remains below ±2% of the long time average (Fenwick et al., 2004). However, it was found that this was not always accomplished. Motivated by this fact and making use of the validated evaluation tool, it was decided to investigate the effects of single parameter variations in the integral dose for a simple helical case.

Table 2.4: *Systematic and random temporal variations introduced in the parameters of the treatment.*

Parameter	Systematic	Random
Output (O)	$O^n(t) = O$	$\pm 0.02 \cdot O$
Couch velocity (V_c)	$V_c^n(t) = \frac{1}{8} \cdot V_c \cdot \frac{t}{100} + V_c \cdot \frac{7}{8}$	$\pm 0.04 \cdot V_c$
Gantry speed (ω_g)	$\omega_g^n(t) = \frac{4}{100} \cdot \omega_g \cdot sin\left(t \cdot \frac{2\pi}{50}\right) + \omega_g$	$\pm 0.04 \cdot \omega_g$

The dose delivered to the virtual phantom was calculated in a simple reference case using the helical mode. The treatment parameters were: 2.5 cm jaw opening (at the isocenter plane), 50 s gantry period, 50 projections per rotation, 5 cm displacement of the couch per gantry rotation, 0° initial gantry angle, 10 cm displacement of the phantom's position prior to the treatment (with respect to the isocenter, in the direction opposing the couch movement) and a total number of projections of 200. This was used as the reference case, in which the output, gantry speed and couch velocity, were assumed to be constant during the treatment. Then, the calculation was repeated, but this time random and systematic temporal variations of the parameters were introduced. Finally, profiles in the longitudinal and transverse directions of the reference and perturbed distributions were compared. Random variations were added to all the studied parameters. Additionally, systematic sinusoidal and linear variations of the gantry speed and couch velocity, respectively, were also introduced. The individual variations are displayed in Table 2.4, where t indicates the time (in seconds) and ^{n} refers to the new value of the parameter (depending on t).

"We can have facts without thinking but we cannot have thinking without facts."

John Dewey (1859-1952)

3 Results

The results of this work are presented in this chapter. They are divided into two parts: First, the establishment and validation of the dose calculation engine and second, the use of this model in a dose verification tool for TomoTherapy. The concepts and specific methods and materials employed for the determination of these results have been previously described in Chapter 2. Their discussion and interpretation will be presented separately in Chapter 4.

3.1 Beam model

The developed dose calculation algorithm aims at modeling accurately the dose deposition in homogeneous media for narrow beams. For this purpose, a kernel-based method (PBK), which allows handling the non-CPE conditions within narrow fields by explicitly modeling the energy transport of the secondary particles, was used. The other effect that has been taken into account in the modeling of small fields is the partial blocking of the source. For this, the effect of an experimentally determined extended source was included into the modeling of the fluence distribution. This extended source distribution not only includes the focal spot, but also the head scatter contributions.

In this section, the results of each step in the determination of the extended source are presented, followed by the determination of the poly-energetic PBK based on pre-calculated mono-energetic DDKs. Then, the results of the validation tests for the model are given. The tests have included the comparison between measured and calculated planar dose profiles and OFs for quadratic and circular fields of different sizes. Most of the results presented in the first part of this chapter can also be found in Caprile and Hartmann (2009).

3.1.1 Extended source

As described in Section 2.3.1, the extended source is defined as the projection of all primary photons and head scatter contributions into a common plane. This two-dimensional

distribution is composed of an "inner" and an "outer" part. The latter, represents the section of the distribution where the intensity was less than 0.1% of the maximum and was determined by a CF analysis.

Inner part.

A slit-collimator (shown in Figure 2.2(a)) was used to measure strip-integrals of the source at different angles. The measured profiles are shown in Figure 3.1. It is noticeable that, after a very pronounced slope close to the central axis, there is a flux stabilization in the measurement. This fact hints that a background signal was being detected. It can also be noticed that there is a slight difference in the maximum value. This is due to the fact that the position of the maximum detected at different angular positions did not coincide exactly with the zero position, but varied within ±1 mm as the system was rotated. It was considered that the geometrical uncertainty in the positioning of the slit-collimator device was also around 1 mm, as the alignment with the laser and the rotation of the system was done manually. Therefore, it was assumed that the source was centered and the measured strip-integrals were shifted to the zero position.

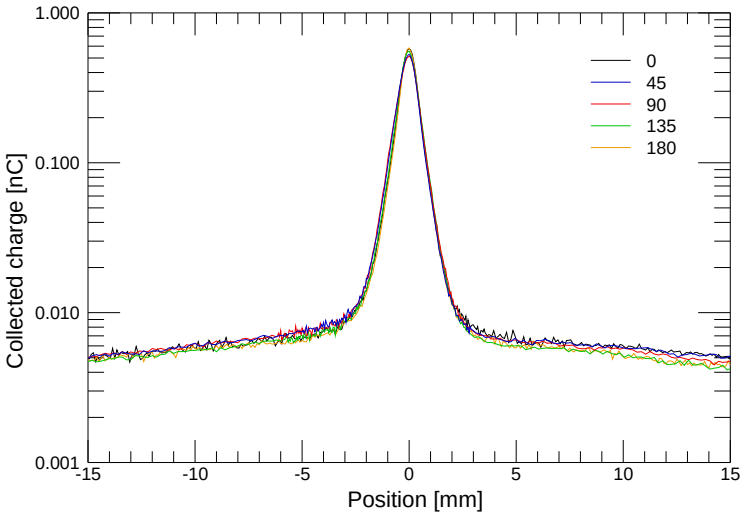

Figure 3.1: *Strip-integrals of the source measured at 0°, 45°, 90°, 135° and 180°.*

A mean Full Width at Half Maximum (FWHM) of the strip-integrals of 0.91±0.06 mm ($\bar{x} \pm \sigma$) was obtained. As the standard deviation of the FWHM was below the resolution of the measurement (0.1 mm), radial symmetry was assumed as a good approximation for the reconstruction process. By the assumption of radial symmetry, the function to be minimized in the iterative reconstruction (Equation 2.4) gets simplified to

$$\chi^2(X) = \sum_i \frac{\left(\sum_r F_r^i X_r - p_i\right)^2}{\sigma_i^2}, \tag{3.1}$$

where p_i is the radially symmetric projection value (average of the measured projections at different angles) at the i^{th} radial position, with an associated uncertainty σ_i. X_r is the intensity of the focal spot at the radial position r and F_r^i is the fraction of X_r projected into p_i. The determination of F_r^i and the minimization of the parameters is thus fairly simple and straight forward. This is due to the reduction of the number of free parameters

from $(2n)^2$ to n, where n is the number of radial positions in which the intensity of the source is reconstructed. The parameters in the χ^2 minimization were constrained to be positive.

The reconstructed radial distribution of the source can be seen in Figure 3.2. It was found to have a FWHM of 0.50±0.08 mm. The division between the inner and outer part of the source, indicated by the dashed line, was selected arbitrarily to be at 0.1% of the maximum intensity (corresponding to a radial position of approximately 3 mm from the center). It was assumed that, down to this point, the reconstructed signal was not affected by the background.

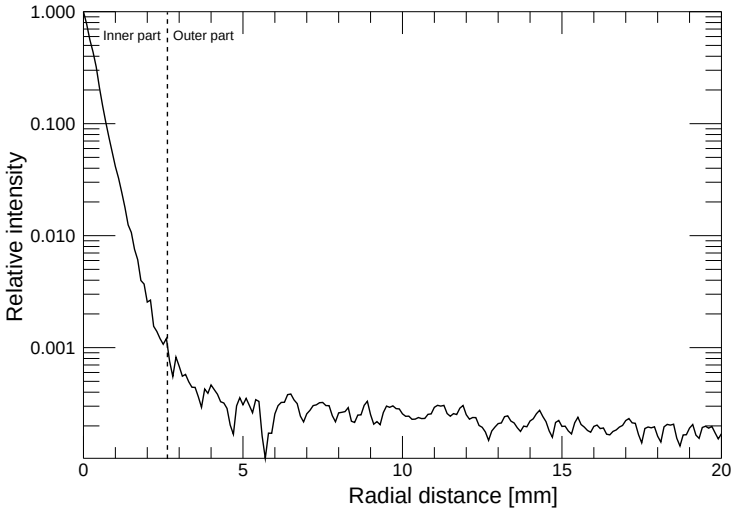

Figure 3.2: *Reconstructed radial distribution of the source. The dashed line indicates the division between the inner (left from the dashed line) and outer (right from the dashed line) parts of the source.*

Outer part.

The outer part of the extended source accounted for the head scatter contributions. CFs were calculated according to Equation 2.5, assuming radial symmetry of the source. The distances l_{cx} and l_{cy}, used for the determination of the integration limits, were obtained by measuring the distance from the edge of the collimators to the isocenter plane, considering a distance of 100 cm from the source to the isocenter. The values obtained were l_{cx}=28.1 cm and l_{cy}=19.5 cm. Using these values, it was found that the inner part of the source ($r \lesssim 3$ mm) was completely visible for nominal field sizes larger than 1.7 cm in the X-direction and 2.3 cm in the Y-direction.

Figure 3.3 shows the result of the fitting process required for the determination of the relative intensity values of the source. The CFs calculated using the inner part of the source (dashed line), give evidence that the focal spot by itself does not account for the measured increase of the CFs with field size (circles). The continuous line represents the fitted CFs. The fitted parameters give the intensity values for the outer part of the source that is shown in Figure 3.4 (continuous line, to the right of the vertical dotted line). It was found that the radial distribution of the outer part of the source behaves approximately like c/r^2 (where c is a normalization constant and r is the radial position).

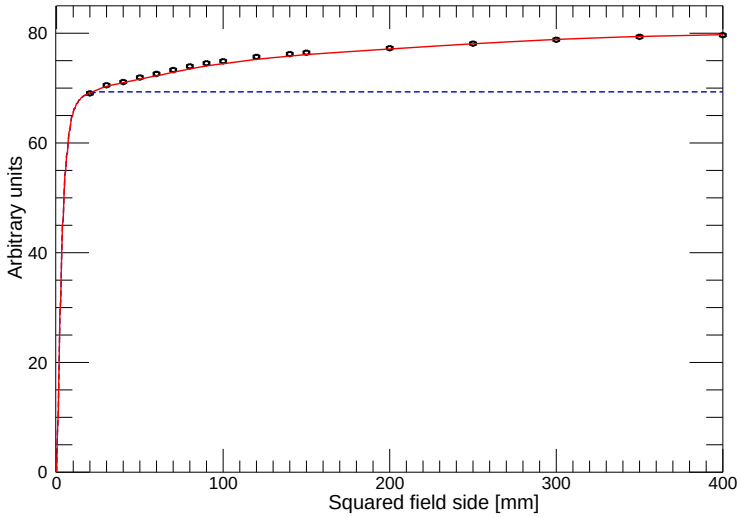

Figure 3.3: *Measured (open circles), calculated (dashed line) and fitted (continuous line) collimator factors. Calculated values were obtained using the inner part of the source.*

The parameters that yield the values for the inner part, were fixed (to the ones obtained in the reconstruction process).

The final extended source distribution.

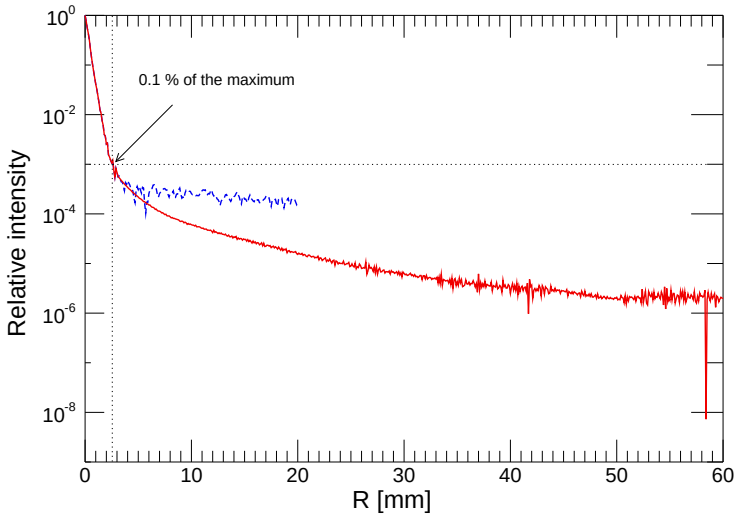

Figure 3.4: *Full radial distribution of the source. The dashed line represents the reconstructed source and the continuous line represents the extended source, obtained as a result of the inner part plus the result of the collimator factor fitting procedure.*

The full distribution of the (extended) source is shown as a continuous line in Figure 3.4. It represents the combination of the reconstructed focal spot (to the left of the vertical dotted line) and the fitted outer part (to the right of the vertical dotted line). It can be seen that the difference between the distribution reconstructed by the slit-method

(dashed line) and the extended source becomes significant for radial positions $\gtrsim$5 mm. The disagreement confirms the hypothesis that the strip-integrals were "contaminated" by the detection of a (very low, <1% of the maximum) background signal. The intensity of the source varies by almost 6 orders of magnitude within its radial range. Although the contributions from the outer part of the source may seem negligible when compared to the ones from the inner part, they are necessary to account for the correct dependency of the CFs with field size (Figure 3.3).

3.1.2 Pencil beam kernel

The PBK distribution obtained (see Figure 3.6(d)) was used to model the energy transport of the secondary electrons. A detailed description of the determination of this distribution is given in Section 2.3.2.

The mono-energetic DDK distributions required for the calculation were obtained directly from Monte Carlo simulations (the simulation parameters are given in Table 2.1). The geometry in which the results were obtained was not cartesian but spherical (see Figure 2.4). The dose deposited in the homogeneous medium (water) was stored in different conical sectors, defined by the volume enclosed by two consecutive radii (24 in total, ranging from 0.1 mm to 60 cm) and two consecutive azimuthal angles (48 in total). The dose values were transformed into cylindrical coordinates (see Figure 3.6(d)), using logarithmic interpolation to simplify the calculations.

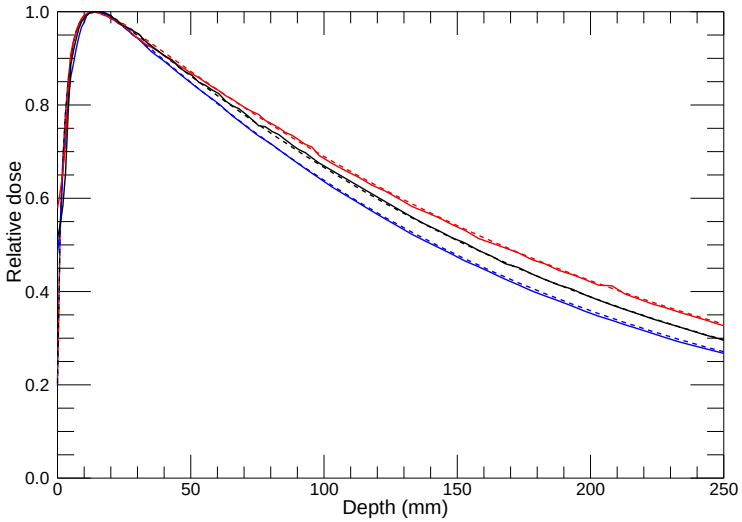

Figure 3.5: *Measured (continuous lines) and calculated (dashed lines) PDD curves (with a SSD=100 cm) for 5x5 (blue), 10x10 (black) and 20x20 cm^2 (red) normalized to the maximum value.*

A preliminary calculation of the PBK was done using the pre-calculated DDK and the energy weights of Mohan's spectrum for a 6 MV photon beam. As the calculated dose did not exactly reproduce the measured PDD for the reference field, new weights were obtained according to Equation 2.7. Figure 3.6 shows relative DDK and PBK distributions for mono-energetic photons with an energy of 1 MV and for the new spectrum weights obtained. It can be noted that the relative distributions obtained for 1 MV are hard to distinguish from the poly-energetic ones calculated using the spectrum of the beam.

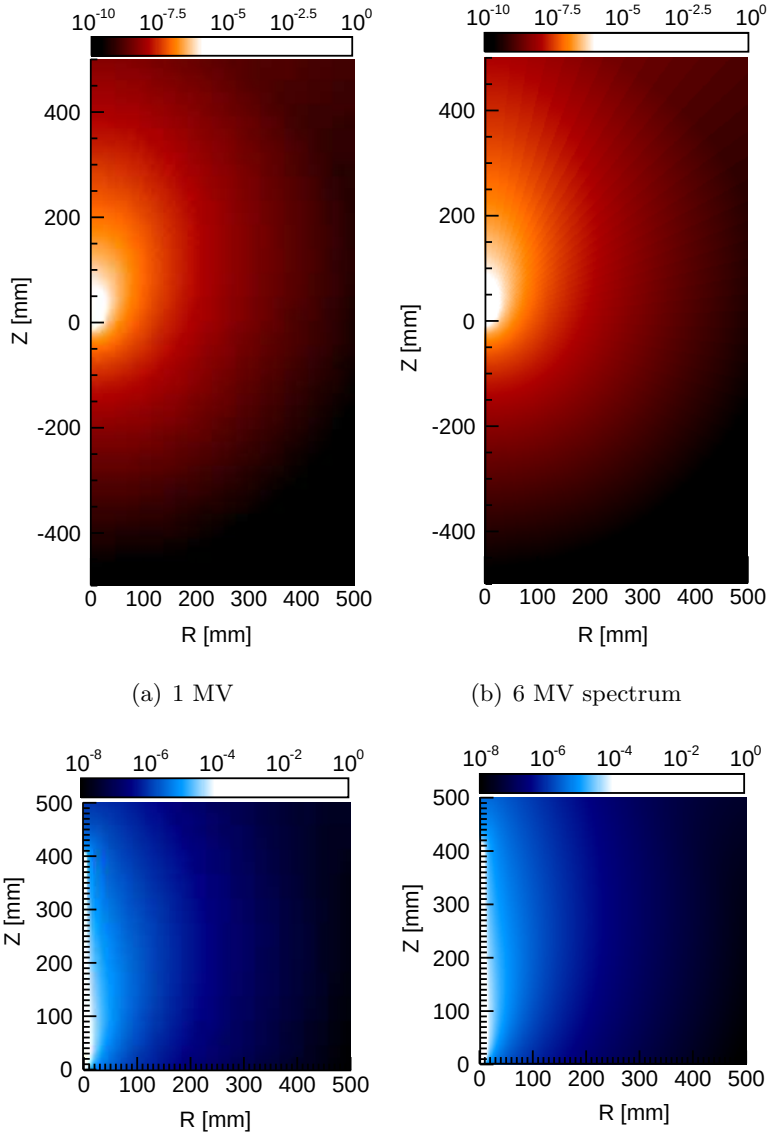

(a) 1 MV

(b) 6 MV spectrum

(c) 1 MV

(d) 6 MV spectrum

Figure 3.6: *Normalized point (top) and pencil beam (bottom) distributions for mono-energetic (left) and poly-energetic (right) photons. The poly-energetic distributions are calculated using the spectrum obtained for the 6 MV beam of the linac.*

Figure 3.5 shows the result of the PDD fitted to the measured curve for a 10x10 cm^2 (reference) field. It also presents the comparison between measured and calculated PDDs for 5x5 and 20x20 cm^2 fields using the new spectrum. Good agreement between measured and calculated values is observed for all the cases without considering the build-up region. The reference field was big enough to prevent the spatial extension of the source from influencing the depth dose in the central axis. Therefore, a point source was assumed for the depth dose calculations according to Equation 2.7.

3.1.3 Validation tests

The model was validated for a 6 MV photon beam using a variety of field sizes, including circular and quadratic fields. Since the stereotactic collimators (formed by tungsten cylinders of 10 cm in height with different internal radii) were positioned at a SCD of 59 cm (distance from the source to the distal edge of the collimator), the circular fields projected at the measurement plane had a diameter $d_m = 1.72 \cdot d_c$ (where d_c is the collimator diameter). Conversely, the field of view of the detector projected to the source plane had a diameter $d_s = 1.93 \cdot d_c$. Therefore, the inner part of the source ($r \lesssim 3$ mm) was uncovered from the detector's point of view for collimators with $d_c \gtrsim 3$ mm, as the detector was positioned at 1015 mm from the source.

To test the performance of the model in a homogeneous medium (as the aim was to use it for dose delivery verification in a homogeneous phantom), calculated OFs and dose profiles (at 15 mm depth with a SSD of 100 cm) were compared with measured values in the same conditions. These measurements were obtained using a diode in a water tank.

Output factors

Two methods to determine the OFs for the circular fields have been used: (i) direct diode measurements in the central axis and (ii) indirect determination by measurement of the relative 2-D distribution and use of a parallel plate chamber (see Section 2.3.4). Both results are shown in Figure 3.7(a) as circles and triangles, respectively. It can be seen that both methods agree well with each other, although some small (non-systematic) differences can be found. The continuous line represents the calculated OFs for the same conditions using the extended source in a calculation grid of 0.1x0.1 mm^2. They show a remarkable agreement with the diode measurements. The dashed line shows the effect of considering a point-like source in the determination of the dose. This calculation indicates the strong effect of the integration of the PBK within the field opening for the small fields, shaping the curve with the characteristic shoulder. It is also evidence of the importance of considering the spatial extension of the source to accurately model the OFs for small fields. This is particularly evident for the collimators with smaller apertures (d_c =1, 2 and 3 mm), which partially block the inner part of the source. For these cases, the difference in output between the point-source calculations and the measured values reaches 22.4% (for the smallest collimator aperture) with respect to the normalization value (corresponding to the collimator with d_c=20 mm). The difference in the same case, but considering the extension of the source, is 1.4%. The calculated OFs agreed with the (diode) measured values within ±2% of the normalization value (except for the value corresponding to the collimator with d_c=2 mm, for which the difference was of 2.07%).

Figure 3.7(b) shows the measured and calculated OFs for the quadratic fields. Considering the extension of the fields (maximum field size of 40x40 cm^2) and the fact that the uncertainty in the field size compared with the nominal value is on the order of 1 mm, a coarser calculation grid (of 1x1 mm^2) was used in order to reduce the calculation time. The same trend already shown for the circular fields is observed here, demonstrating that the approximation of the source as a point (considering the phantom scatter by the integration of the PBK contribution within the field) is not sufficient to model the increase of dose deposited on the central axis with increasing field size (see dashed line). The OFs calculated using the extended source appear to be in good agreement with the values measured with the diode. The discrepancies observed for the first three measure-

ments (corresponding to quadratic field sides of 5, 10 and 20 mm in length) should be judged considering that the corresponding (visible) section of the extended source has a very steep slope, and thus, a small deviation in the field size (the uncertainties associated with the field size are of the order of 1 mm) leads to an important variation in output.

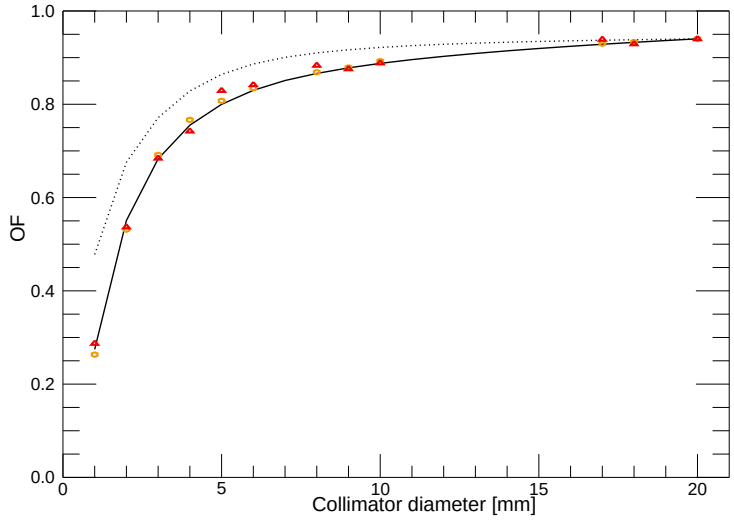

(a)

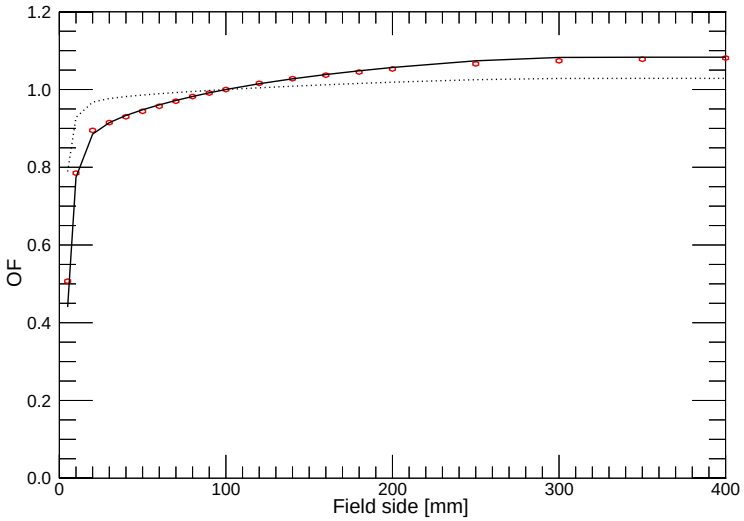

(b)

Figure 3.7: *Output factors: measured with a diode (open circles), measured with a combination of diode and parallel plate chamber (open triangles), calculated using the extended source (continuous lines) and using a point source (dashed lines). (a) Circular fields. (b) Quadratic fields.*

In general, the combination of PBK and extended source showed to be appropriate to model OFs from very small field sizes (the smallest field size evaluated corresponded to a circular field with $d_m = 1.7$ mm at the measurement plane) to the biggest available (40x40 cm^2 at the isocenter).

Dose profiles

The final test of the model consisted in the evaluation of its performance modeling lateral dose profiles (Figure 3.8), with particular interest in the penumbra (i.e., the region between the 90% and 10% dose points on the beam profile) of the small circular fields.

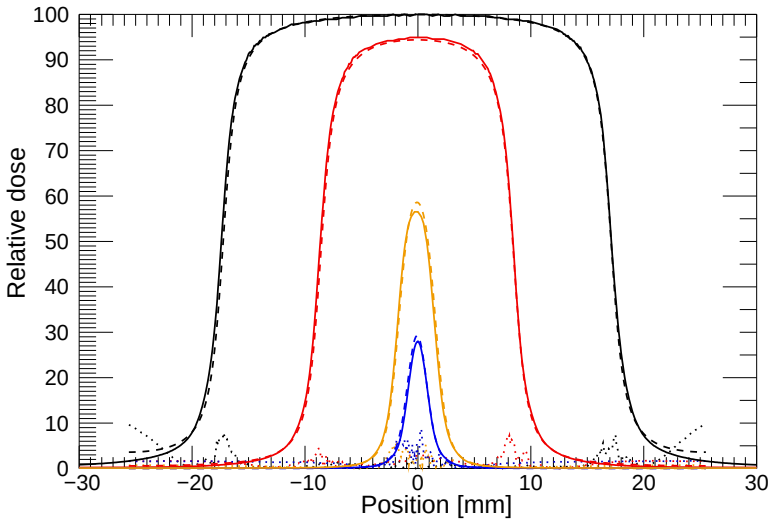

(a)

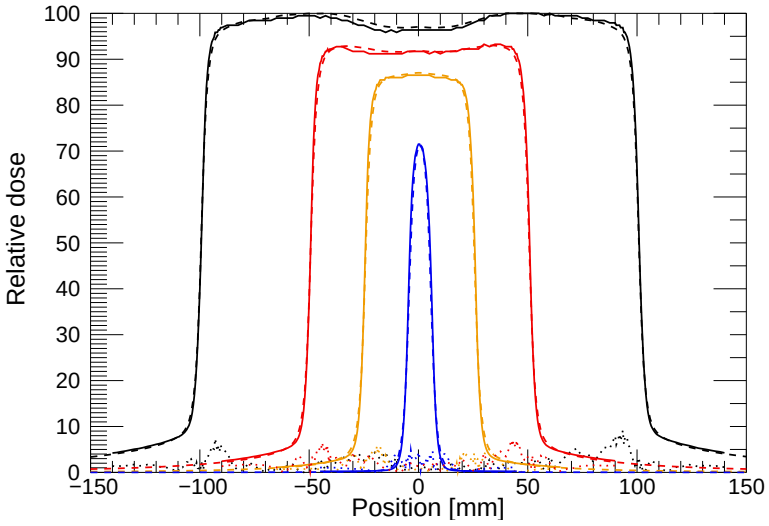

(b)

Figure 3.8: *Relative dose profiles measured (continuous lines) and calculated (dashed lines) for different field sizes. The dotted lines represent* $10 * \gamma$ *(gamma index value,* $\gamma < 1$ *: pass,* $\gamma > 1$ *: fail) for each profile. (a) Circular fields. (b) Quadratic fields.*

Figure 3.8(a) shows the comparison between measured and calculated dose profiles for the fields generated by the cylindrical collimators. The dotted lines represent the gamma index value (amplified by 10 for better visualization) with individual acceptance criteria of 2% dose difference and 0.5 mm DTA. This evaluation indicates that the calculations have passed the test in all the cases shown in the figure (corresponding to collimators with

d_c =1, 2, 10 and 20 mm). The good agreement indicates that the criteria could have been further tightened. The only regions presenting minor discrepancies (slight overestimation of the dose with respect to the measured values) corresponded to the central part of the profile for the collimator with $d_c = 2$ mm, and to the tails of the profile measured for the collimator with $d_c = 20$ mm.

Although the capacity of the pencil beam method to accurately model dose distributions for homogeneous media under conditions of CPE has already been widely studied and confirmed (Mohan et al., 1986; Bourland and Chaney, 1992; Ahnesjö et al., 1992; Storchi and Woudstra, 1996; Bortfeld, 2006), the modeled and measured lateral profiles for quadratic fields covering the complete range of possible field sizes were compared in order to have a complete validation of the model. Figure 3.8(b) shows the result of this comparison for (quadratic) field sides of s =1, 5, 10 and 20 cm length measured in the Y-direction.

For the quadratic fields the gamma index test (dotted lines) has been used again with the same dose difference criterion as for the evaluation of the circular fields (2%), but the DTA criterion has been changed to a value of 2 mm (considering that the calculation grid used for these calculations was of 1x1 mm^2 and that the uncertainty in the field size was higher than for the circular fields). The calculations presented here lie within these acceptance criteria in every case, the agreement is particularly good in the penumbra region. Small differences can be seen for the fields with s =10 and 20 cm on the left side of the central axis, in the region close to the "horns" of the profile. There, the calculated distributions slightly overestimated the measured dose at the corresponding off-axis position. It can be noted that the measured profiles for these field sizes are not perfectly symmetric with respect to the central axis of the beam. As the measured fields presented a systematic asymmetry with respect to the CAX of approximately 1 mm, the calculations were shifted for better comparison. A justification and analysis of this shift is given in Section 4.1.4.

3.2 TomoTherapy dose verification tool

In this section the results related to the integration of the model into a dose verification tool applicable to TomoTherapy delivered dose distributions and to the performance of the tool itself are presented. First, the input distributions necessary to apply the model to this system are presented. Then, the results of the evaluation of the model in its static and dynamic modes are shown. Finally, the comparison between a reference helical treatment calculation and the result of the same treatment, modified by temporal variations of the couch and gantry positions and of the beam output, is presented.

3.2.1 Model components

The components needed to implement the developed dose calculation model (described in Section 2.3) into a TomoTherapy dose calculation tool are the following: the determination of the extended source and the poly-energetic PBK, and the obtainment of the profiles used to correct the calculated planar dose distributions for the lateral fluence variation (envelope profile) and for the leakage contributions (see Section 2.4.4).

Source distribution

The extended source distribution of the TomoTherapy treatment beam (6 MV) was determined using the same combination of methods as in the validation of the model (slit-method and CF fitting, see Section 2.3.1).

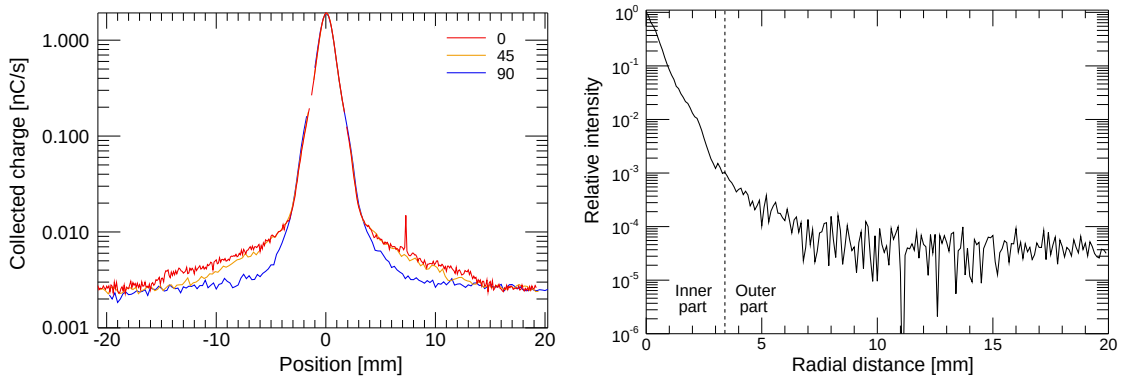

(a) (b)

Figure 3.9: *Slit-method TomoTherapy source reconstruction. (a) Strip-integral of the source measured at 0°, 45° and 90°. (b) Reconstructed distribution.*

Figure 3.9(a) shows the unnormalized strip-integrals of the source measured at different angular positions, with the detector positioned at a distance of approximately 65 cm from the source. The jaws and MLC openings were set to provide a nominal field size of 10x5 cm^2 at the isocenter plane. The 0° measurement corresponds to a scan of the source in the transverse direction (X axis). It can be seen that the shape of the measured distributions, with a FWHM of 1.37±0.02 mm ($\bar{x}\pm\sigma$), are virtually indistinguishable from the maximum value down to ∼1% of the maximum intensity (corresponding to a off-axis distance of ∼3 mm). Therefore, radial symmetry of the focal spot was assumed for the reconstruction. The radial distribution of the reconstructed source is shown in Figure 3.9(b). It has a FWHM of 0.72±0.05 mm. The dashed line shows the division between the inner and outer parts of the source (at 0.1% of the maximum intensity), this point corresponds to a radial distance of approximately 3.4 mm.

As the nature of the discrepancies in the strip-integrals, corresponding to intensity values lower tan 1% of the maximum, was not certain (most probably due to an undetermined amount of scatter radiation coming not directly from the source), it was only possible to assume radial symmetry also for the outer part. The outer part was obtained following the procedure described in Section 2.3.1 and according to this, it was found that the inner part of the source was completely visible from the isocenter point for field openings greater than 1.67 cm in the X direction and 2.80 cm in the Y direction. Figure 3.10(b) shows the result of the least-squares fitting process, for which the reconstructed distribution (and a c/r^2 distribution for the missing values) was used as a first guess. The fitted parameters produced a very good agreement between the measured (interpolated) and modeled CFs. However, it can be seen in Figure 3.10(a) that the fitted parameters are subject to some artifacts of the fitting process (related to interpolation issues and the non-negativity constraint), which are accentuated due to the fact that, after the first three evaluated fields, the increase of CF with increasing field size is almost negligible.

Figure 3.10(a) also reveals that the first component of the outer part (between the radial positions of ∼3 and ∼15 mm) can be modeled by the reconstructed source. This indicates that the measured strip-integrals were not as "contaminated" by a background signal as in the linac case (see Figure 3.4).

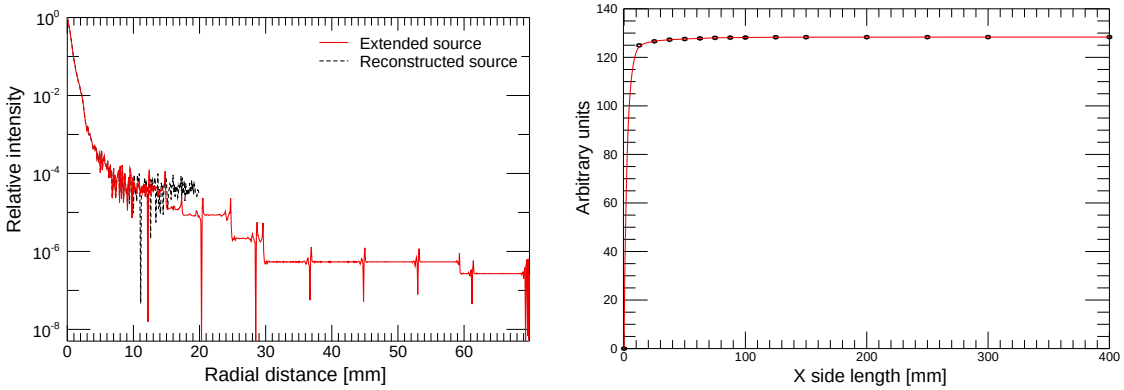

(a) (b)

Figure 3.10: *(a) TomoTherapy radial distribution of the extended source, composed of the inner reconstructed part and the outer fitted part. The dashed line represents the reconstructed distribution and the continuous line is the extended source. (b) Measured (circles) and fitted (continuous line) CFs. The fitted parameters give the radial intensity values of the extended source.*

Pencil beam kernel

The poly-energetic PBK distribution used for TomoTherapy planar dose calculations was obtained using the same pre-calculated DDK (mono-energetic) distributions. This time the weights of the spectrum were obtained according to Equation 2.7, by fitting the calculated PDD to the measured PDD (with a SSD of 85 cm) for the TomoTherapy reference field (nominal size of 40x5 cm^2 defined at the isocenter).

Figure 3.5 shows the result of the PDD fitted to the measured curve for the reference field in black. In the same figure it can also be seen that the new weights used in the calculation of PDDs for different field sizes (5x5 and 10x5 cm^2) provide an appropriate basis for an accurate determination of the depth dose dependence of the TomoTherapy beam.

The PDDs were measured in a water tank using a diode detector. The discrepancies between the measured and calculated distributions in the build-up region, which corresponds to the region between the surface of the phantom and the point at which the CPE condition is reached (maximum dose), are due to detector effects and, therefore, are not of physical relevance. It was found that the depth of the maximum dose for the reference field corresponded to 12.4±0.4 mm.

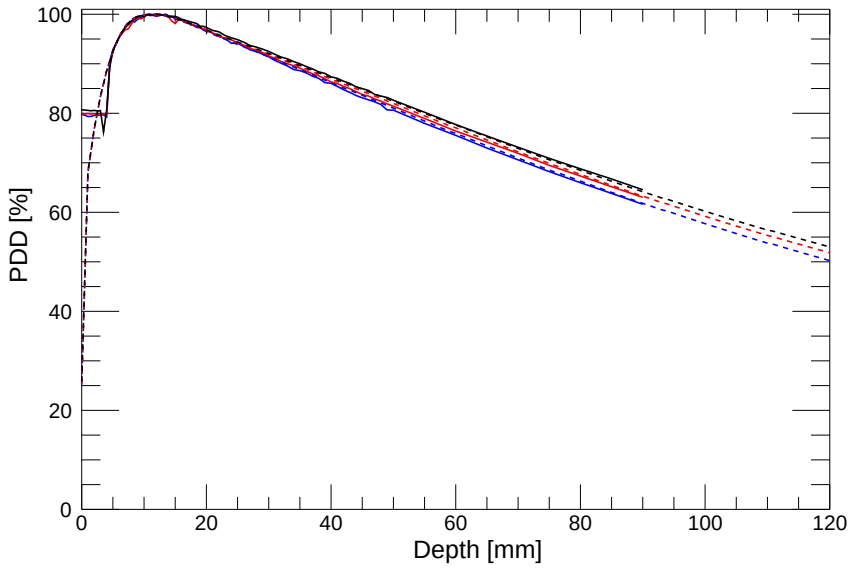

Figure 3.11: *Measured (continuous lines) and calculated (dashed lines) TomoTherapy PDD curves (with SSD=85 cm) for 5x5 (blue), 10x5 (red) and 40x5 cm^2 (black) normalized to the maximum value.*

Envelope and leakage

Figure 3.12(a) shows transverse profiles measured with a diode detector at 15 mm depth in a water tank with a SSD of 85 cm. The fields were defined by the maximum Y-jaws opening and a variable number of open MLC leaves, ranging from 0 to 64 (symmetric with respect to the CAX). Two important characteristics of the beam can be identified from this figure: (i) the cone shape of the beam, product of the unmodulated photon fluence (absence of flattening filter); and (ii) the low increase of the relative beam output with increasing field size, again related to the absence of a flattening filter and the subsequent reduction of head scatter contributions. For the calculation process described in Section 2.3.3, the profile measured for the biggest field size of 40x5 cm^2 was used as the radially symmetric envelope profile (after a deconvolution with the PBK at 15 mm depth to account for the relative fluence variation instead of dose variation).

A zoom into Figure 3.12(a) is presented in Figure 3.12(b) to visualize better the cross-profile measured when all the MLC leaves were set to be closed (relative to the dose in the central axis measured for the largest field available). It can be seen that the TomoTherapy system produces very low additional dose contributions (below 0.4%) outside the radiation field, which are due to intra- or inter-leaf leakage (in most of the distribution was of even less than 0.3%, with a mean of 0.14%). This is due to the design of the tungsten MLC leaves (10 cm long) coupled with an effective tongue and groove design. Even though small, the leakage contributions were considered in the calculations (see Section 2.4.4). The transmission through the Y-jaws was negligible, as in this direction the jaws are composed of up to 23 cm of tungsten.

These two distributions are the last components necessary to implement the dose calculation engine into the dose verification tool for TomoTherapy (as the source and PBK were already characterized).

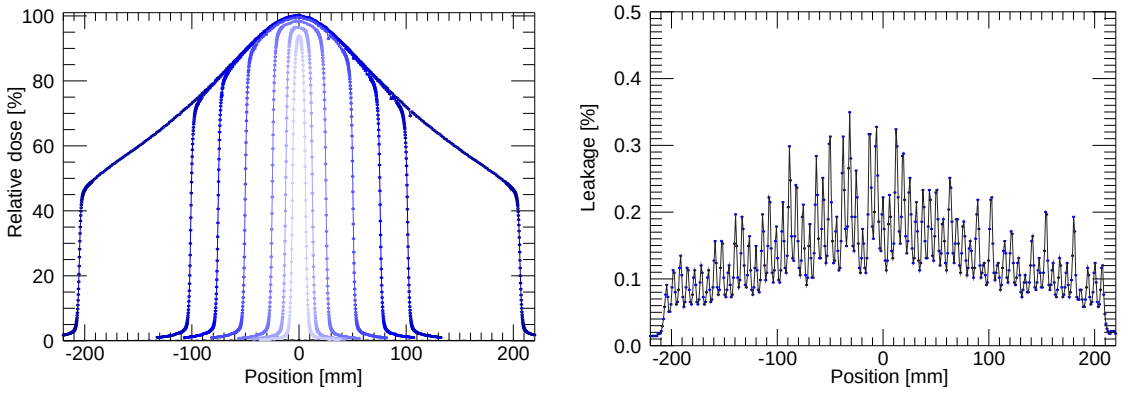

(a) (b)

Figure 3.12: *Helical TomoTherapy cross-profiles. (a) Transverse profiles for different MLC openings. (b) MLC leakage.*

3.2.2 Test results

The capability of the dose verification tool to reproduce dose distributions delivered by the TomoTherapy system to a homogeneous phantom was evaluated using each of its modes (static, topographic, rotational and helical). In this section, the comparisons between measured and calculated beam profiles and OFs are presented.

Static mode

The measurements performed to test the model were done in a water tank using a diode in the plane parallel to the couch with the linac pointing straight downwards. The dose was calculated for the same conditions, using a calculation grid of 1x1 mm^2.

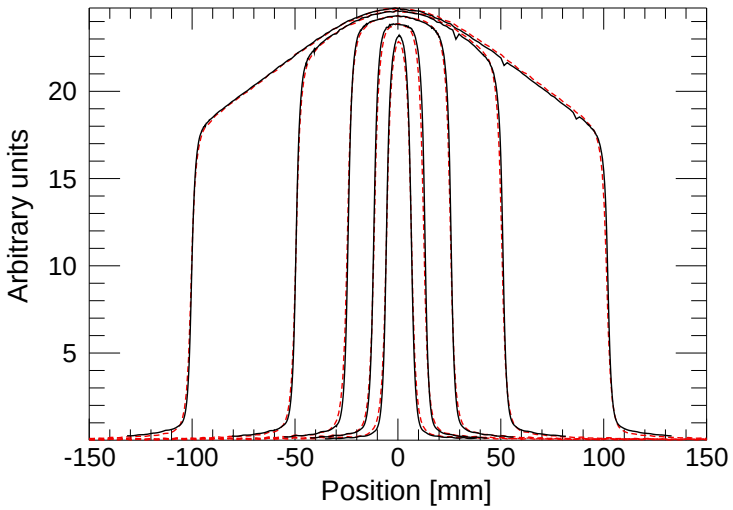

Figure 3.13: *TomoTherapy static calculation: X profiles. Measured (continuous line) and calculated (dashed line) profiles in the X direction for different MLC openings.*

Figure 3.13 shows the comparison of measured and calculated profiles in the X direction for different MLC openings, the Y-jaws projected a field size of 5 cm to the isocenter plane for every evaluated field. Consistent with the validation results, the profiles are found to be in good agreement with the values measured with a diode. All studied cases pass the acceptance criteria of 2%/2mm globally defined (with respect to the maximum dose). However, small differences were observed. For example, the maximum dose was underestimated by the calculation method in the smaller field size evaluated (1.25 cm at the isocenter in the X direction). Another mild disagreement is found in the "tail" of the biggest field shown (corresponding to a nominal field of 20 cm in the X direction), for which the measured dose was also slightly underestimated.

The modeling of OFs (shown as the solid line in Figure 3.14) shows a very good agreement with the measured values. The differences remain under ±2% of the normalization value (corresponding to a nominal field size of 10x5 cm^2). The maximum deviation was -1.98%, corresponding to the smallest field size evaluated of only 1.25 cm in the X direction. The differences between modeled and measured OFs for the rest of the evaluated fields remain below 1%.

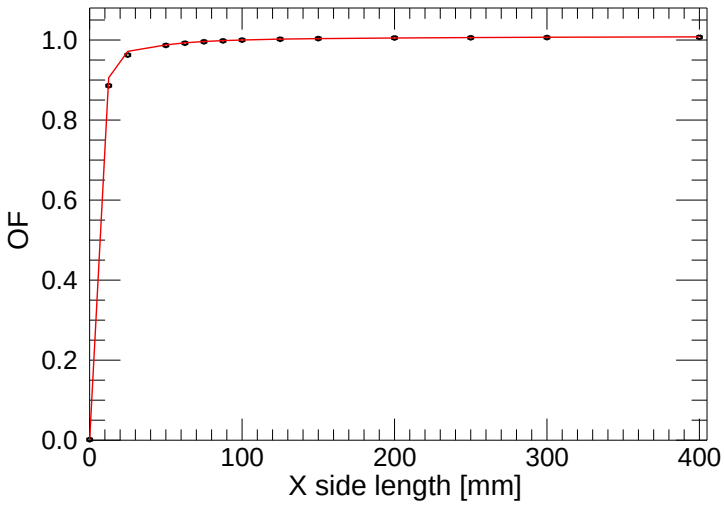

Figure 3.14: *TomoTherapy static calculation: Output factors. Measured (circles) and calculated (continuous line) OFs.*

Even though subtle, as the CF and OF distributions (Figures 3.10(b) and 3.14, respectively) exhibit almost no increase for field sizes larger than 5x5 cm^2, the OFs show a more pronounced increase due to the spread of the dose in water (phantom scatter), accounted for by the PBK.

Planar dose profiles using the static mode of the system were evaluated in both directions (X and Y) for simple MLC configurations (symmetric rectangular fields). Figure 3.15 shows the performance of the tool in the modeling of dose profiles in the main axis of the plane perpendicular to the CAX. The relative intensity of the profiles is displayed on a logarithmic scale. From this figure, it can be seen that the shape of the penumbras and the tails of the profile in the different directions are not the same. Although some deviations between the modeled and measured profiles (within the acceptance criteria) can be observed, the tool is able to predict correctly the shape of the different penumbras of the field in the complete scanned range (down to ∼0.5% of the maximum).

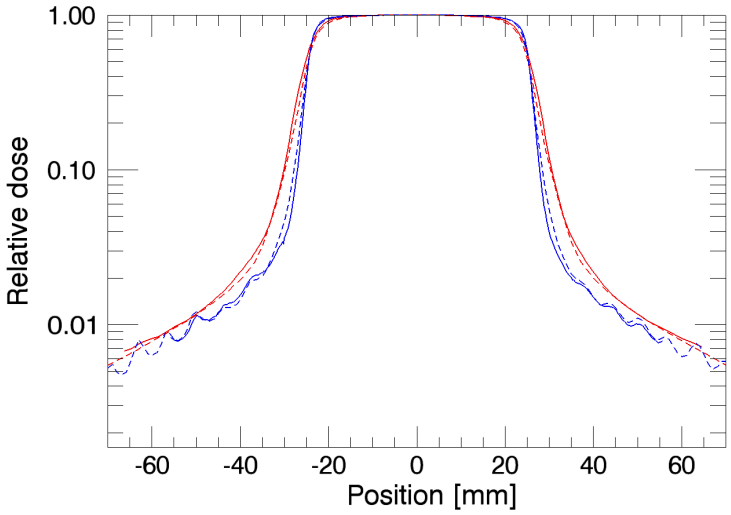

Figure 3.15: *TomoTherapy static calculation: X v/s Y profiles. Measured (continuous lines) and calculated (dashed lines) profiles in the X (blue) and Y (red) directions of a 5x5 cm^2 field.*

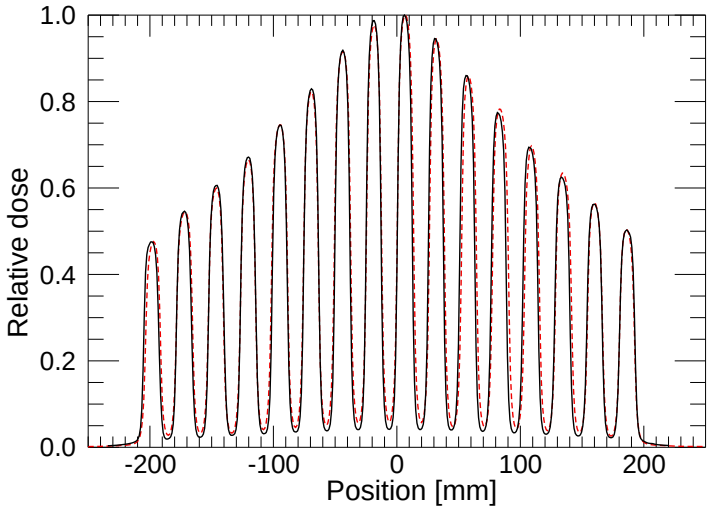

Figure 3.16: *TomoTherapy static calculation: Cross-profile of an MLC dose pattern. Measured (continuous line) and calculated (dashed line) profile. The Y-jaws are at their maximum opening and the MLC has every other pair of leaves open.*

Good agreement (below 2%/2mm) between the measured and calculated profile can also be seen in Figure 3.16, indicating that the tool is also well suited to predict dose distributions in asymmetric configurations for different MLC patterns. The maximum dose under each pair of open leaves was predicted very accurately, however, some small differences were observed for positions where the beam was blocked by the closed leaves (minimum dose). There, the dose was slightly overestimated by the calculation tool (∼1.5%). Also, it can be seen that certain penumbra regions within the pattern (specially on the right side with respect to the CAX) appear to be "shifted" from the measured positions (with a maximum shift corresponding to ∼2 mm). It is not clear if these discrepancies are a result of detector effects, interpolation and voxel averaging issues or inaccuracies related

to the MLC position and shape.

Dynamic mode

The dose verification tool was tested in the three dynamic modes (topographic, rotational and helical) for a simple MLC/jaws configuration (projecting a square field size to the isocenter plane of 2.5x2.5 cm^2) that was fixed during the complete treatment time. The different treatment parameters used for the evaluation of each mode can be seen in Table 2.3. The integral dose was calculated in the virtual cylindrical phantom (Figure 2.13) and delivered to the cheese-phantom (Figure 2.12(a)) using the same parameters and the same MLC configuration. The dose was measured with a film positioned at the coronal plane of the cheese phantom.

Figure 3.17 shows the results of the dynamic test. All the evaluated cases show good agreement (better than 2%/2mm) with the measured profiles in the longitudinal direction. The distributions were normalized to the dose at the center of the phantom. It can be seen that the measured profiles are not smooth and flat in the "plateau" region (Figures 3.17(a) and 3.17(g)), but show some discrepancies from the calculated results. This indicates that there is a temporal variation of one or more of the treatment parameters within the irradiation procedure. Although less evident (because of the narrower plateau region), this effect is also observed in the rotational case (Figure 3.17(d)). The second and third columns of the figure show the calculated relative 2-D dose distributions in the transverse and sagittal planes of the virtual phantom for the three dynamic modes. In Figures 3.17(b) and 3.17(c), some artifacts related with interpolation and grid size of the beamlet calculation can be seen.

3.2.3 Parameter variations

As seen in Figure 3.18, variations in the output of the beam (obtained in the static mode) were in general within the recommended ±2% (see Section 2.4.6) of the long term average. However, this was not always the case (see yellow line), thus, the impact of similar variations (and additional ones) in the integral dose of a simple helical case was investigated. The variations included systematic and random components.

In Section 2.4.6 the specific variations introduced to the beam output, the speed of the gantry and the couch velocity are given. These can also be visualized on the left side of Figure 3.19. On the right side of the figure, the result of introducing these variations can be seen. The reference helical distribution was calculated using the treatment parameters described in Section 2.4.6. The output, couch velocity and gantry speed were constant during the complete irradiation procedure. The distributions were compared (reference profiles are shown as continuous lines and the variation results as dashed lines) in the coronal plane of the virtual cylindrical phantom (shown in Figure 2.13) on the X and Y axis. Figure 3.19(b) shows that a random variation of ±2% in the output of the beam throughout the treatment does not introduce any considerable influence to its final outcome. Similar results are obtained by considering an uncertainty in the table velocity of 4% of the nominal value and a constant acceleration (of 0.001 mm/s^2). In this case the discrepancies on the longitudinal axis are greater than for the output variation, nevertheless, they still remain within ±2% of the maximum dose. The gantry speed variation, corresponding to a systematic sinusoidal variation (reducing the velocity by an amplitude of 4% of the nominal value as the linac moves upwards and increasing as the linac moves

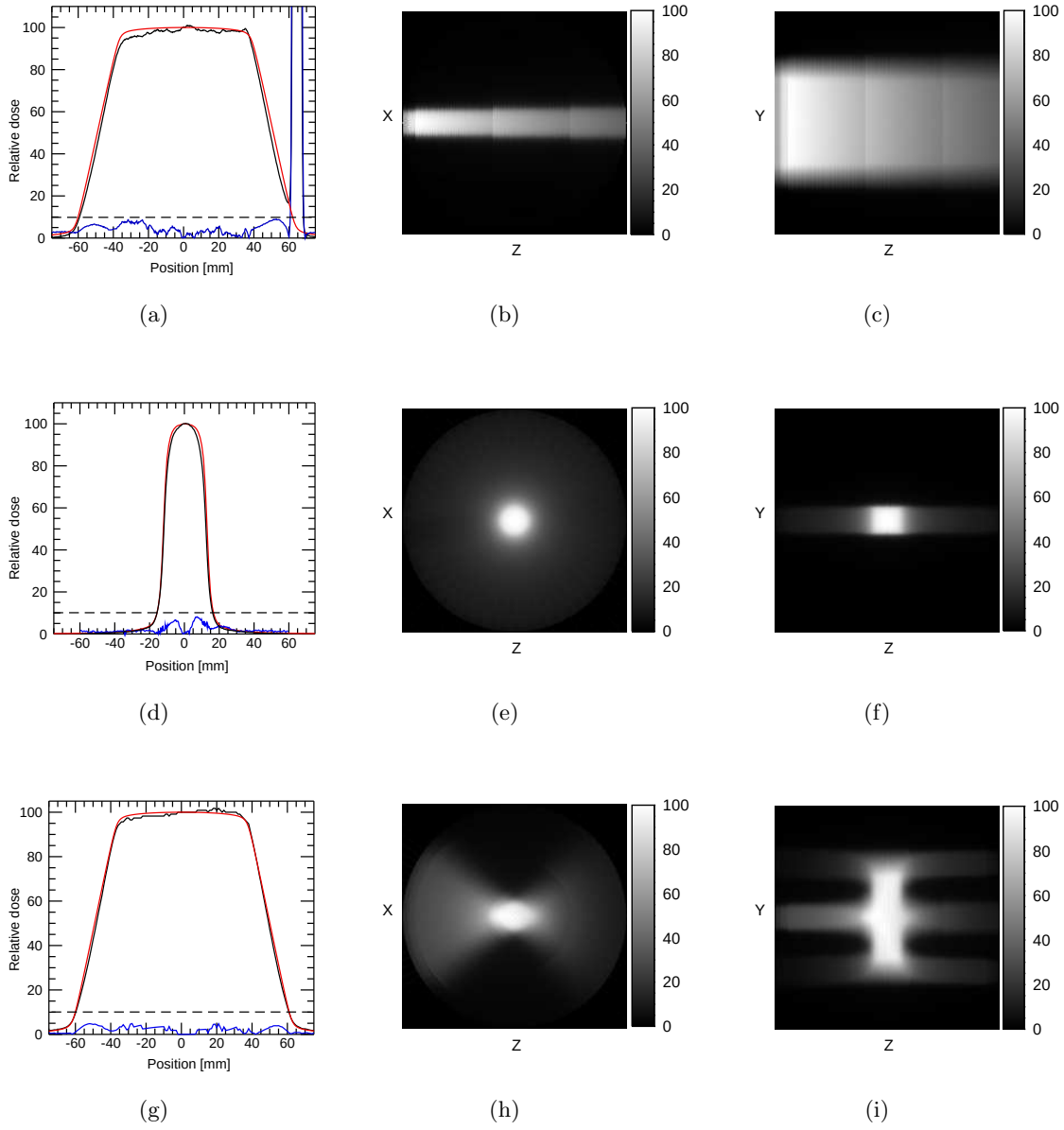

Figure 3.17: *TomoTherapy dynamic calculation: Longitudinal (first row), rotational (second row) and helical (third row) modes. The first column (from left to right) shows the comparison between the measured (black lines) and calculated (red lines) relative dose profiles in the longitudinal direction of the coronal plane at the cylindrical phantom. The gamma value (blue lines) with acceptance criteria of 2%/2mm is shown amplified by 10 for better visualization. Dashed lines indicate the limit of acceptance for the gamma index. The second column shows the distributions calculated in the transverse plane of the virtual cylindrical phantom and the third column shows the distributions obtained for the sagittal plane.*

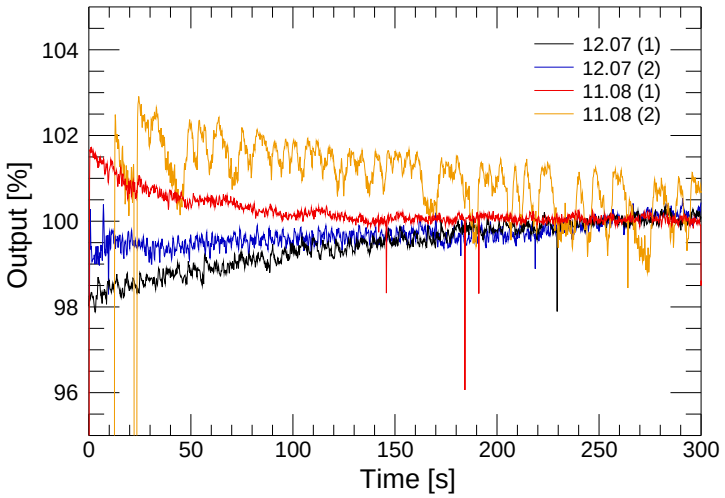

Figure 3.18: *Relative output variation normalized to the long-term average. The variation was measured in the static mode, using the maximum field size.*

downwards) plus a random component (also ±4% of the nominal value), shows a larger impact on the final outcome of the treatment (particularly in the transverse direction) compared with the other studied cases. However, the discrepancies in this case were still within acceptance criteria of 3%/3mm.

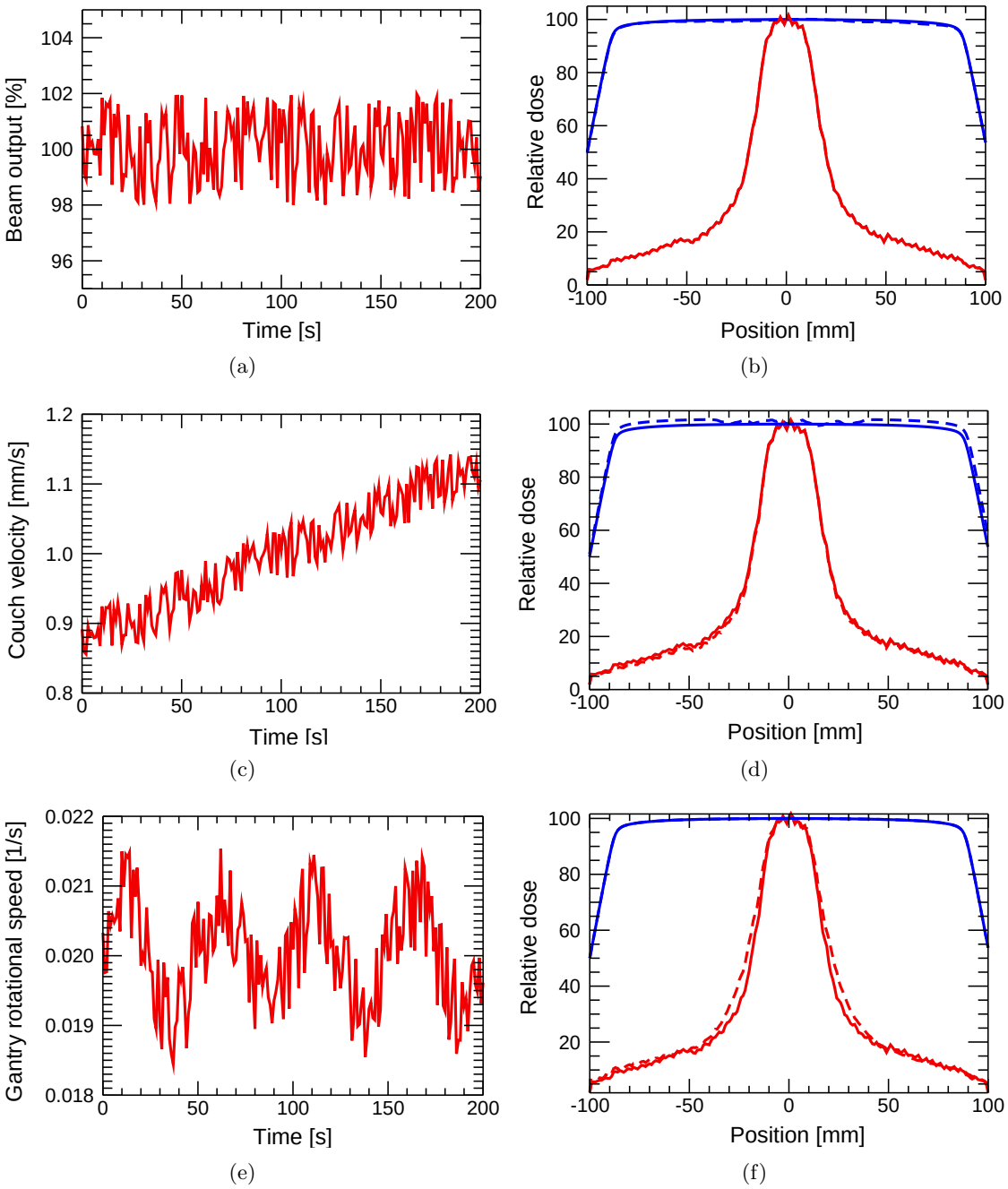

Figure 3.19: *Effect of random and systematic parameter variations on a test helical case. Left: variation introduced. Right: Comparison between calculated coronal profiles X (red) and Y (blue), with (dashed line) and without (continuous line) the inclusion of the variation.*

"Research is the process of going up alleys to see if they are blind."

Marston Bates (1906-1974)

4 Discussion

The rationale and methodology employed in the development of a dose verification tool for TomoTherapy were presented in Chapter 2. The main parameters of the dose calculation model have been determined and used to produce dose distributions delivered by the TomoTherapy system (using its different modes) in a homogeneous phantom. Additionally, variations in some of the delivery parameters were introduced. The integral dose obtained under these circumstances was compared with a reference distribution. These results were presented in the previous chapter. In this chapter, these results are analyzed in their context; addressing issues related to the establishment and implementation of the dose calculation model. A critical evaluation of the performance and usability of the proposed dose verification tool is also presented.

4.1 First part: The beam model

The dose calculation model presented in this study is a PBK-based algorithm that includes a detailed description of the extended source (focal spot + outer part, see Section 2.3.1). The determination of the poly-energetic PBK is based on pre-calculated mono-energetic DDK distributions obtained from Monte Carlo simulations (see Section 2.3.2).

The validation of this algorithm was performed using the 6 MV beam of a Siemens Primus linac for circular and quadratic fields. The focus of the model was set to accurately reproduce OFs and dose profiles for small fields, i.e., fields with sizes in the order of two times the range of the secondary electrons in the medium, or smaller. Considering that for a 6 MV clinical beam the forward range of the electrons corresponds approximately to 1.5 cm, CPE conditions will be present in the center of fields with diameters larger than 3 cm. This limit can be tightened to about 1.5 cm when considering, as discussed by Das et al. (2008), not the forward but rather the lateral range of the secondary particles (corresponding to approximately half of the forward range) as the key parameter defining the CPE conditions. The validation results, shown in Section 3.1.3, demonstrate that the model presented in this work provides an adequate approach to determine dose distributions in water for both small and large fields.

Within this section, an analysis of the extended source and of the methods used to reconstruct it, is presented. In particular, the effects observed in the measured strip-integrals, used for the focal spot reconstruction, are analyzed. With the source fully characterized, the individual influences of the source and the PBK on the final dose calculations (penumbra and output) for different collimator configurations are compared. Then, the results of the validation tests are discussed in detail, in order to assess the advantages offered by the approach presented here and also the current limitations of the model.

4.1.1 On the slit-method and the determination of the source

When performing slit-collimator measurements with the unshielded detector, it became clear that a part of the radiation detected by the diode was due to background radiation. Therefore, a shielding was added to the diode, particularly effective in the lateral direction (perpendicular to the slit).

Figure 4.1(a) shows measured strip-integrals of the source using two different shielding materials for the diode. The first attempt to reduce the background signal was made using a brass shielding, which resulted in an immediate reduction of the background. This confirmed the assumption that the signal was enhanced by radiation coming from parts other than the slit and served as a motivation to further reduce this effect by implementing a more effective shield made of tungsten. Even though the new shielding reduced the background signal even more ($\sim$4.5% with respect to the brass shielding), a small detector flux (of less than 1% compared to the maximum) was still observed at distances of 5 mm and larger. This flux presented a constant contribution to the measured slit. As it turned out that the associated (calculated) increase of the output factor free in air was still too large compared with the measured CFs, it became clear that it was not possible to reconstruct the complete source distribution (for distances larger than 5 mm from the source center) using the data of the slit measurement. The small discrepancies observed in the central part of the strip-integrals do not correspond to the background effect, but rather to the different SCDs used. The measurement taken the brass shielding was performed at an SCD that was 20 cm larger than the one used for tungsten, thus, the resolution of the slit at the source plane (projection of the slit-collimator opening) was coarser for a larger SCD.

To further understand the nature of the background signal detected by the diode, a slit-integral was measured varying the openings of the secondary collimators. It was found that the intensity of the background signal was field size dependent: increasing with increasing field size (though the effect was more subtle than the variations observed for the change in shielding material). As the field size was reduced, it could be noticed, that at certain scanning positions, the measured signal did not correspond to radiation coming from the source plane: the slit was blocked by the collimators. Figure 4.1(b) shows strip-integrals measured in the Y direction for the same experimental setup, but with a varying opening of the secondary collimators. It can be seen that the reproducibility of the measurements in the central part of the distribution is remarkably good. Also, as mentioned before, a reduction in the signal at the wings of the distribution is observed for the smaller field opening. It is interesting to see how the point where the collimator structure begins is clearly defined, as the collimator starts "eclipsing" the source plane from the detector's point of view. The distance from the source to the effective edge of the Y-jaws was l_{cy}=19.5 cm measured (obtained by manually measuring the distance from the collimator to the isocenter position and assuming an SAD of 100 cm), thus, a nominal field side of 6 cm

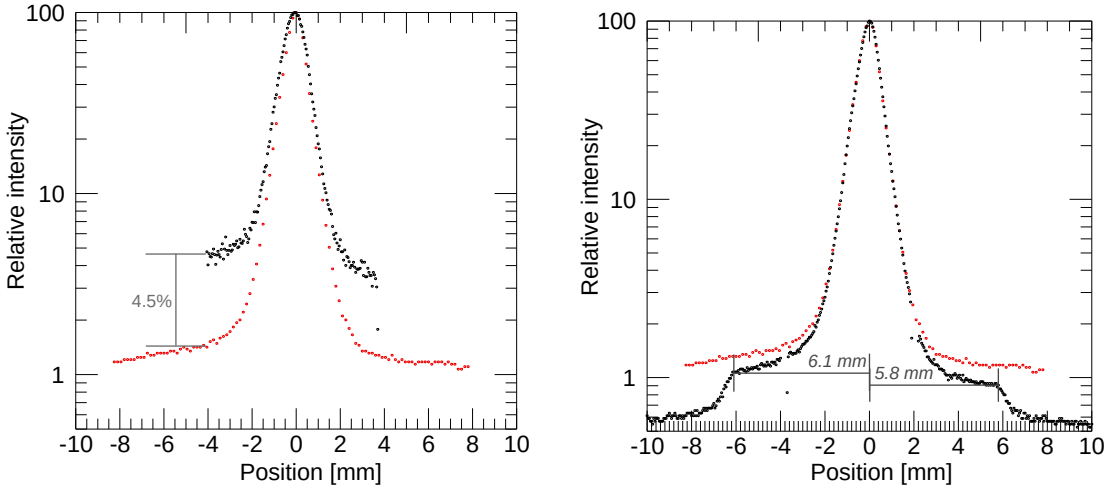

Figure 4.1: *Effects observed in the measurement of strip-integrals of the source. (a) Strip-integrals of the source measured for a nominal field size of 10x10 cm^2 in the Y direction using different shielding materials for the diode: brass (black circles) and tungsten (red circles). (b) Strip-integrals of the source measured in the Y direction using the tungsten shielding for different nominal field sizes: 6x6 cm^2 (black circles) and 10x10 cm^2 (red circles.)*

length (symmetric with respect to the central axis) in the Y direction, requires a collimator opening of 1.17 cm (5.85 mm to each side). It was found (as indicated in Figure 4.1(b)) that the collimator was blocking the slit from the starting position of the measurement (-10 mm) to a position of -6.1 mm from the central axis. The next blocking occurred at +5.8 mm (in very good agreement with the calculations). These openings, projected to the isocenter plane correspond to 3.13 and 2.97 cm respectively. As shown in Table 4.1, this analysis was later confirmed by the measurement of field sizes in the Y direction, showing a systematic CAX deviation of $\sim$1 mm and also a systematic deviation from the nominal size corresponding to $\sim$1 mm. The same analysis in the perpendicular direction was not performed because it was impossible to clearly resolve the exact point where the collimators first blocked the slit (it was a rather smooth change, perhaps associated with increase in the background scatter, interleaf leakage and transmission contributions). This is an example of an alternative use of the slit-method, which serves not only to reconstruct the source shape but also to study the fine details of the radiation field.

Besides the background effects, the radial variations of the source were also investigated by obtaining strip-integrals at different angles (see Figure 3.1). The first finding from this analysis was that the maximum value was not exactly the same for different angular positions, furthermore, it did not always correspond to the central axis position but was slightly deviated (within $\pm$1 mm). This indicates either that the source was not centered or that the device was not positioned correctly. As the stability of the slit measuring device (after manual rotation) and the precision of the alignment of the slit with the central axis (also done manually) yield an estimated uncertainty of the position of the detector of $\sim$1 mm, it was not possible to untangle these possibilities. Hence, it was assumed that the source was aligned with the central axis and the measured strip-integrals were

shifted in order to establish a coincidence between the maximum and the zero position. As the standard deviation of the FWHMs of the distributions was less than 0.1 mm, radial symmetry of the source was assumed as a good approximation for the focal spot reconstruction process.

Focal spots (inner part of the source) of medical linear accelerators have been determined in the past using different methods, such as slit-collimators (Munro et al., 1988), deconvolution techniques (Treuer et al., 1993) and the analysis of OFs (Zhu et al., 1995). As stated before, the slit-collimator method was selected for being the most direct and quantitative among them. Jaffray et al. (1993) studied the focal spots of several linacs (including Varian, Siemens and AECL) for different energies, obtaining focal spots with FWHMs in the range of 0.6 to 2.9 mm with deviations from rotational symmetry varying from 0 to 1.3 mm. In the work presented here, a symmetric focal spot, with a FWHM of 0.50±0.08 mm was obtained. This result is similar to that found by Jaffray et al. (1993) for a Siemens KD-2 linac using the 6 MV beam (major axis: 0.7 mm, minor axis: 0.5 mm), as shown in Figure 3.2.

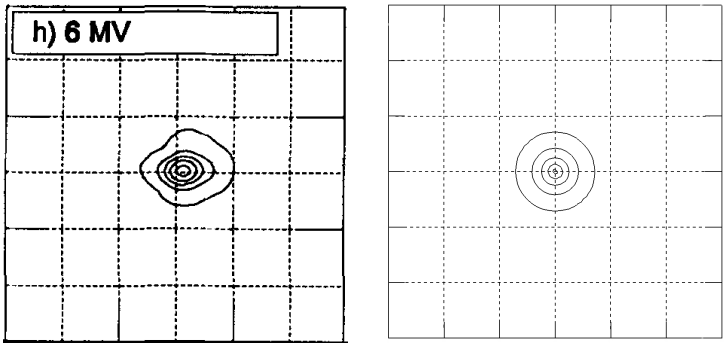

(a) (b)

Figure 4.2: *Comparison of focal spots. Dashed lines divide the plane in regions of 1x1 mm^2. The contour lines indicate the 10%, 30%, 50%, 70% and 90% of the maximum intensity. (a) Focal spot of a a Siemens KD-2 linac using the 6 MV beam from Jaffray et al. (1993). (b) Focal spot of a Siemens Primus linac for the 6 MV beam, obtained for the validation of the beam model using the slit-method.*

Due to the aforementioned limitations of the slit-method to accurately determine the distribution of the source at off-axis positions, the outer part of the extended source was determined using the same concept as in the numerical single source model described by Chui et al. (2003). This method obtains the (symmetric) shape of the radiation source by fitting the head scatter factors (or CFs) of quadratic fields of different sizes. Therefore, the accuracy on the determination of the source distribution using this method depends directly on the accuracy of the CFs. It was assumed that the measured CFs using the diode detector (with an appropriate build-up cup) were reliable (i.e., sufficiently accurate) for field sizes larger than 2x2 cm^2 and, thus, were used for the determination of the outer part of the source (shown in Figure 3.4). Although this method presents a much simpler approach to determine the radial distribution of the source, its usefulness to obtain the inner part is limited by its resolution (it would require a huge amount of CFs measured for very small fields to map the steep slope of the inner part of the source) and accuracy (large uncertainties are associated with small field measurements).

The method to construct a radial distribution of the source by the combination of the slit-method for the focal spot and the CFs analysis for the outer part, provides a sufficiently accurate and flexible tool to calculate dose distributions and OFs in water for a broad range of field sizes (from a few millimeters up to 40 cm), as shown in Section 3.1.3.

4.1.2 On the pencil beam determination

Since the introduction of the concept of pencil beam kernels for photon dose calculations, many ways of obtaining the PBK have been used. These include: deconvolution techniques (Chui and Mohan, 1988), experimental methods (Ceberg et al., 1996; Storchi and Woudstra, 1996), Monte Carlo based techniques (Mohan and Chui, 1987; Ahnesjö and Trepp, 1991; Bourland and Chaney, 1992) and analytic/parametric approaches (Ahnesjö et al., 1992; Bortfeld et al., 1993; Nyholm et al., 2006). As stated in Section 2.3.2, a Monte Carlo based technique was used to obtain the final PBK from pre-calculated point kernel distributions (appropriately weighted to fit a measured PDD curve in a broad beam configuration). Once the mono-energetic point kernels (DDKs) are obtained, getting the weights of the spectrum (from the fitting procedure) is conceptually a straight forward procedure. This simplicity provides the approach with the flexibility of reusing the same point kernels in the calculation of PBKs for any beam (if the nominal energy is included in the calculated DDKs).

In Figure 3.5, an example of how the Monte Carlo based PBK accurately reproduces the depth dependence of the absorbed dose in the CAX for quadratic fields in the range of 5x5 cm^2 to 20x20 cm^2 for a 6 MV beam of a Siemens Primus linac can be seen.

Although the concept of obtaining the poly-energetic PBK is clear, the method is not exempt of implementation issues. The most prominent are: (i) the interpolation of the DDK distributions (which originally come in a spherical geometry, not very practical for planar dose calculations) and (ii) finding the correct weights of the spectrum by means of the minimization.

The raw DDK data coming directly out of the Monte Carlo simulations needed some processing before being ready to be used for the determination of the PBK and as the convolution kernel distribution in the final dose calculation (here, interpolation into cartesian coordinates is needed for the use of FFT). As these distributions are symmetric around the polar angle (see Figure 2.4), they were transformed into cylindrical coordinates (after assigning the dose of each voxel to an effective radius and an azimuthal angle). This process required interpolation of the data. It was found that a bilinear interpolation on a logarithmic base was an appropriate method. It was also found that the result of the final PBK was strongly influenced by the value of the central bin in the DDK distributions, because close to the origin the slopes of the distributions are very steep. Therefore, the interpolation/rebinning process required a careful consideration of these effects. These issues have been discussed by Eklöf et al. (1990); Rathee et al. (1993) and Ahnesjö and Aspradakis (1999).

From the pre-calculated DDK distributions for 24 energy bins (between 250 KeV and 6 MeV), 24 mono-energetic depth dose profiles were calculated. These were used in the least-squares minimization process to obtain the spectrum weights (see Equation 2.7). It was found that the dependence of the final dose on the weights was not very strong (i.e., many different combinations yield the same or at least a very similar solution), therefore, some constraints were set in order to force the parameters (energy weights) to vary only

little with respect to the first guess (Mohan's spectrum for 6 MV, Mohan et al. 1985). It was also necessary to constrain the parameters so they could only take positive values (Scholz et al., 2003), as otherwise the solution would have not been physically valid.

4.1.3 On the individual effects of the source and pencil beam kernel

The convolution-based method to calculate planar dose distributions has been presented in Section 2.3.3. Here, the individual characteristics of the convolution kernels (source and pencil beam) that shape the penumbra of the field and are responsible for the increase of the output with the increase of field size are analyzed.

The individual influence of these effects on the OF is presented in Figure 3.7. It can be seen that none of the effects by themselves would account for the precise increase of output with field size, but the combination of both yield a very good agreement with the measurements for both circular and quadratic configurations. In the latter, greater discrepancies in the small field section of the curve were observed due to the uncertainties associated to the field size and the increase of the calculation grid size from 0.1x0.1 (for the circular fields) to 1x1 mm^2. It can be noticed that the PBK by itself (point source approximation) already provides the basic shape of the curve by reducing the output as the field sizes decrease and steepening the curve as we enter the regime of non-CPE conditions within the field (for $s \lesssim 2$ cm or $d_c \lesssim 10$ mm). However, it cannot model the "eclipsing" of part of the radiation source, which is particularly important for the very small fields, where sections of the inner part of the source (steepest part of the extended source distribution) are being blocked. Even though the outer part of the source does not have an important influence on the OFs for the circular fields, it is very important for the large quadratic fields, as it accounts for the head scatter contribution (projected into the source plane) that represents an important part of the total increase in output for larger field sizes. The major contribution to the head scatter comes from the flattening filter. This can be deduced comparing the increase of CFs with field size for the linac (Figure 3.3) with the one for the TomoTherapy system (Figure 3.10(b)), which does not use flattening filter.

Figure 4.3 shows the individual 2-D convolution functions, scaled source and PBK at the measurement depth as used in the determination of the planar dose distributions for the two field configurations used in the validation of the model (circular fields, shaped by add-on cylindrical collimators and quadratic fields shaped by the Y-jaws and the MLC of the linac). The field penumbra modeled by the different effects (individually and combined) is also included. The effects on the cylindrical configuration will be analyzed first.

It can be seen from Figures 4.3(a), 4.3(b) and 4.3(c) that the source and pencil beam kernel distributions are very similar in shape and intensity. However, the scaled source displays a steeper slope than the PBK at the measurement depth. As the circular fields were defined by single cylindrical collimators located at a fixed distance from the source, the presented model produces radially symmetric distributions. This is due to the additional facts that the PBK is defined to be radially symmetric (see Section 2.3.2) and that the reconstructed source was assumed to be centered and radially symmetric (see Sections 3.1.1 and 4.1.1). This symmetry was confirmed by diode measurements performed in the X and Y directions, for which the discrepancies in the penumbra were within ± 0.1 mm, indicating that the assumptions on the source were appropriate. Figure 4.3(d) shows the penumbra of a field of 8.6 mm in diameter (corresponding to the collimator with a diameter d_c=5 mm), measured (red) and modeled (black): by the combined effect (dot-dashed line) and considering the source (dashed line) and PBK (dotted line) effects individually. The

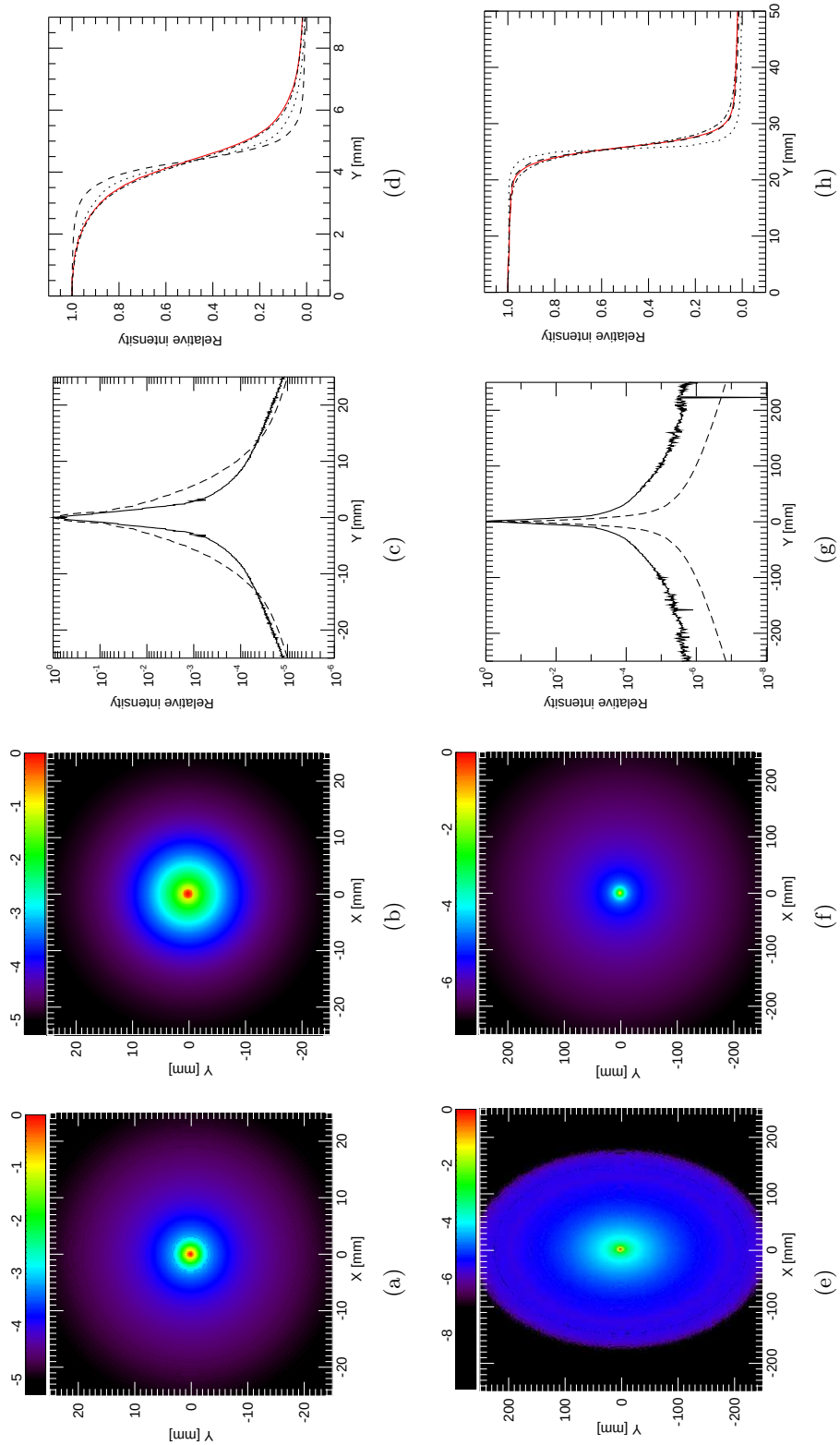

Figure 4.3: *The extended source (considering the relative distances between the collimators, the source and the measurement plane), the used poly-energetic PBK (at the measurement depth) and their individual effects on the calculation of planar dose distributions for the circular (top) and quadratic (bottom) fields. From left to right: (a,e) scaled 2-D source distributions at 15 mm. (b,f) 2-D PBK distributions. (c,g) Cross-profiles of the source (continuous lines) and PBK (dashed lines) distributions. (d,h) Relative dose profiles measured (continuous red lines) for a field performed by the circular collimator with d_c=5 mm (d) and for a quadratic field of side length s= 5 cm (h). The non-solid lines indicate the calculated profiles for a point source (only the PBK effect was considered, dotted lines), free-in-air (only the source effect was considered, dashed lines) and using the extended source (both effects were considered, dot-dashed lines).*

combination of both effects can almost perfectly model the drop of the dose at the edge of the field. Although the point source approximation reproduces the penumbra of the field slightly better than the case in which no energy transport of the secondary electrons is considered, neither of the individual effects by themselves can model the penumbra of the small circular fields as good as the combination of them. It should be noticed that the point source approximation would be sufficient to fulfill an acceptance criteria for the dose circular dose profiles of 2%/0.5 mm (as they are normalized to the maximum here), but it would not reproduce the correct output variation with field size.

The planar dose calculations for the quadratic fields show a different scenario. Here, the fields are shaped by independent collimators (in X and Y) located at different distances from the source. Therefore, even though the source is radially symmetric, the scaling required to perform the fluence calculations (c_x and c_y in Equation 2.8) makes the source unevenly rebinned with respect to the X and Y axis as shown in Figure 4.3(e). This effect will naturally yield different penumbras for the X and Y directions of the field as it is shown in Figure 4.5. Figure 4.3(f) shows the 2-D PBK distribution at the measurement depth (15 mm). It is actually the same distribution already shown in Figure 4.3(b), but this time a longer range of the distribution was considered in the calculation (the distributions were truncated at the total extent of the calculation plane, which corresponded to 5x5 cm^2 with a calculation grid of 0.1x0.1 mm^2 for the circular fields and to 50x50 cm^2 with a calculation grid of 1x1 mm^2 for the quadratic fields). It can be seen from Figure 4.3(g) that, in this case, the dominant effect is the extended source and, in contrast to the circular case, the slope of the kernel in this configuration is much steeper than the slope of the scaled source in the Y direction. Figure 4.3(h) allows us to analyze the performance of the developed model regarding the penumbra of a 5x5 cm^2 field measured with a diode in the Y direction (shown in red). As expected, the PBK by itself (point source approximation, dotted line) is not enough to provide an accurate modeling of the penumbra of the field, although the agreement is in the verge of the acceptance criteria of 2%/2mm (globally defined for the dose difference criterion). The agreement presented by the complete dose calculation (dot-dashed line) and by considering only the extended source effect (dashed line), is much better than for the point source. It can be noticed that here the predominant effect is the extended source and that the inclusion of the PBK into the calculation, does not cause an important improvement of the result. In fact, in this particular case, the extended source effect by itself can already model the shape of the penumbra (plus the tail). This result is even slightly better than the one for which the PBK is included. However, the differences in the tail of the distribution can be attributed to the averaging within one pixel (1x1 mm^2) or to convolution effects and not to physical effects, thus, they can be neglected. In the penumbra itself (defined in the area between 10%-90% of the maximum) the distributions are almost indistinguishable (i.e., within 1 mm). Finally, it can be confirmed that the consideration of the extended source improves the result with respect to the point source (the PBK needs to be considered on the planar dose calculations in water because, as previously discussed, it also contributes to the correct increase in output with field size).

4.1.4 On the validation and field size considerations

The selection of a diode for the validation of the method was based on the fact that this type of detector has shown good agreement with Monte Carlo simulations for small fields (Sánchez-Doblado et al., 2007; Scott et al., 2008). Although no attempt was made to model possible detector specific effects (composition or size) that could affect the dose dis-

tributions for very small fields, the calculations presented here are in very good agreement with the data measured with a diode.

As the dosimetry of small fields has been associated with large uncertainties, the OFs for the circular small fields were measured using two methods: the diode measurement and a combination of the diode and parallel plate chamber (the Large Area Chamber (LAC) method, see description in Section 2.3.4). Figure 4.4 shows the difference between these two methods. It can be seen that the agreement is in general acceptable, but, nevertheless, some discrepancies (larger than 2%) can be found (with a maximum deviation of 2.6% for the collimator with d_c=4). These discrepancies can be explained by the different amount of steps involved in each method and some intrinsic effects of the LAC measurement. While the diode determination only involves the uncertainty associated with the point measurements of the evaluated and the reference field, the LAC method includes four factors (see Equation 2.10). The effective area of the chamber (taken from the technical specifications), the reference dose and the measured dose for the evaluated field, have small uncertainties associated (the SD associated with these measurements was less 0.1% of the measured value). The uncertainty in the determination of the relative profile is by itself not relevant either. However, if it is considered that the symmetric profile is then integrated over the area of the chamber, the total uncertainty gets specially amplified in regions far from the central axis as

$$I = 2\pi \int_0^{R_{LAC}} r \cdot p(r)\, \mathrm{d}r, \tag{4.1}$$

where R_{LAC} is the effective radius of the parallel plate chamber and $p(r)$ is the relative intensity of the profile measured at the radial position r. It was assumed that the response of the chamber was homogeneous within its effective area, but the validity of this assumption was not confirmed.

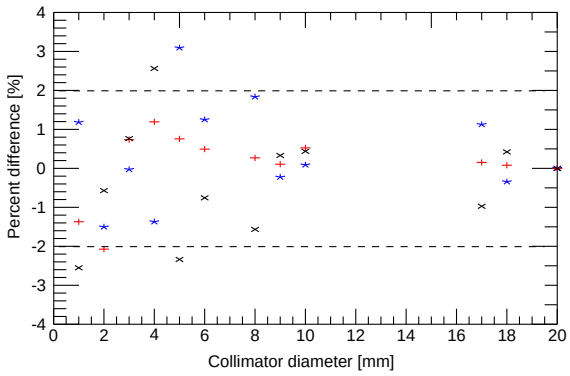

Figure 4.4: *Difference between OFs. Between the diode measurements and determined by the LAC method (×), between the diode and the calculations (+) and between the LAC and the calculations (⋆).*

Figure 4.4 also shows the performance of the presented algorithm in the modeling of OFs for small fields, for which the results are compared with measured values (using both methods). With the exception of one outlier (for each method), the model can reproduce the OFs for small fields with an accuracy better that 2% of the normalization value (corresponding to the biggest circular field).

Table 4.1: *Measured field sizes and deviations from the CAX for quadratic fields in the X and Y directions. The sizes of the fields were determined for 50% of the maximum value. CAX deviations and field sizes were obtained using Mephysto mc^2.*

Nominal side length [cm]	Direction	Measured size [cm]	Size difference [cm]	CAX deviation [mm]
0.5	X	0.42	-0.08	0.21
0.5	Y	0.72	0.22	0.76
1.0	X	0.73	-0.27	0.18
1.0	Y	1.09	0.09	0.75
5.0	X	4.72	-0.28	0.31
5.0	Y	5.07	0.07	0.76
10.0	X	9.74	-0.26	0.27
10.0	Y	10.06	0.06	0.79
20.0	X	19.79	-0.21	0.13
20.0	Y	20.05	0.05	0.81
30.0	X	29.74	-0.26	0.00
30.0	Y	30.09	0.09	0.89

As seen in Figure 3.7(b), the method also performed well in the modeling of OFs for the quadratic fields. It was already mentioned that the discrepancies in the small field section of the curve are not due to poor modeling, but rather related to a combination of effects: (i) the coarse grid of 1x1 mm^2 (in the context of the fields of 5, 10 and 20 mm being evaluated), (ii) the uncertainty in the field size (which will be discussed later in this text) and (iii) the fact that, for these fields, the inner part of the source started to be occluded by the collimators: due of the steepness of its distribution in this part, a small variation in the field size has a great impact on the output variation.

As shown in Section 3.1.3, calculated profiles in water were within the acceptance criteria of 2%/2mm for the quadratic fields in the Y direction and 2%/0.5mm for the circular fields. The agreement on the small field penumbras was especially good, as a very fine calculation grid was used and accurate information on the position and geometry of the collimators (aperture and length) for every evaluated field was available. There were two sectors with discrepancies of moderate relevance: (i) the central section of the profile using the collimator with a diameter d_c=2 mm (difference $\sim$2%) and (ii) the tail of the largest collimator profile (difference $\sim$2%). The first could be explained by a possible misalignment of the diode with the CAX (implying a lower maximum value). A possible explanation for the second discrepancy may be related to the interpolation of the PBK or to inaccuracies in the determination of the outer part of the source, more specifically, in the interface section between the inner and the outer part (where the slope is still pronounced and was obtained from the CF analysis for relatively small fields, thus more prone to uncertainties). Another explanation could be the spectral variation at off-axis

positions. In the future, this effect could be further investigated and incorporated into the model. The study of lateral spectral variations was not within the scope of this thesis, as this effect is negligible for the TomoTherapy system (due to the absence of a flattening filter).

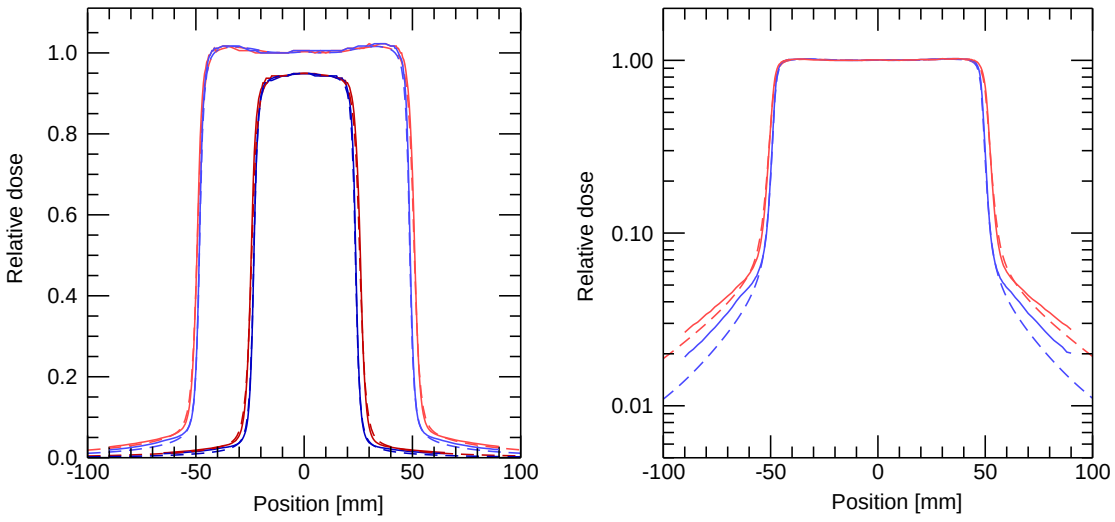

(a) (b)

Figure 4.5: *Quadratic fields: X and Y profiles. The calculations were done considering the measured field sizes and the CAX deviations given in Table 4.1 as input parameters. (a) Measured (continuous lines) and calculated (dashed lines) profiles in the X (blue lines) and Y (red lines) directions for two field sizes: 5x5 cm^2 (dark lines) and 10x10 cm^2 (light lines). (b) Same comparison as in (a) shown in logarithmic scale only for the field size of 10x10 cm^2.*

In the case of quadratic field configurations, a fine calculation grid was not justified, as the nominal size of the fields deviated from the measured sizes on a millimetric scale (in contrast to the circular case, where the geometry permitted sub-millimetric accuracy in the field determination). The small disagreements shown in Figure 3.8(b) for the two biggest fields may be due to the fact that a radially symmetric envelope profile (that accounts for the horn-effect) was used in the dose calculations, which may have been a coarse approximation (although all the evaluated profiles passed the acceptance criteria). As a systematic shift of approximately 1 mm between the measured distributions and the calculated profiles was found, the set of results was shifted for better comparison (a detector misalignment was assumed). This was a motivation to further investigate the asymmetries in the radiation field and the deviations from the nominal field size. Hereafter, the findings concerning these effects are described.

The field sizes and CAX deviations were obtained for several quadratic fields (using the DataAnalyze feature of the Mephysto mc^2 software[1]). The sizes and deviations obtained in each direction are shown in Table 4.1. Three systematic effects can be clearly identified: an asymmetry of the field in the Y direction (the asymmetry in the X direction is negligible),

[1]Mephysto mc^2 (PTW, Freiburg, Germany). Software for the controlling of water phantoms, data acquisition and analysis.

a negative deviation from the nominal field size in the X direction and a positive deviation from the nominal field size in the Y direction. The field size variation in the X direction is quite significant; of the order of -2 to -3 mm. The rest of the variations are within 1 mm and can be explained by detector positioning effects. However, it is interesting to note the concordance of the CAX and size deviations in the Y direction with the predictions made in Section 4.1.1, which were based on the analysis of a strip-integral measured for a 6x6 cm^2 field in the Y direction (see Figure 4.1(b)). The slit-method predicted a 1 mm increase from the nominal field size in the Y direction, shifted 0.8 mm from the CAX, which is in very good agreement with the measured field size deviation (0.97±0.06 mm, $\bar{x} \pm \sigma$) and CAX deviation (0.79±0.05 mm, $\bar{x} \pm \sigma$).

Figure 4.5(a) shows the comparison between measured and calculated profiles in the X and Y directions for two different quadratic fields (5x5 and 10x10 cm^2 in size) considering size and symmetry effects, which can be clearly identified. In general, a very good agreement between measured and calculated distributions can be seen. Now, looking at the profiles in a logarithmic scale (Figure 4.5(b)), it can be seen that the umbra region of the profiles (low dose region, outside the radiation field) is not perfectly modeled. This can be explained on the basis that transmission and leakage effects have not been considered in the calculation algorithm, as perfect collimators were assumed. It can be seen that the developed model reproduces the umbra better in the Y direction. This is not a surprise, as the Y-jaws are thicker than the MLC (which shapes the field in the X direction) and there is no contribution from interleaf leakage.

4.1.5 On the advantages and limitations of the model

After a thorough evaluation of most of the aspects concerning the implementation and validation process for the presented model, a critical view on the strengths and weaknesses of this algorithm can be presented.

Advantages

The algorithm was successfully validated, predicting accurately OFs and planar dose distributions in water from very small to large field sizes, making it a useful QA tool for the performance of the linac. As the complete range of evaluated field sizes was well reproduced, the transformation of relative values into absolute dose becomes straightforward (only a dose conversion factor measured in a reference field is needed), which enables this method to be used as an alternative to the conventional dosimetry of small fields. As a by-product of the slit-method (used for the reconstruction of the source), accurate information on the disposition of the components in the linac head (collimators) that can be used to predict the exact geometry of the radiation field was obtained. This by itself can be used as a supplemental QA test.

Recently, Djouguela et al. (2009) have investigated an analytical approach to reproduce dose profiles of narrow photon beams. They have used an analytic/parametric convolution kernel based on the Lorentz function that can account for both, the source extension and the energy transport of secondary electrons in a single radially symmetric function. They found a very good agreement between a set of measured and calculated profiles in the range of 10 to 30 mm in side length (at three different depths for two different energies). Even though they present an attractive, purely mathematical approach, the model described throughout this thesis provides a more general and physically meaningful

one; as it can accurately reproduce not only dose profiles, but also the correct field size dependent increase of OFs for a very broad range of field sizes (including fields with diameters of ∼2 mm). Every component of the dose calculation engine has been carefully studied (identifying its individual influence on the final dose) and characterized in its physical context.

Limitations

As the aim of this method was to validate a model that can be implemented into a dose delivery verification tool (for a homogeneous phantom), the performance of the model in non-homogeneous media was not addressed. This is an important limitation if the method is intended to be used for treatment planning. As it has otherwise shown to be a very accurate method for the determination of dose in water, the presented method leaves an open door for further investigations and generalization of the model in this respect. Also as further extensions of this work, some effects can be mentioned, whose relevance can be studied to evaluate the benefit of their inclusion into the dose calculation engine. These include: lateral spectral variations, explicit modeling of the shape of the MLC and Y-jaws, and the consideration of leakage and transmission contributions.

A crucial component of this model, that represents both a strength and a limitation, is the use of the slit-method. This method has proven to be extremely accurate and useful in the determination of the precise shape of the focal spot and in the study of other effects (field size and symmetry). However, as it is a custom made device that is not available in every institution, its use cannot be widely recommended. At least not until a commercial alternative for the slit-device is created or until a method that shares the same accuracy characteristics to determine the shape of the focal spot, is found.

4.2 Second part: The dose verification tool for TomoTherapy

The dose verification tool for TomoTherapy is based on the dose calculation model developed throughout this thesis. This model showed to be very accurate in the determination of dose distributions using both large and small fields (see Section 3.1 and 4.1).

This section presents an analysis of several aspects related with the implementation of the calculation model into the verification tool and with the evaluation of its performance in the different modes of the TomoTherapy system. Additionally, the uses and advantages offered by this tool and the issues related with its implementation into the clinical QA program are discussed.

4.2.1 On the implementation of the model into the tool

The model was successfully implemented into the dose verification tool. For this, it was required to obtain all components necessary to perform the planar dose calculations according to Section 2.2 (i.e., the extended source distribution, the PBK and envelope distribution, besides the information on the system's geometry).

Extended source and head scatter effects

In Figure 4.6(a), the reconstructed distribution of the TomoTherapy source (blue line), obtained using the slit-method, is compared with the distribution found for the linac's beam (red line). It can be seen that the TomoTherapy focal spot has a larger FWHM (of 0.72±0.05 mm) than the one obtained for the linac and that the intensity (for the same radial positions) remains higher at radial positions $\lesssim$5 mm (that approximately coincides with the position from which a background signal can be identified on the red line). From this position on, the intensity of the TomoTherapy source continues to decrease until a background signal can be identified (of almost one order of magnitude lower than for the linac case). This difference in the background intensity is related to the fact that the absence of flattening filter in the TomoTherapy system reduces significantly the head scatter contributions and thus, the detector signal used for the reconstruction (strip-integral) is less "contaminated" by scatter radiation.

The influence of the background signal in the determination of the correct extended source (able to reproduce the field size dependence of the CFs) can be better understood from Figure 4.6(b), where CFs were calculated (according to Equation 2.5) using the different reconstructed distributions and assuming the same geometric configuration (the detector is positioned at 100 cm from the source and the circular fields are produced by perfect collimators located at 20 cm from the source). It can be seen that the CF distribution using the TomoTherapy reconstructed source (blue line) already resembles the expected field size dependence (Figure 3.14), whereas using the linac's distribution (red) the distribution shows a clear overestimation of the expected increase of CF with increasing in field size (Figure 3.7).

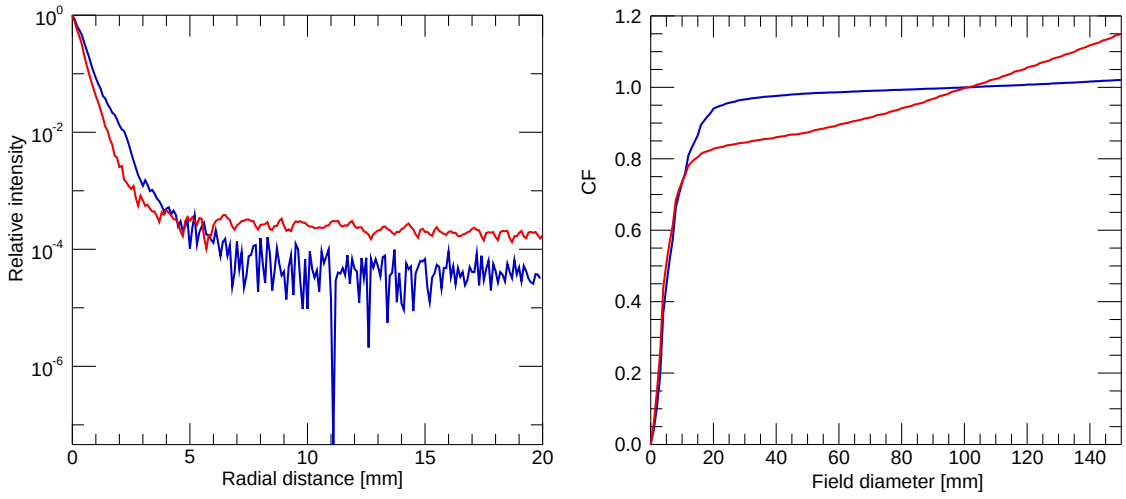

(a) (b)

Figure 4.6: *Comparison of reconstructed focal spots and the associated CF distributions. (a) Reconstructed radial distributions of the linac (red line) and the TomoTherapy (blue line) sources. (b) Comparison between the variation in CF associated with the increase in field size using the linac's (red line) and TomoTherapy's (blue line) reconstructed source distributions.*

Pencil beam kernel and percentage depth dose curves

The PBK obtained by the method described in Section 2.3.2, proved to be appropriate to model the depth dependence of the dose in the central axis for different field sizes (as shown in Figure 3.11) and, in combination with the extended source, was also able to reproduce both the increase of the OFs depending on the field size (Figure 3.14) and the shape of the penumbra for different field configurations (see Figure 3.15 and 3.16).

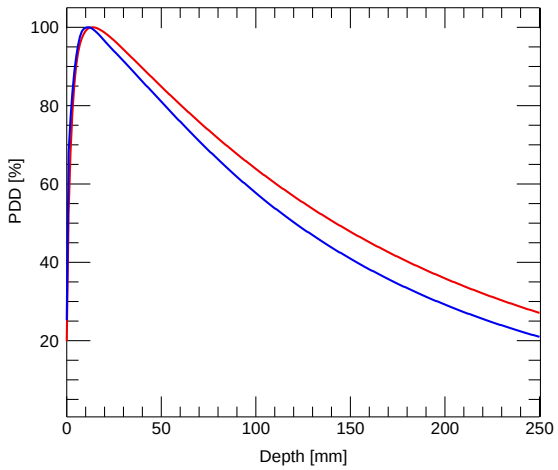

Figure 4.7: *Comparison of calculated PDDs for the linac (red line) and for the TomoTherapy system (blue line) considering a nominal field size of 5x5 cm^2 and SSDs of 100 and 85 cm respectively.*

Although the 6 MV beam of the conventional linac used in the validation of the dose calculation model and the TomoTherapy beam have the same nominal energy, they have different spectral characteristics (see Section 2.4.2). The energy characteristics of the beam are reflected in its PDD curve. Figure 4.7 shows the comparison between the calculated PDD distributions for the linac and for the TomoTherapy beam, using the same nominal field size (of 5x5 cm^2). One of the main reasons of the spectral differences is the flattening filter, which filters the photons from the low energy end of the spectrum and thus, makes the linac spectrum harder than the one of the TomoTherapy beam. This, increases the (mean) forward range of the secondary electrons, thus, the depth of maximum dose (where the condition of CPE is achieved) is shifted to a deeper position with respect to the TomoTherapy case.

4.2.2 On the evaluation of the tool

After comparing measured and calculated OFs and dose profiles for different field configurations in the static and dynamic delivery modes, it was found that they were in very good agreement (within the acceptance criteria of 2%/2mm globally defined).

Most of the small discrepancies between measured and calculated profiles and OFs in the static mode (see Figure 3.13 and 3.14) can be associated with interpolation, convolution or voxel averaging effects (the calculation grid was of 1x1x1 mm^3). Nevertheless, the influence of other effects related to the MLC hardware (i.e., the exact shape and position of the leaves) could not be discarded as the approximation of perfect collimators was used.

Figure 3.15 shows that the penumbras in the X and Y directions are well modeled by the combination of extended source and PBK effects. Furthermore, the inclusion of the leakage contribution in the X direction was shown to be sufficient to accurately model the "umbra" of the distributions down to ∼1% of the maximum dose, in contrast to results obtained for the linac (see Figure 4.5(b)), were the leakage contributions were not considered. The fact that the agreement in the Y direction is very good, is based on the fact that the jaws that define the field size in the longitudinal direction were made of tungsten of up to 23 cm in thickness and, therefore, the contributions due to the transmission of photons through the collimators in this direction was negligible. As seen in Figure 3.16, the tool was also found to be well suited to model dose distribution in asymmetric and complex field configurations.

From the dynamic tests, it was found that the verification tool was able to reproduce measured profiles within 2%/2mm for simple beam configurations. By looking at the measured profiles for this simple configurations, the effect of temporal variations in one or more of the beam parameters was identified (because the "plateau" regions were not flat as expected for constant parameters). Once the sinograms (and treatment parameters) of patients become available, the application of this tool as a patient specific QA test should be evaluated.

4.2.3 On the parameter variations

The dose verification tool is not only useful as a dose verification system, but also can be use to study more deeply this dynamic delivery technique and identify the individual role of the different beam parameters in the final outcome of the treatment.

As the overall performance of the system depends on the performance and synchrony of the MLC, gantry, couch and linac. Random and systematic variations were introduced to the parameters that are considered constant in the planning of the treatments (beam output, couch velocity and gantry speed). The results of this study were presented in Section 3.2.3.

It was found that none of the variations introduced (see Figure 3.19) yielded deviations greater than 3%/3mm from a reference helical distribution (for which the parameters were assumed to be constant during the complete treatment). It was interesting to see that random variations of the beam output (of ±2%) had almost no influence in the integral dose (with a maximum observed deviation of 0.7% from the reference value). Flynn et al. (2008) investigated the effect of output variations (random and systematic) in the integral dose for different clinical cases. They found that systematic and random variations tend to cancel out throughout the treatment and, therefore, the ±2% threshold of the beam output (recommended by Fenwick et al. 2004) was shown to be too conservative. This conclusions are in agreement with the presented results.

4.2.4 On the implementation of the tool into the quality assurance program

As previously described, it was found that the developed tool offers a very useful approach to study the TomoTherapy delivery system and to test its performance using the different available modes (static, topographic, rotational and helical). Therefore, it can be used as a supplemental dosimetric QA procedure for the system. It was possible to visualize the calculated distributions not only in one and two-dimensional representations (as shown in

Figure 3.17), but also in three-dimensional intensity maps and isosurfaces (as shown in Figure 4.8). The availability of this feature is indeed desirable in certain cases (e.g., the use of isosurfaces to study and identify variations in the "thread" effect by using different pitch values).

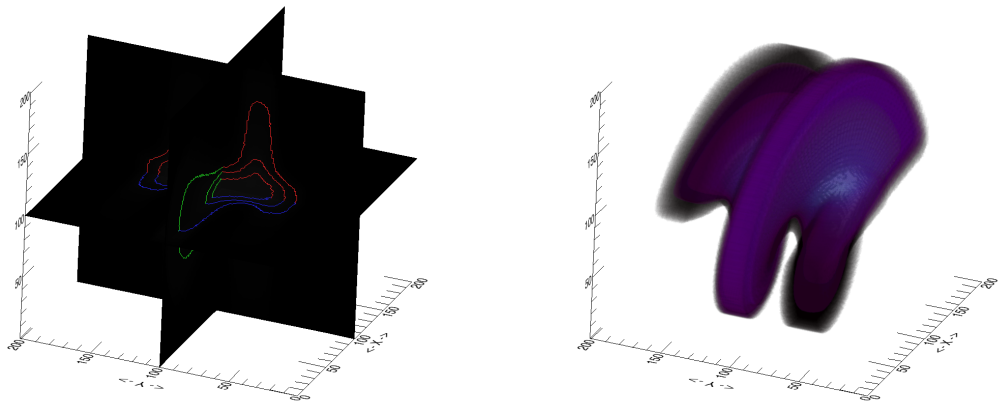

(a) (b)

Figure 4.8: *3-D visualization of an helical dose distribution delivered on the virtual cylindrical phantom. (a) Main planes and contours. (b) Isosurface and 3-D distribution.*

The dose verification tool would certainly benefit from the implementation of comparison tools (e.g., the 2-D gamma index distribution) into a stand alone application, in which all the input parameters (and output representations) can be interactively controlled by the user. In this way, its introduction into the routine QA program of the system would be easier. It was not within the scope of this thesis to address this practical implementation issues. However, considering the usability range of this tool, they should certainly be addressed as a continuation of this work. Also, a recommendation for the further expansion of the presented study, is to increase the flexibility of the phantom shape, positioning and composition (once the dose engine is validated for non-homogeneous media).

"The universe is full of magical things patiently waiting for our wits to grow sharper."

Eden Phillpotts (1862-1960)

5 Concluding Remarks

In this final chapter, the work presented throughout this thesis is summarized. An outlook together with suggestions for future research that can extend its scope and address its current limitations is also given.

5.1 Summary

This dissertation presents the implementation of a dose calculation tool for the verification of dose delivered to a homogenous phantom using the TomoTherapy system. This tool is based on a dose calculation model developed to accurately reproduce dose distributions for small fields. This procedure can be implemented as a supplemental check for the already established dosimetric QA program of the TomoTherapy system.

In Chapter 2, the main physical aspects of the energy deposition in matter for clinical photons beams and the development of the dose calculation methods, according to the technological evolution and the demanding uncertainty requirements, have been presented. The advantages and challenges posed by state-of-the-art techniques used in photon radiotherapy have been pointed out. According to this, a model that serves to account for the non-conventional conditions imposed by the use of these techniques has been developed. A special focus has been given to TomoTherapy. Within this context, the system has been described and the present QA crisis due to the accelerated technological advances has been unveiled. These advances have yielded the commercialization of non-standard systems, making it impossible (in certain cases, e.g., TomoTherapy) to apply the conventional dosimetry protocols, and thus, complicating the establishment of new standardized recommendations. A QA program of the TomoTherapy system has been presented and a strategy to study this delivery technique and to verify the dose delivered to a homogeneous phantom was proposed.

The developed model was validated for a 6 MV beam produced by a conventional linac. In the first part of Chapter 3, the results of the main model parameters and of the validation tests were shown. The shape of the extended source, reconstructed using a combination of a slit-method and CF analysis, was found to have a FWHM of 0.50±0.08

mm. The model was successfully validated, as it was able to accurately reproduce planar dose profiles and OFs in water with an agreement better than 2%/2mm for quadratic fields (calculation grid of 1x1 mm^2) and better than 2%/0.5mm for fields performed by stereotactic collimators (calculation grid of 0.1x0.1 mm^2). The second part of Chapter 3 included the results of the tests performed to the dose verification tool for TomoTherapy. For simple MLC configurations in static and dynamic modes, the results were found to be in agreement with the validation of the model (i.e., better than 2%/2mm using a calculation grid of 1x1 mm^2). The studied parameter variations revealed that: (i) most of the random variations cancel out throughout the treatment and (ii) the systematics produce variations in the overall treatment that remain below 3%/3mm.

Chapter 4 included the analysis of the results presented in the previous chapter. It was found that the reconstructed source size is in agreement with the FWHM found by Jaffray et al. (1993). The inclusion of the extended source (including head scatter contributions) into the pencil beam kernel calculations proved to be adequate, as the model was able to provide accurate modeling of the penumbra and output of the beam for a broad range of field sizes. Thus, making the transformation into absolute dose straightforward and providing an alternate method to the conventional dosimetry of small fields. Concerning the TomoTherapy results in static mode, it was confirmed that the low head scatter contributions due to the absence of a flattening filter result in an almost negligible intensity of the outer part of the source. The reconstructed source proved to be efficient in reproducing the measured penumbras. In the dynamic mode, although only simple cases were studied, the tool was found to be particularly useful to study the influence of variations in beam output, gantry speed and table position on the uncertainty of the integral dose. The application of this approach as a supplemental QA procedure was assessed and the limitations of it were discussed.

One of the main conclusions of this work is that having an independent dose calculation method is a useful and feasible supplemental QA procedure for the TomoTherapy delivery system. The model presented in this work provides a calculation tool with the capability of handling the narrow beam conditions that are present in TomoTherapy delivered treatments. Nevertheless, the approach developed in this thesis still has some limitations that need to be addressed in future studies. In the next section, suggestions to be considered as an extension of this project are presented.

5.2 Perspectives

As discussed in Chapter 4, the concepts and methods used in the implementation of the tool are based on simple theoretical considerations, and therefore, straightforward to be performed (once the input data has been obtained). Although the developed tool proved to be sufficiently accurate and useful for the verification of dose distributions delivered (in a homogeneous medium) by the TomoTherapy system, it would certainly benefit from further developments.

After finishing this project, it was realized that the accuracy of the calculation tool could be further improved by including more effects that were not explicitly modeled in this approach. These effects include a complete characterization of the MLC (taking into account that they are not perfectly aligned with the source) and the inclusion of the couch into the calculation algorithm.

It would be desirable that the dose verification tool was implemented into a stand-alone

application with a user-friendly interface in order to ease its incorporation into the clinical QA program of the system. Considering the usefulness and potential of the presented method, it would be worth to continue this work by implementing such an application. In this way, after inputting the basic parameters (i.e., source shape, PBK distribution and envelope profile) the user could easily control the treatment parameters and the desired output form (point, profile or plane calculation) in an interactive way. The possibility to input reference data and the availability of comparison tools, such as the gamma index calculation, would also be desirable to ease the integration of this procedure into the workflow of the QA program.

To extend the application of this tool from its current state of supplemental delivery verification procedure into a TPS verification system, it is necessary that the model handles inhomogeneities and performs calculations using the CT data-set of the patient. For this purpose, the pencil beam approach may not be adequate anymore, as it can only account for inhomogeneities in the forward direction by kernel scaling (it can not correct for lateral inhomogeneities). Therefore, it might be appropriate to use a collapsed-cone convolution approach, increasing the complexity of the algorithm.

Bibliography

Ahnesjö A 1989 Collapsed cone convolution of radiant energy for photon dose calculation in heterogeneous media *Med. Phys.* **16**(4), 577–592.

Ahnesjö A 1994 Analytic modeling of photon scatter from flattening filters in photon therapy beams *Med. Phys.* **21**(8), 1227–1235.

Ahnesjö A, Andreo P and Brahme A 1987 Calculation and application of point spread functions for treatment planning with high energy photon beams *Acta Oncologica* **26**(1), 49–56.

Ahnesjö A and Aspradakis M M 1999 Dose calculations for external photon beams in radiotherapy *Phys. Med. Biol.* **44**(11), R99–R155.

Ahnesjö A, Saxner M and Trepp A 1992 A pencil beam model for photon dose calculation *Med. Phys.* **19**(2), 263–273.

Ahnesjö A and Trepp A 1991 Acquisition of the effective lateral energy fluence distribution for photon beam dose calculations by convolution models *Phys. Med. Biol.* **36**(7), 973–985.

Alfonso R, Andreo P, Capote R, Huq M S, Kilby W, Kjall P, Mackie T R, Palmans H, Rosser K, Seuntjens J, Ullrich W and Vatnitsky S 2008 A new formalism for reference dosimetry of small and nonstandard fields *Med. Phys.* **35**(11), 5179–5186.

Almond P R, Biggs P J, Coursey B M, Hanson W F, Huq M S, Nath R and Rogers D W O 1999 AAPM's TG-51 protocol for clinical reference dosimetry of high-energy photon and electron beams *Med. Phys.* **26**(9), 1847–1870.

Andreo P, Burns D T, Hohlfeld K, Huq M S, Kanai T, Laitano F, Smyth V and Vynckier S 2000 Absorbed dose determination in external beam radiotherapy: An international code of practice for dosimetry based on standards of absorbed dose to water iaea technical report series no 398 Technical report IAEA Vienna, Austria.

Andreo P and Ortiz-Lopez P 1997 Tecdoc-1040: Quality assurance in radiotherapy Technical report IAEA Vienna, Austria.

Balog J, Holmes T and Vaden R 2006 Helical tomotherapy dynamic quality assurance *Med. Phys.* **33**(10), 3939–3950.

Balog J, Olivera G and Kapatoes J 2003 Clinical helical tomotherapy commissioning dosimetry *Med. Phys.* **30**(12), 3097–3106.

Balog J and Soisson E 2008 Helical tomotherapy quality assurance *Int. J. Radiation Oncology Biol. Phys.* **71**(1, Supplement 1), S113–S117.

Belletti S, Dutreix A, Garavaglia G, Gfirtner H, Haywood J, Jessen K A, Lamm I L, Mijnheer B, Noël A, Nüsslin F, Rosenow U, Schneider P, Seelentag W, Sheriff S, Svensson H and Thwaites D 1996 Quality assurance in radiotherapy: The importance of Medical Physics staffing levels. Recommendations from an ESTRO/EFOMP joint task group *Rad. Oncol.* **41**(1), 89–94.

Berger M J and Seltzer S M 1982 Stopping powers and ranges of electrons and positrons Technical report National Bureau of Standards Report NBSIR 822550 Washington, DC, United Sates of America.

BIPM, IEC, IFCC, ISO, IUPAC, IUPAP and OIML 1995 *Guide to the Expression of Uncertainty in Measurement* International Organisation for Standardisation. Geneva, Switzerland.

Bortfeld T 2006 IMRT: A review and preview *Phys. Med. Biol.* **51**(13), R363–R379.

Bortfeld T, Schlegel W and Rhein B 1993 Decomposition of pencil beam kernels for fast dose calculations in three-dimensional treatment planning *Med. Phys.* **20**(2), 311–318.

Bourland J D and Chaney E L 1992 A finite-size pencil beam model for photon dose calculations in three dimensions *Med. Phys.* **19**(6), 1401–1412.

Boyer A, Biggs P, Galvin J, Klein E, LoSasso T, Low D, Mah K and Yu C 2001 Basic Applications of Multileaf Collimators: Report of AAPM radiation therapy task group no. 50 Technical report AAPM Madison, WI, United Sates of America.

Boyer A, Biggs P, Galvin J, Klein E, LoSasso T, Low D, Mah K and Yu C 2004 Tissue inhomogeneity corrections for megavoltage photon beams: Report of AAPM radiation therapy task group no. 65 Technical report AAPM Madison, WI, United Sates of America.

Boyer A and Mok E 1985 A photon dose distribution model employing convolution calculations *Med. Phys.* **12**(2), 169–177.

Boyle P and Levin B, eds 2008 *World Cancer Report 2008* International Agency for Research on Cancer (IARC).

Brahme A, Roos J E and Lax I 1982 Solution of an integral equation encountered in rotation therapy *Phys. Med. Biol.* **27**(10), 1221–1229.

Broggi S, Cattaneo G M, Molinelli S, Maggiulli E, Vecchio A D, Longobardi B, Perna L, Fazio F and Calandrino R 2008 Results of a two-year quality control program for a helical tomotherapy unit *Rad. Oncol.* **86**(2), 231–241.

Calcina C S G, de Oliveira L N, de Almeida C E and de Almeida A 2007 Dosimetric parameters for small field sizes using fricke xylenol gel, thermoluminescent and film dosimeters, and an ionization chamber *Phys. Med. Biol.* **52**(5), 1431–1439.

Caprile P and Hartmann G H 2009 Development and validation of a beam model applicable to small fields *Phys. Med. Biol.* **54**(10), 3257–3268.

Ceberg C P, Bjärngard B E and Zhu T C 1996 Experimental determination of the dose kernel in high-energy x-ray beams *Med. Phys.* **23**(4), 505–511.

Childress N L, White R A, Bloch C, Salehpour M, Dong L and Rosen I I 2005 Retrospective analysis of 2d patient-specific imrt verifications *Med. Phys.* **32**(4), 838–850.

Chui C, LoSasso T and Palm A 2003 Computational algorithms for independent verification of IMRT. In: A Practical Guide to Intensity-Modulated Radiation Therapy (Madison, WI: Med. Phys. Publishing) pp. 83–101.

Chui C S and Mohan R 1988 Extraction of pencil beam kernels by the deconvolution method *Med. Phys.* **15**(2), 138–144.

Crop F, Reynaert N, Pittomvils G, Paelinck L, Gersem W D, Wagter C D, Vakaet L, Neve W D and Thierens H 2007 Monte Carlo modeling of the moduleaf miniature mlc for small field dosimetry and quality assurance of the clinical treatment planning system *Phys. Med. Biol.* **52**(11), 3275–3290.

Cunningham J R 1972 Scatter-air ratios *Phys. Med. Biol.* **17**(1), 42–51.

Das I J, Ding G X and Ahnesjö A 2008 Small fields: Nonequilibrium radiation dosimetry *Med. Phys.* **35**(1), 206–215.

Day M J 1950 A note on the calculation of dose in x-ray fields *Br. J. Radiol.* **23**, 368–369.

Delaney G, Jacob S, Featherstone C and Barton M 2003 Radiotherapy in cancer care: Estimating optimal utilization from a review of evidence-based clinical guidelines Technical report Collaboration for Cancer Outcomes Research and Evaluation (CCORE) Liverpool Hospital, Sydney, Australia.

Djouguela A, Harder D, Kollhoff R, Foschepoth S, Kunth W, Ruhmann A, Willborn K and Poppe B 2009 Fourier deconvolution reveals the role of the lorentz function as the convolution kernel of narrow photon beams *Phys. Med. Biol.* **54**(9), 2807–2827.

Dutreix A 1984 When and how can we improve precision in radiotherapy? *Radiother. and Oncol.* **2**(4), 275–292.

Eklöf A, Ahnesjö A and Brahme A 1990 Photon beam energy deposition kernels for inverse radiotherapy planning *Acta Oncol.* **29**(4), 447–454.

El-Khatib E and Battista J J 1984 Improved lung dose calculation using tissue–maximum ratios in the batho correction *Med. Phys.* **11**(3), 279–286.

Ezzell G A, Galvin J M, Low D, Palta J R, Rosen I, Sharpe M B, Xia P, Xiao Y, Xing L and Yu C X 2003 Guidance document on delivery, treatment planning, and clinical implementation of IMRT: Report of the IMRT subcommittee of the AAPM radiation therapy committee *Med. Phys.* **30**(8), 2089–2115.

Fenwick J D, Tome W A, Jaradat H A, Hui S K, James J A, Balog J P, DeSouza C N, Lucas D B, Olivera G H, Mackie T R and Paliwal B R 2004 Quality assurance of a helical tomotherapy machine *Phys. Med. Biol.* **49**(13), 2933–2953.

Flynn R T, Kissick M W, Mehta M P, Olivera G H, Jeraj R and Mackie T R 2008 The impact of linac output variations on dose distributions in helical tomotherapy *Phys. Med. Biol.* **53**(2), 417–430.

Fraass B, Doppke K, Hunt M, Kutcher G, Starkschall G, Stern R and Dyke J V 1998 American association of physicists in medicine radiation therapy committee Task Group 53: Quality assurance for clinical radiotherapy treatment planning *Med. Phys.* **25**(10), 1773–1829.

Gaskill J D 1978 *Linear systems, Fourier transforms, and optics* Wiley Series in Pure and Applied Optics, New York: Wiley, 1978.

Gibbons J, Smith K, Cheek D and Rosen I 2009 Independent calculation of dose from a helical tomotherapy unit *J. Appl. Clin. Med. Phys.* **10**(1), 103–119.

Giraud P, Elles S, Helfre S, Rycke Y D, Servois V, Carette M F, Alzieu C, Bondiau P Y, Dubray B, Touboul E, Housset M, Rosenwald J C and Cosset J M 2002 Conformal radiotherapy for lung cancer: Different delineation of the gross tumor volume (GTV) by radiologists and radiation oncologists *Radiother. Oncol.* **62**(1), 27–36.

Hobbie R and Roth B 2007 *Intermediate physics for medicine and biology* Springer.

ICRU 1976 Determination of absorbed dose in a patient irradiated by beams of x or gamma rays in radiotherapy procedures Technical report International Commission on Radiation Units and Measurements (ICRU) Washington, DC, United Sates of America.

Jaffray D A, Battista J J, Fenster A and Munro P 1993 X-ray sources of medical linear accelerators: Focal and extra-focal radiation *Med. Phys.* **20**(5), 1417–1427.

Jeleń U 2007 Development and verification of a high-precision dose calculation algorithm for IMRT treatment planning PhD thesis AGH University of Science and Technology, Poland.

Jeraj R, Mackie T R, Balog J, Olivera G, Pearson D, Kapatoes J, Ruchala K and Reckwerdt P 2004 Radiation characteristics of helical tomotherapy *Med. Phys.* **31**(2), 396–404.

Khan F M, Sewchand W, Lee J and Williamson J F 1980 Revision of tissue-maximum ratio and scatter-maximum ratio concepts for cobalt 60 and higher energy x-ray beams *Med. Phys.* **7**(3), 230–237.

Kissick M W, Fenwick J, James J A, Jeraj R, Kapatoes J M, Keller H, Mackie T R, Olivera G and Soisson E T 2005 The helical tomotherapy thread effect *Med. Phys.* **32**(5), 1414–1423.

Kopka H and Daly P W 1977 *Donner Algorithms for Reconstructive Tomography Users Manual* Lawrence Berkeley Laboratory, Publication No. 214.

Kutcher G J, Coia L, Gillin M, Hanson W F, Leibel S, Morton R J, Palta J R, Purdy J A, Reinstein L E, Svensson G K, Weller M and Wingfield L 1994 Comprehensive QA for radiation oncology: Report of AAPM radiation therapy committee task group 40 *Med. Phys.* **21**(4), 581–618.

Leunens G, Menten J, Weltens C, Verstraete J and van der Schueren E 1993 Quality assessment of medical decision making in radiation oncology: Variability in target volume delineation for brain tumours *Radiother. Oncol.* **29**(2), 169–175.

Low D A, Chao K, Mutic S, Gerber R L, Perez C A and Purdy J A 1998 Quality assurance of serial tomotherapy for head and neck patient treatments *Int. J. Radiation Oncology Biol. Phys.* **42**(3), 681–692.

Low D A and Dempsey J F 2003 Evaluation of the gamma dose distribution comparison method *Med. Phys.* **30**(9), 2455–2464.

Low D A, Harms W B, Mutic S and Purdy J A 1998 A technique for the quantitative evaluation of dose distributions *Med. Phys.* **25**(5), 656–661.

Mackie T R 2006 History of tomotherapy *Phys. Med. Biol.* **51**(13), R427–R453.

Mackie T R, Bielajew A F, Rogers D W O and Battista J J 1988 Generation of photon energy deposition kernels using the EGS Monte Carlo code *Phys. Med. Biol.* **33**(1), 1–20.

Mackie T R, Holmes T, Swerdloff S, Reckwerdt P, Deasy J O, Yang J, Paliwal B and Kinsella T 1993 Tomotherapy: A new concept for the delivery of dynamic conformal radiotherapy *Med. Phys.* **20**(6), 1709–1719.

Mackie T R, Scrimger J W and Battista J J 1985 A convolution method of calculating dose for 15-mv x rays *Med. Phys.* **12**(2), 188–196.

Mainegra-Hing E, Rogers D W O and Kawrakow I 2005 Calculation of photon energy deposition kernels and electron dose point kernels in water *Med. Phys.* **32**(3), 685–699.

Mijnheer B J, Battermann J J and Wambersie A 1987 What degree of accuracy is required and can be achieved in photon and neutron therapy? *Radiother. Oncol.* **8**(3), 237–52.

Mohan R, Chui C and Lidofsky L 1985 Energy and angular distributions of photons from medical linear accelerators *Med. Phys.* **12**(5), 592–597.

Mohan R, Chui C and Lidofsky L 1986 Differential pencil beam dose computation model for photons *Med. Phys.* **13**(1), 64–73.

Mohan R and Chui C S 1987 Use of fast fourier transforms in calculating dose distributions for irregularly shaped fields for three-dimensional treatment planning *Med. Phys.* **14**(1), 70–77.

Munro P, Rawlinson J A and Fenster A 1988 Therapy imaging: Source sizes of radiotherapy beams *Med. Phys.* **15**(4), 517–524.

Nath R, Biggs P J, Bova F J, Ling C C, Purdy J A, van de Geijn J and Weinhous M S 1994 AAPM code of practice for radiotherapy accelerators: Report of AAPM radiation therapy task group no. 45 *Med. Phys.* **21**(7), 1093–1121.

Nilsson B and Brahme A 1981 Contamination of high-energy photon beams by scattered photons. *Strahlentherapie* **157**(3), 181–6.

Nyholm T, Olofsson J, Ahnesjö A, Georg D and Karlsson M 2006 Pencil kernel correction and residual error estimation for quality-index-based dose calculations *Phys. Med. Biol.* **51**(23), 6245–6262.

Olofsson J 2006 Developing and Evaluating Dose Calculation Models for Verification of Advanced Radiotherapy PhD thesis Umeå University, Sweden.

Palta J R, Liu C and Li J G 2008*a* Current external beam radiation therapy quality assurance guidance: Does it meet the challenges of emerging image-guided technologies? *Int. J. Radiation Oncology Biol. Phys.* **71**(1, Supplement 1), S13–S17.

Palta J R, Liu C and Li J G 2008*b* Quality assurance of intensity-modulated radiation therapy *Int. J. Radiation Oncology Biol. Phys.* **71**(1, Supplement 1), S108–S112.

Pappas E, Maris T G, Zacharopoulou F, Papadakis A, Manolopoulos S, Green S and Wojnecki C 2008 Small SRS photon field profile dosimetry performed using a pinpoint air ion chamber, a diamond detector, a novel silicon-diode array (DOSI), and polymer gel dosimetry. analysis and intercomparison *Med. Phys.* **35**(10), 4640–4648.

Rathee S, McClean B A and Field C 1993 An improved method for rebinning kernels from cylindrical to cartesian coordinates *Med. Phys.* **20**(5), 1343–1351.

Rogers D, Kawrakow I, Seuntjens J, Walters B and Mainegra-Hing E 2001 NRC user codes for EGSnrc Technical report National Research Council of Canada Report No PIRS-702.

Sánchez-Doblado F, Hartmann G H, Pena J, Roselló J V, Russiello G and Gonzalez-Castano D M 2007 A new method for output factor determination in mlc shaped narrow beams *Physica Medica* **23**(2), 58–66.

Sarkar V, Lin L, Shi C and Papanikolaou N 2007 Quality assurance of the multileaf collimator with helical tomotherapy: Design and implementation *Med. Phys.* **34**(7), 2949–2956.

Schlegel W and Mahr A, eds 2007 *3D Conformal Radiation Therapy - A Multimedia Introduction to Methods and Techniques, 2nd revised and enhanced edition. Multimedia DVD.* Springer.

Schneider W, Bortfeld T and Schlegel W 2000 Correlation between CT numbers and tissue parameters needed for Monte Carlo simulations of clinical dose distributions *Phys. Med. Biol.* **45**(2), 459–478.

Scholz C, Schulze C, Oelfke U and Bortfeld T 2003 Development and clinical application of a fast superposition algorithm in radiation therapy *Radiother. Oncol.* **69**(1), 79–90.

Scott A J D, Nahum A E and Fenwick J D 2008 Using a Monte Carlo model to predict dosimetric properties of small radiotherapy photon fields *Med. Phys.* **35**(10), 4671–4684.

Sharpe M B and Battista J J 1993 Dose calculations using convolution and superposition principles: The orientation of dose spread kernels in divergent x-ray beams *Med. Phys.* **20**(6), 1685–1694.

Sontag M, Battista J, Bronskill M and Cunningham J 1977 Implications of computed tomography for inhomogeneity corrections in photon beam dose calculations *Radiology* **124**(1), 143–149.

Sontag M and Cunningham J 1978 The equivalent tissue-air ratio method for making absorbed dose calculations in a heterogeneous medium *Radiology* **129**(3), 787–794.

Sontag M R and Cunningham J R 1977 Corrections to absorbed dose calculations for tissue inhomogeneities *Med. Phys.* **4**(5), 431–436.

Sterzing F, Schubert K, Sroka-Perez G, Kalz J, Debus J and Herfarth K 2007 Helical tomotherapy. Experiences of the first 150 patients in Heidelberg. *Strahlenther. Onkol.* **184**(1), 8–14.

Storchi P and Woudstra E 1996 Calculation of the absorbed dose distribution due to irregularly shaped photon beams using pencil beam kernels derived from basic beam data *Phys. Med. Biol.* **41**(4), 637–656.

Thames H D 1973 First scatter to off-axis points and the clarkson method (absorbed dose distributions) *Phys. Med. Biol.* **18**(3), 444–451.

Thomas S D, Mackenzie M, Field G C, Syme A M and Fallone B G 2005 Patient specific treatment verifications for helical tomotherapy treatment plans *Med. Phys.* **32**(12), 3793–3800.

Treuer H, Boesecke R, Schlegel W, Hartmann G H, Muller R P and Sturm V 1993 The source-density function: Determination from measured lateral dose distributions and use for convolution dosimetry *Phys. Med. Biol.* **38**(12), 1895–1909.

Treuer H, Hoevels M, Luyken K, Hunsche S, Kocher M, Muller R P and Sturm V 2003 Geometrical and dosimetrical characterization of the photon source using a micro-multileaf collimator for stereotactic radiosurgery *Phys. Med. Biol.* **48**(15), 2307–2319.

Van Dyk J 2008 Quality assurance of radiation therapy planning systems: Current status and remaining challenges *Int. J. Radiation Oncology Biol. Phys.* **71**(1, Supplement 1), S23–S27.

van Zijtveld M, Dirkx M L, de Boer H C and Heijmen B J 2006 Dosimetric pre-treatment verification of IMRT using an EPID; clinical experience *Radioth. Oncol.* **81**(2), 168–175.

Wambersie A 2001 What accuracy is required and can be achieved in radiation therapy (review of radiobiological and clinical data) *Radiochimica Acta* **89**(4-5/2001), 255.

Webb S 2001 *Intensity-modulated radiation therapy* IOP Publishing Bristol and Phiadelphia.

Williamson J F, Dunscombe P B, Sharpe M B, Thomadsen B R, Purdy J A and Deye J A 2008 Quality assurance needs for modern image-based radiotherapy: Recommendations from 2007 interorganizational symposium on "quality assurance of radiation therapy: Challenges of advanced technology" *Int. J. Radiation Oncology Biol. Phys.* **71**(1, Supplement 1), S2–S12.

Winkler P, Zurl B, Guss H, Kindl P and Stuecklschweiger G 2005 Performance analysis of a film dosimetric quality assurance procedure for IMRT with regard to the employment of quantitative evaluation methods *Phys. Med. Biol.* **50**(4), 643–654.

Woo S Y, Grant W, McGary J E, Teh B S and Butler E B 2003 The evolution of quality assurance for intensity- modulated radiation therapy (IMRT): Sequential tomotherapy *Int. J. Radiation Oncology Biol. Phys.* **56**(1), 274–286.

Yan G, Liu C, Lu B, Palta J R and Li J G 2008 Comparison of analytic source models for head scatter factor calculation and planar dose calculation for IMRT *Phys. Med. Biol.*. **53**(8), 2051–2067.

Yang Y, Xing L, Boyer A L, Song Y and Hu Y 2002 A three-source model for the calculation of head scatter factors *Med. Phys.* **29**(9), 2024–2033.

Zhu T C, Bjärngard B E and Shackford H 1995 X-ray source and the output factor *Med. Phys.* **22**(6), 793–798.

List of Figures

List of Tables

Acknowledgements

During the last three years working towards my PhD, many people have supported me. Here, I would like to acknowledge them.

First of all, I would like to thank my supervisor Prof. Günther Hartmann, for accepting me in his working group, for his guidance, the numerous discussions, and career advice. I am sincerely grateful for your confidence in my work, for your availability, patience and constant motivation.

My stay in Heidelberg would not have been possible without the support of Prof. Wolfgang Schlegel, who helped me since the early days of my application to the PhD program. Thank you for your advice, for creating a great working atmosphere as Head of our Department and for agreeing in being the second referee of my dissertation.

I would like to thank the people in the hospital, specially to Dr. Gabriele Soroka-Perez for easing my work with the TomoTherapy system, to Dr. Kai Schubert for his availability and patience to answer all the (many) questions related with the system and QA, to Katja Wagenknecht and Stephan Bader for priceless technical support in the long measurement weekends and to Dr. Florian Sterzing for the camaraderie.

Thanks to my current and former office mates, "Los Topos": Andrés Vásquez, Christine Harting, Ina Niedermayer, Martina Hub, Sarah Fleischhacker, Sonja Lahrmann and Torsten Moser, for providing a friendly environment, for helping me solve all kind of bureaucracy related issues, for the "Mittwoch sekts" and all the other activities that we shared. Thanks in particular to Sonja, for being my "complaining pal", gift advisor and for proofreading of this thesis.

I would like to acknowledge the DKFZ International Ph.D. Program that awarded me a three-year fellowship to carry out my PhD. To Prof. Iring Bender, Prof. Dirk Dubbers and Prof. Wolfgang Schlegel, thank you for kindly agreeing to form part of my examination committee.

Many weekends and holidays were spent with our dear friends Paula Jofré and Manuel Aravena. Perhaps being far from home brought us closer as friends. You were really important during this period of my life, wherever destiny takes us, you will always have a special place in my heart.

Special thanks go to my family, in particular to my parents Juan Carlos Caprile and Alejandra Etchart. Papá, mamá, gracias por su amor incondicional y por haber creido siempre en mi. I would also like to thank my acquired family, for the support and sincere caring, and my old friends back in Chile, specially Constanza Miranda, for many laughs and for making me feel close (thanks to skype).

Finally and most importantly, I would like to thank Timo Anguita. My love, my friend, my life partner; computational assistant, proofreader and so much more. Thank you for being there in every step of the way. I could not have done it without you.